

FREQUENCY-SCANNED WAVEGUIDE-FED SLOT ARRAY FOR MILLIMETRE-WAVE  
RADAR APPLICATIONS

by

Michael Royle

A thesis submitted in conformity with the requirements  
for the degree of Master of Applied Science  
Graduate Department of Electrical and Computer Engineering  
University of Toronto

# **Abstract**

Frequency-Scanned Waveguide-Fed Slot Array for Millimetre-Wave Radar Applications

Michael Royle

Master of Applied Science

Graduate Department of Electrical and Computer Engineering

University of Toronto

2016

Millimetre-wave designs have become increasingly common in radar applications due to advantages when compared with traditional microwave designs. The increased operating frequencies offer greater bandwidths and allow for reduced antenna sizes. In radar systems, large bandwidths are used to achieve high range resolutions. At millimetre-wave frequencies, there is sufficient bandwidth for additional uses, most notably, beam steering using a frequency-scanning antenna. Due to their simplicity, these antennas are particularly attractive for commercial radar applications. In this work, a millimetre-wave frequency-scanned slot array was designed based on a serpentine waveguide for a 1.8 GHz bandwidth centred at 34.3 GHz. The antenna was fabricated, and measurements indicated a range resolution better than 1.25 metres over an angular scanning range of 20 degrees. The antenna was incorporated in a simplified radar system, which successfully demonstrated the ability to detect and locate multiple targets simultaneously.

## Acknowledgements

I would like to take this opportunity to acknowledge the people and organizations that have contributed to the success of this thesis. First, I would like to thank my supervisor, Professor George V. Eleftheriades for his guidance, advice, and encouragement throughout this project. In addition, I thank the remaining members of my examination committee: Professors Costas Sarris, Sean Hum, and Raviraj Adve. I would also like to thank my colleagues in the Electromagnetics Group for their friendship and advice regarding many aspects of graduate studies. Finally, I would like to acknowledge the financial support received from the National Sciences and Engineering Research Council of Canada, the University of Toronto, the Edward S. Rogers Sr. Scholarship, as well as AUG Signals for funding the fabrication of the designed antenna.

# Contents

<b>1</b>	<b>Introduction</b>	<b>1</b>
1.1	Motivation . . . . .	2
1.1.1	Antenna Requirements . . . . .	2
1.2	Beam Scanning . . . . .	4
1.2.1	Electronic Scanning: Phased Arrays . . . . .	4
1.2.2	Electronic Scanning: Frequency Scanned Arrays . . . . .	5
1.3	Waveguide-fed Slot Arrays . . . . .	6
1.4	Objectives and Proposed Design . . . . .	8
1.5	Thesis Outline . . . . .	10
<b>2</b>	<b>Antenna Array Theory</b>	<b>11</b>
2.1	Antenna Array Fundamentals . . . . .	11
2.1.1	Principle of Pattern Multiplication . . . . .	12
2.1.2	Array Factor Determination . . . . .	12
2.1.3	Properties of Linear Arrays . . . . .	13
2.2	Frequency Scanned Arrays . . . . .	17
2.2.1	Bandwidth Considerations . . . . .	18
2.3	Array Pattern Synthesis . . . . .	19
2.3.1	Dolph-Chebyshev Array . . . . .	20
2.3.2	Taylor-Villeneuve Array . . . . .	21
<b>3</b>	<b>Waveguide-fed Slot Array Theory and Design</b>	<b>26</b>
3.1	Slot Antenna . . . . .	26
3.2	Waveguide-fed Slot Array Design . . . . .	30
3.2.1	Active Slot Impedance Determination . . . . .	30

3.2.2	Travelling-Wave Arrays . . . . .	32
3.2.3	Reflection Cancelling Arrays . . . . .	34
3.3	Frequency Scanning Waveguide-fed Slot Arrays . . . . .	36
3.4	Fabrication of Waveguides . . . . .	38
<b>4</b>	<b>Frequency Modulated Radar</b>	<b>39</b>
4.1	Principle of Operation . . . . .	40
4.1.1	Range Resolution . . . . .	41
4.2	Frequency Scanning Implementation . . . . .	41
4.3	Practical Considerations . . . . .	42
4.3.1	Range and Angular Resolutions . . . . .	43
4.3.2	Radar Equation . . . . .	43
4.3.3	Radar Cross Section . . . . .	43
4.3.4	Signal to Noise Ratio . . . . .	44
4.3.5	Receiver Noise and Noise Figure . . . . .	44
4.3.6	Transmitter Phase Noise and Leakage . . . . .	45
4.3.7	Clutter . . . . .	46
<b>5</b>	<b>Antenna Design and Simulation</b>	<b>47</b>
5.1	Design Overview and Initial Considerations . . . . .	47
5.2	Serpentine Waveguide Design . . . . .	49
5.3	Slot-Pit Pair Design . . . . .	51
5.3.1	Reflection Cancelling . . . . .	52
5.3.2	Element Coupling and Phasing . . . . .	55
5.4	Taylor-Villeneuve Implementation . . . . .	59
5.5	Simulation Results . . . . .	61
5.5.1	Radiation Patterns . . . . .	62
5.5.2	Scanning Performance . . . . .	62
5.6	Summary . . . . .	66
<b>6</b>	<b>Antenna Fabrication and Measurement Results</b>	<b>67</b>
6.1	Antenna Fabrication . . . . .	67
6.2	Antenna Measurements . . . . .	69
6.2.1	Radiation Patterns . . . . .	69

6.2.2	Scanning Performance . . . . .	70
6.2.3	Measurement Summary . . . . .	74
6.3	Radar Equation Example . . . . .	74
6.4	Discrepancies . . . . .	76
<b>7</b>	<b>Radar Demonstration</b>	<b>82</b>
7.1	Demonstration Overview . . . . .	82
7.1.1	Radar Components . . . . .	84
7.1.2	Targets . . . . .	86
7.1.3	Signal-to-Noise Ratio Estimate . . . . .	87
7.1.4	System Limitations . . . . .	89
7.2	Results . . . . .	90
7.2.1	Single Target . . . . .	90
7.2.2	Multiple Targets . . . . .	94
7.2.3	Range Resolution . . . . .	96
7.3	Summary . . . . .	99
<b>8</b>	<b>Conclusion</b>	<b>100</b>
8.1	Future Directions . . . . .	102
<b>Appendix A</b>	<b>Detailed Antenna Drawings</b>	<b>105</b>
<b>Bibliography</b>		<b>110</b>

# List of Figures

1.1	Atmospheric Absorption of Radio Frequencies at Sea Level . . . . .	2
1.2	Planar Phased Array . . . . .	5
1.3	Frequency Scanned Antenna Array . . . . .	5
1.4	Slotted Waveguide . . . . .	6
1.5	Meandered Slotted Waveguide . . . . .	7
1.6	Proposed Design . . . . .	9
1.7	Multiple Antenna Configuration . . . . .	9
2.1	Linear Array . . . . .	13
2.2	Frequency Scanned Antenna Array . . . . .	17
2.3	Array Factor and Amplitude Distribution Comparison . . . . .	24
2.4	Modified Dolph-Chebyshev Array Factor . . . . .	25
3.1	Waveguide-fed Slot Antenna . . . . .	27
3.2	Vector surface currents of a rectangular waveguide . . . . .	28
3.3	Series Slots and Their Equivalent Circuit . . . . .	29
3.4	Shunt Slots and Their Equivalent Circuit . . . . .	29
3.5	Slot Antenna Simulation Model . . . . .	32
3.6	Traveling-Wave Array Transmission Line Model . . . . .	33
3.7	Reflection Cancelling Array Elements . . . . .	35
3.8	Frequency Scanned Waveguide-fed Slot Array Excitation . . . . .	37
4.1	FMCW Principle . . . . .	40
4.2	Frequency Scanned FMCW Radar Block Diagram . . . . .	41
5.1	Antenna Design Concept . . . . .	48
5.2	Waveguide Unit Cell . . . . .	50

5.3	Waveguide Bend Simulation Results . . . . .	50
5.4	Reflection Coefficient of 10 Serpentine Waveguide Unit Cells . . . . .	51
5.5	Algebraic Uniform Array Factor for 10 Unit Cells . . . . .	52
5.6	Simulated Model of Slot-Pit Pair . . . . .	53
5.7	Slot Equivalent Series Impedance . . . . .	54
5.8	Reflection Coefficient of Isolated Elements . . . . .	55
5.9	Reflection Coefficient Improvement for a Single Slot . . . . .	55
5.10	Summary of Slot-Pit Pair Design . . . . .	56
5.11	Simulated Uniform Array . . . . .	57
5.12	Uniform Array Simulation Results . . . . .	57
5.13	Summary of Coupling Values . . . . .	58
5.14	Summary of Selected Slot Lengths and Coupling Values . . . . .	60
5.15	Summary of Approximate Taylor-Villeneuve Distribution . . . . .	61
5.16	Simulated Designed Array . . . . .	62
5.17	Simulated Gain of Designed Antenna . . . . .	63
5.18	Simulated Array Scanning Characteristic . . . . .	63
5.19	Simulated Network Parameters . . . . .	64
5.20	Simulated Gain and Beamwidth . . . . .	65
5.21	Calculated Discretized Scanning Characteristic and Range Resolution . . . . .	66
6.1	SolidWorks Model of Fabricated Antenna . . . . .	68
6.2	Measured Gain of Fabricated Antenna . . . . .	69
6.3	Measured Array Scanning Characteristic . . . . .	71
6.4	Measured Reflection Coefficient . . . . .	71
6.5	Apparent Conjugate Beams . . . . .	72
6.6	Measured Gain and Beamwidth . . . . .	73
6.7	Measured Discretized Scanning Characteristic and Range Resolution . . . . .	73
6.8	Simulated Model with Air Gap . . . . .	77
6.9	Gain Reduction with Air Gap . . . . .	78
6.10	Increased Side Lobe Levels with Slot Offset . . . . .	79
6.11	Modified Simulated Model Radiation Patterns . . . . .	80
6.12	Modified Simulated Model Reflection Coefficient . . . . .	80
7.1	Block Diagram of Radar Demonstration . . . . .	83

7.2	Radar Transmitted Frequency Scanning Scheme . . . . .	83
7.3	Laboratory Equipment used in Demonstration . . . . .	85
7.4	Demonstration Receiver Components . . . . .	86
7.5	Demonstration Radar Antenna Configuration . . . . .	86
7.6	Corner Reflectors Constructed for Demonstration . . . . .	87
7.7	Single Target Demonstration . . . . .	91
7.8	Measured Received Radar Signal for Single Target . . . . .	92
7.9	Single Target Corrected Range Measurement . . . . .	92
7.10	Measured Radar Images for Single Target . . . . .	93
7.11	Processed Single Target Radar Image . . . . .	94
7.12	Multiple Target Demonstration . . . . .	95
7.13	Measured Radar Image for Multiple Target . . . . .	95
7.14	Processed Multiple Target Radar Image . . . . .	96
7.15	Range Resolution Demonstration with 100 MHz Bandwidth . . . . .	98
7.16	Range Resolution Demonstration with 150 MHz Bandwidth . . . . .	99

# Chapter 1

## Introduction

In the last two decades, there has been increased interest in the millimetre-wave (MMW) band of frequencies for commercial radar and imaging applications. This band, spanning 30 to 300 gigahertz has a number of advantages in these applications when compared to the conventionally used microwave bands. In particular, the smaller wavelength allows for physically small directive antennas and the increased available bandwidth allows for higher resolution.

Millimetre-wave frequencies have found use in a number of applications. Historically, their use was limited to the military and scientific industries due to cost considerations. These include radar and weapon systems, and remote sensing and astronomy [1]. With advances in MMW technologies and design tools, the cost of implementing components in this frequency range has reduced, becoming practical for commercial applications. In recent years, MMW designs have been used in automotive radars, law enforcement speed measurements, and point-to-point communications [2–4].

Millimetre waves have a number of properties that make them particularly suitable for short- to medium-range radar systems. While they experience higher atmospheric absorption than lower frequencies, Figure 1.1 shows transmission windows exist near 35 , 94, 140, and 220 GHz where the absorption rate is sufficiently reduced for radar applications [5]. Furthermore, millimetre waves are relatively insensitive to environmental conditions such as cloud and fog [6]. These propagation characteristics, along with the benefits of increased bandwidth have resulted in a number of successfully implemented surveillance radars, with some examples found in references [7, 8].

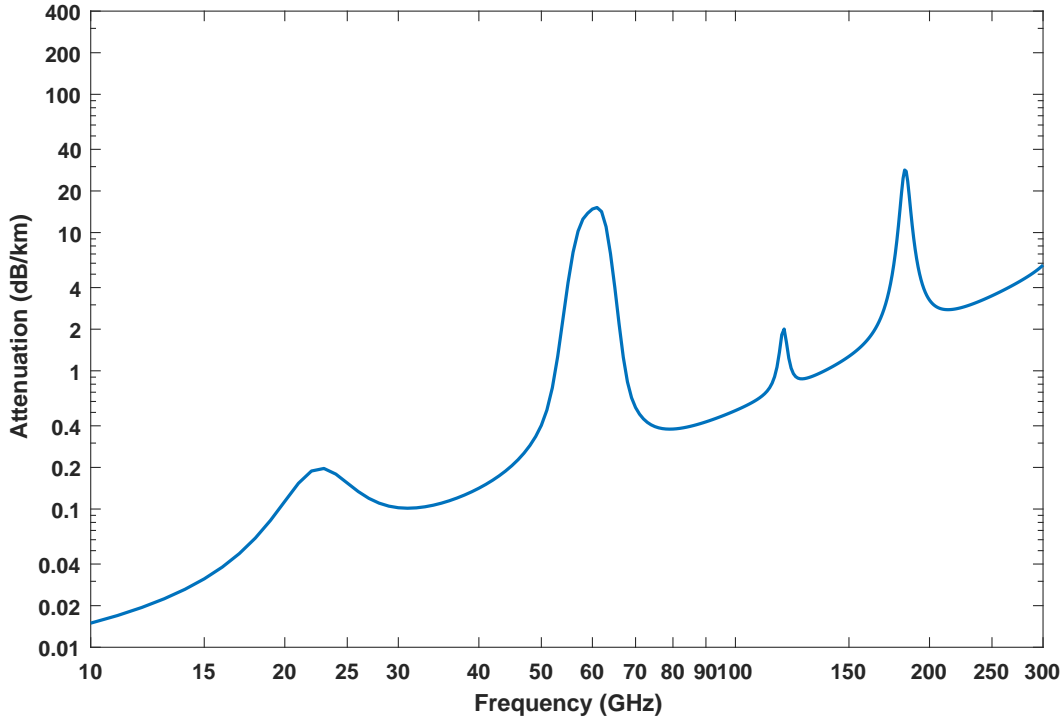


Figure 1.1: Atmospheric Absorption of Radio Frequencies at Sea Level [5].

## 1.1 Motivation

A multipurpose MMW radar system operating in the 35 GHz window is envisioned, with one specific application including highway surveillance and traffic monitoring. Radar systems deployed near highways can detect, locate, and track vehicles, persons, and large animals. This information can then be used to warn motorists of the presence of large animals in an effort to reduce animal-vehicle collisions [9].

In order to be feasible, the MMW radar system must meet a number of electrical and mechanical requirements. Most importantly, it must be able to locate its intended targets, in both range and angular position, within a sufficiently large region. For the system to be installed in remote locations, it must be designed to operate from off-grid power sources, necessitating low-power usage. Additionally, for year-round deployment in an outdoor environment, the radar must be robust. It must be able to operate in all weather conditions with minimal required maintenance. Finally, to simplify its implementation in multiple applications and locations, the system should be compact and relatively low cost.

### 1.1.1 Antenna Requirements

A critical component of both the transmit and receive functions of a radar system is its antenna. In transmitting, its role is to convert a radio frequency (RF) signal generated by the radar, to a radiated

wave directed into space and toward a target. In receiving, it must convert the received echo, scattered from a target, to a suitable RF signal for processing. It is through this received signal that a radar can determine the presence and location of a target.

The desired radar specifications, in combination with typical system performances at MMW frequencies, dictate a strict set of requirements for the radar's antenna. These features include high directivity and efficiency, beam scanning, low side lobe levels, compact form-factor, and relative low cost.

An efficient, highly directive antenna is critical to the performance of a surveillance radar. Focusing the antenna's radiated power in a narrow beam toward the observation direction allows a radar to precisely determine a target's angular position. A large directivity, when combined with high efficiency, also increases the maximum range the radar can observe. The resulting high gain antenna ensures the majority of energy input to the antenna is directed toward the target instead of in undesired directions or lost in the system.

Beam scanning is the ability of an antenna to steer the angle at which its radiation pattern is directed. This capability is required in a surveillance radar to measure the received echo from multiple directions and allows the radar to determine the angular positions of multiple targets accordingly. Beam scanning techniques typically employed in radar systems fall into two categories: mechanical and electronic. The merits of both will be discussed in Section 1.2.

Directive antennas exhibit side lobes, directions in which the antenna's power is radiated unintentionally. To ensure targets are located accurately, the power radiated in these directions must be reduced as much as practical. Low side lobe levels are required to reduce false detections due to signals received from sources in directions other than that being observed. This is particularly important in the proposed highway monitoring application as expected targets can vary significantly in size, for example automobiles and humans. Reduced side-lobe levels are achieved through tapering the excitation of an antenna across its aperture.

A low cost and compact antenna will increase the versatility of the radar system. The antenna's fabrication can contribute significantly to the overall cost of a radar system. Thus, it is an important consideration when selecting a design to implement. A smaller antenna can be installed in more locations unobtrusively. The combination of these features also introduces the possibility of including multiple antennas in a system, to economically increase its resolution and/or angular coverage.

## 1.2 Beam Scanning

The requirement of surveillance radars to determine a target's angular position has led to the development of a number techniques to steer an antenna's beam. Early radar systems achieved scanning through mechanically rotating the antenna or array in an azimuthal plane. Due to its relative simplicity, this method is still widely used in both military and commercial surveillance applications. More advanced mechanical steering techniques utilize multiple motors and a two-axis design to observe a three-dimensional volume [10].

Commercial MMW radars exist that satisfy many of the requirements for the envisioned radar system, with one example being Flir's Ranger R1, [8]. This radar is currently used in AUG Signal's Large Animal Detection System for the previously described highway surveillance application [9]. These systems however, suffer from their use of mechanical beam steering. The mechanical components required to rotate an antenna with a connection suitable for an RF signal are expensive, bulky, and draw a significant amount of electrical power in order to rotate. The rotational nature of the mechanism requires preventative maintenance or downtime for repairs. Moreover, mechanical beam steering is inherently slow when compared to RF signal processing, thus a faster method of beam-scanning allows for increased refresh rates of radar images.

### 1.2.1 Electronic Scanning: Phased Arrays

In more demanding radar applications, electronically-scanned phased arrays are employed. These directive antennas consist of a number of individual radiating elements, uniformly spaced in linear or planar arrangements. An example planar arrangement is depicted in Figure 1.2. In varying the excitation magnitude and phase of each element, the radiation pattern and steering angle of the array can be controlled. In this manner, the beam can be scanned over an angular region without the requirement of physically rotating the, typically large, array. This results in drastically increased beam-scanning speeds, on the order of microseconds [10].

In order to control the excitation amplitudes and phases required for a desired radiation pattern and steering angle, elements must be fed individually through electronically controlled components. In applications requiring only beam steering, phase shifters can be used as the feeding element. More advanced arrays may employ a complete transmitter for each individual element, providing full control of amplitude and phase, while increasing the total available power for transmission. These elements however, introduce additional loss and complexity, and significantly increase the cost of large, directive arrays. These factors typically outweigh the performance benefits in commercial applications and thus,

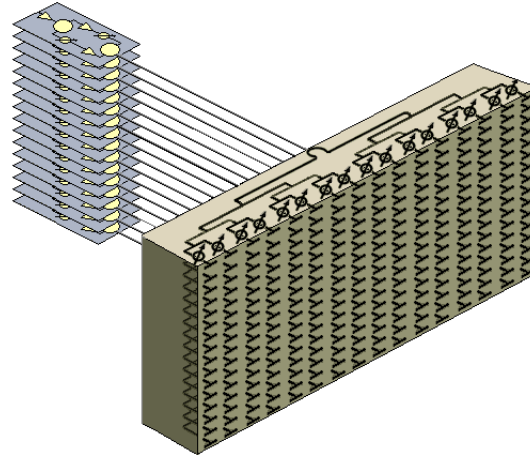


Figure 1.2: Planar Phased Array [11].

large phased arrays are generally only used in military radars.

### 1.2.2 Electronic Scanning: Frequency Scanned Arrays

Frequency-scanned arrays are a class of phased-array antenna which achieve beam steering through varying their frequency of operation. These antennas are typically implemented using serpentine series feed networks, similar to that illustrated in Figure 1.3. As the operating frequency is varied, the electrical length of the feed between elements also varies and a frequency-dependent progressive phase-shift is generated. With this technique, beam steering is achieved without the need of additional circuit components.

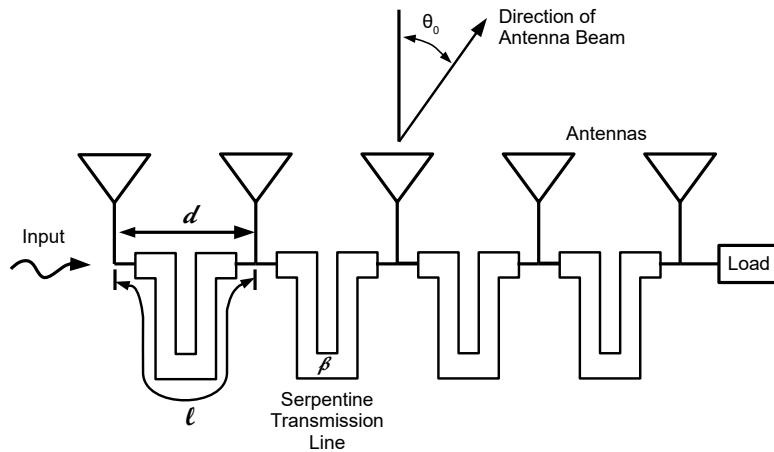


Figure 1.3: Frequency Scanned Antenna Array.

In radar applications, target range resolution is determined by the available bandwidth of the system. This typically limits the use of frequency for other purposes, such as angular beam steering or

frequency hopping for electronic counter-countermeasures. At millimetre-wave frequencies, the significantly increased available bandwidth reduces this limitation. For commercial applications, where electronic counter-countermeasures and varying pulse frequencies are not required, the use of this additional bandwidth for angular scanning becomes particularly attractive.

### 1.3 Waveguide-fed Slot Arrays

Waveguide-fed slot arrays are commonly used in radar applications. These arrays radiate electromagnetic energy through slots cut in the side wall of a feeding rectangular waveguide. They offer a number of attractive features arising from their physical simplicity, as the feeding network and radiating elements are unified in a planar structure. They benefit from low losses, high-power capability, and relative simple fabrication, making them well suited for MMW applications. As a result, they have been well studied and successfully implemented for MMW frequencies up to 100's of GHz [12–14].

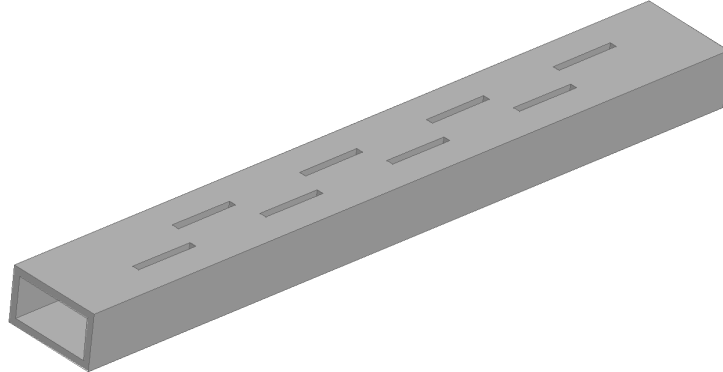


Figure 1.4: Slotted Waveguide.

A slot cut in a rectangular waveguide acts as a form of aperture antenna. Directive arrays are implemented by cutting multiple slots in a waveguide, as seen in Figure 1.4. These array antennas can be designed for specified radiation patterns as the excitation magnitude and phase of each element can be controlled through varying slot size, shape, and location.

Historically, significant efforts were made to characterize the behaviour of slots and develop methods to design arrays. The theoretical radiation and impedance properties of an isolated slot in a waveguide were first studied by Stevenson [15]. This work was extended by Elliott and Kurtz to develop a design method for arrays of slots in a waveguide excited by a standing wave [16] that was subsequently adapted by Elliott to permit the design of arrays excited by traveling waves [17]. These methods relied on previously measured characteristics of an isolated slot as a function of its geometry. In accounting for

mutual coupling and other higher order effects, a pair of non-linear design equations were derived that may be solved iteratively for a set of physical slot parameters (e.g. lengths and positions) that produce a desired radiation pattern. In recent years, the availability of commercial finite element analysis software and increased computational resources has permitted the efficient characterization of a waveguide-fed slot in an array environment [18, 19]. A slot may be characterized for a set of physical parameters and the results used to design arrays directly, i.e. without iteration.

When excited by a travelling wave, a frequency-dependent phase shift between successive slot excitations arises due to their physical spacing. In fixed-beam applications, this is considered a detriment to performance because the antenna's beam will squint, or deviate from the design angle as frequency varies. For frequency-scanning applications, the phase shift in a linear waveguide is typically insufficient to provide a meaningful amount of angular scanning. By meandering the waveguide as seen in Figure 1.5, frequency-scanning arrays can be implemented with specified scanning characteristics. The required shift is produced by the length of waveguide, while the spacing between radiating slots can be maintained sufficiently small to prevent the generation of grating lobes. This approach was frequently used in the past for scanning radars [20, 21], and has more recently been utilized for MMW radar systems [7, 22].

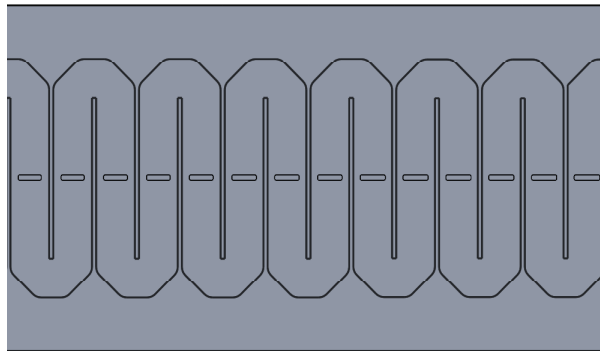


Figure 1.5: Meandered Slotted Waveguide.

A classical limitation of travelling-wave slot arrays is the inability to radiate toward the broadside of the antenna. Each slot in the array generates a small reflected wave; when the slots are excited in phase, these reflections add coherently resulting in the well-known scanning blindness condition at broadside. In order for a slot array to radiate at broadside, the reflections from each individual slot must be suppressed. This is typically achieved through introducing an additional discontinuity in the waveguide a quarter wavelength from the radiating slot. The simplest being a similar slot, however pits, posts, and walls have also been proposed [23–26].

## 1.4 Objectives and Proposed Design

The objective of this thesis is to design a planar frequency-scanned antenna that is suitable for use in MMW surveillance radar applications. To this effect, the antenna must meet the requirements qualitatively described above. To guide the design process, a set of quantitative specifications, found in Table 1.1, were selected based on commercially available radars [8] and relaxing some requirements to facilitate an economical implementation that still provides adequate performance. The designed antenna will be implemented and utilized in a simplified radar system to demonstrate its application.

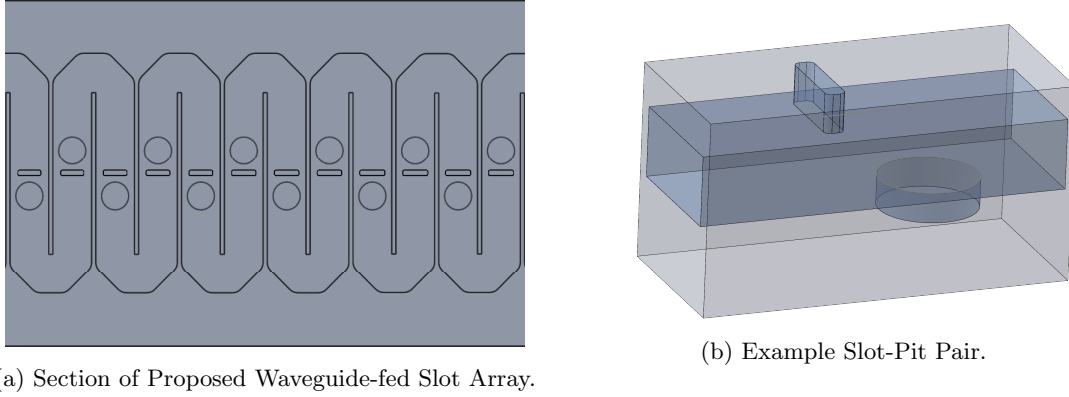
Specification	Value
Center Frequency	34.3 GHz
Total Bandwidth	1.8 GHz
Range Resolution	1.5 m
Maximum Scan Angle	20°
Scanning Beam width	2°
Side Lobe Levels	20 dB
Polarization	Vertical

Table 1.1: Proposed Radar and Antenna Specifications.

The proposed antenna is based on a travelling-wave slot array; a section of which is depicted in Figure 1.6(a). It consists of a serpentine rectangular waveguide with transverse slots cut in the broad wall. Using a standard WR22 cross-section for the waveguide simplifies the integration with a radar front end, allowing standard waveguide components and coaxial transitions to interface with the antenna. In this geometry, transverse slots provide linear vertical polarization which is beneficial for surface-based surveillance radars, as the effects of multipath reflections from the ground are reduced [10]. Furthermore, transverse slots simplify the design process, as their excitation magnitude is controlled solely by adjusting their length.

Reflection cancelling circular pits are embedded in the bottom broad wall of the waveguide. For the geometry shown in Figure 1.6(a), the addition of reflection cancelling slots was found to introduce secondary grating lobes that required additional baffles to reduce, significantly increasing the antenna's size [27, 28]. The use of a non-radiating reflection cancelling pit allows for broadside radiation without introducing secondary grating lobes and maintains the antenna's planar structure. Furthermore, when implemented in a frequency-scanned array, the serpentine length can be adjusted to correct any error in slot excitation phase resulting from the introduction of the pits. This allows the physical spacing of the slots to be maintained constant which is typically not the case for reflection-cancelling arrays in linear waveguides [29]. The result is a simplified design process, where slot excitation magnitude and phase can be designed independently. An example slot-pit pair is depicted in Figure 1.6(b) as it would appear

in a waveguide of practical thickness.



(a) Section of Proposed Waveguide-fed Slot Array.

(b) Example Slot-Pit Pair.

Figure 1.6: Proposed Design.

In applications requiring increased angular coverage, two identical antennas may be co-located and oriented such that their beams steer in opposite directions with frequency. To allow for this, while maintaining an overall planar configuration, the antenna will be designed to scan from broadside to a maximum scan angle over the range of its operating bandwidth. An example of one possible configuration of this concept is depicted in Figure 1.7. A single transmitting antenna with a wide beam width illuminates the entire surveillance area and two frequency-scanned arrays are used as receivers to determine the direction multiple targets.

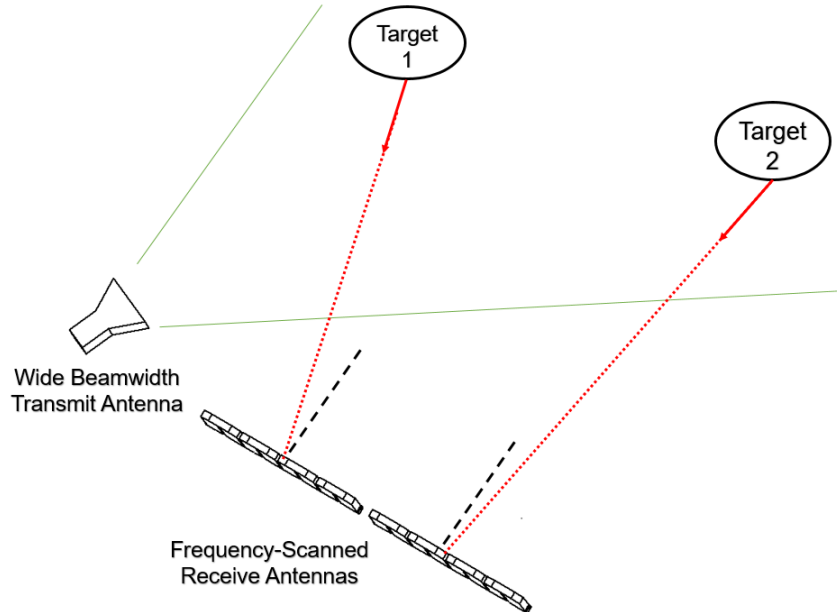


Figure 1.7: Multiple Antenna Configuration.

A prototype of the proposed antenna can be manufactured through standard Computer Numerical

Control (CNC) milling techniques. A milling machine can carve the waveguide channel and pits from a block of conducting metal and the slots from a thin sheet of aluminum. Bolting these components together completes the antenna.

## 1.5 Thesis Outline

The thesis is divided into six chapters. Chapters 2, 3, and 4 review background information relevant to this work. Chapter 2 presents the fundamental theory necessary to analyze general antenna array performance and synthesized desired radiation patterns. Chapter 3 introduces the waveguide-fed slot array and its principles of operation. Design methods for waveguide-fed slot arrays and frequency scanning arrays are then introduced and discussed. Chapter 4 then covers the fundamentals of frequency modulated radar and its application with frequency scanning.

Chapter 5 will outline the design process of the proposed antenna. Detailed design of the waveguide and slot-pit pairs will be presented as well as the overall array design to meet the proposed specifications. Simulated radiation patterns will show the antenna's predicted performance.

Chapter 6 presents the implementation of the waveguide-fed slot array and its experimental performance. The experimental results will be compared to the simulation predictions and similarities and discrepancies will be discussed.

Chapter 7 details a simple radar experiment representing the practical application of the antenna. A radar will be implemented using laboratory equipment and commercial components. The received radar signals will be presented and used to generate radar images displaying the location of targets in range and angle.

The final chapter will conclude the research findings and discuss future designs and applications that may be further explored.

# Chapter 2

## Antenna Array Theory

This chapter will review the relevant theory pertaining to the analysis and design of antenna arrays. This fundamental theory forms the basis for the design of the proposed frequency-scanned waveguide-fed slot array. Basic array factor theory will first be reviewed, including definitions and mathematical expressions predicting an array's performance. Secondly, the concept of a frequency scanning array is introduced and equations describing its behaviour presented. Finally, methods to design conceptual arrays meeting specific performance requirements are discussed. Reference [30] contains additional details and derivations relevant to the information presented here and may be referred to accordingly.

### 2.1 Antenna Array Fundamentals

An antenna array is a set of individual antennas arranged and excited in such a manner to act as a single antenna with specified radiation characteristics. Antenna arrays are used to achieve directive radiation patterns, focusing the energy radiated in a desired direction while simultaneously reducing energy directed elsewhere. In radar applications, this provides a number of benefits [10]. For a fixed transmitter power, the concentration of the radiated energy increases the maximum range the radar can observe. Conversely, for a specified range, required transmitted power is reduced, typically resulting in a more compact design. Additionally, the directive radiation pattern acts as a spatial filter in the angular domain, rejecting signals from undesired directions, thus allowing the radar to determine the angular position of a target. In general, antenna arrays achieve their high directivity through increasing their aperture size and total number of elements.

### 2.1.1 Principle of Pattern Multiplication

The radiation pattern of an antenna describes the directional dependence of its various radiation properties. It is typically used to describe field strength or radiation intensity. The analysis of array radiation patterns is simplified through the principle of pattern multiplication. The total pattern of an array is modelled as the product of an individual element's pattern with an array factor. The array factor may be thought of as the radiation pattern that would be obtained if the array's discrete elements were isotropic radiators. This principle can be expressed for an antenna's field strength pattern as

$$f_{\text{tot}}(\theta, \phi) = f(\theta, \phi) AF(\theta, \phi) \quad (2.1)$$

where  $f_{\text{tot}}(\theta, \phi)$  is the total array field pattern,  $f(\theta, \phi)$  is the field pattern of an individual element, and  $AF(\theta, \phi)$  is the array factor.

It is often convenient to view an antenna's radiation pattern in terms of its radiation intensity, or power radiated per unit solid angle. In this case, it is referred to as a power pattern and from extension of (2.1) is given by

$$U_{\text{tot}}(\theta, \phi) = U(\theta, \phi) |AF(\theta, \phi)|^2 \quad (2.2)$$

where  $U_{\text{tot}}(\theta, \phi)$  is the total array radiation intensity, and  $U(\theta, \phi)$  is the field pattern of an individual element.

In practice, array elements are small antennas with broad patterns. Thus, the array factor is usually sufficient to predict array performance and appropriate for initial design work.

### 2.1.2 Array Factor Determination

The configuration of a general linear array is depicted in Figure 2.1.  $M$  antenna elements are placed along the  $x$ -axis an equal distance,  $d$ , apart. The distance from each element to the observation point is denoted  $r_n$ . Each element is excited by a complex current  $I_n$ . The resulting array factor is given by

$$AF = \sum_{n=0}^{M-1} I_n e^{-jk_0 r_n} \quad (2.3)$$

where  $k_0 = 2\pi/\lambda_0$  is the free space wavenumber.

Equation (2.3) can be further simplified with a far-field assumption that the distance from any element to the observation point is much greater than the total array length,  $(M - 1)d$ . The result of this assumption is that the  $\theta$  and  $\phi$  coordinates of the field point are the same with respect to each

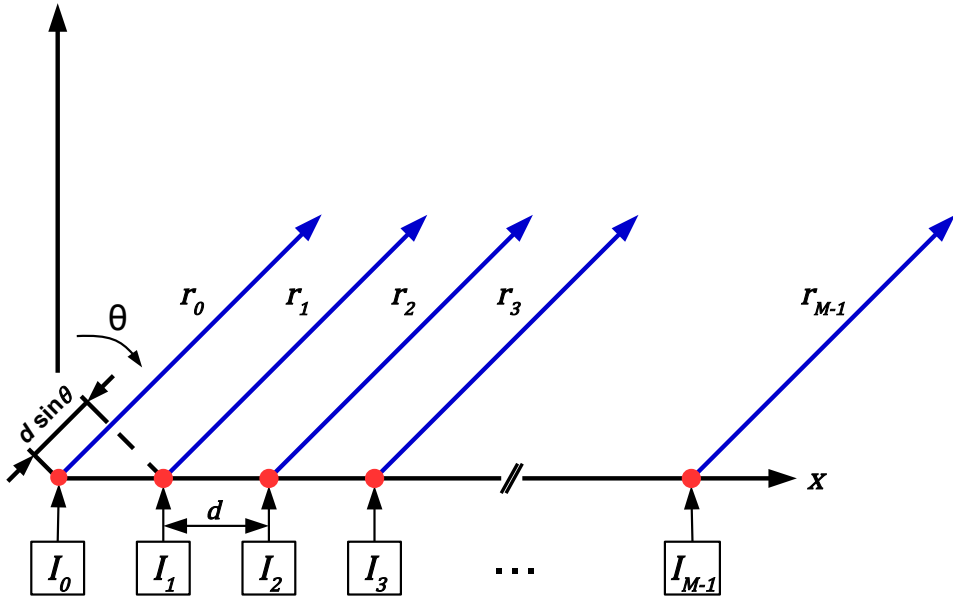


Figure 2.1: Linear Array.

element. Thus,  $r_n$  can be replaced with  $r_0 - nd \sin \theta$  in the exponential term of the summation and the common phase term  $e^{-jk_0 r_0}$  is typically dropped. In many applications, there is a uniform progression in the phase of the excitation currents, and the currents may be written as

$$I_n = A_n e^{-j n \alpha} \quad (2.4)$$

Then, the array factor can be simplified as

$$AF(\psi) = \sum_{n=0}^{M-1} A_n e^{j n \psi} \quad (2.5)$$

where

$$\psi = k_0 d \sin \theta - \alpha \quad (2.6)$$

### 2.1.3 Properties of Linear Arrays

The array factor given by Equation (2.5) can provide insight into the behaviour and performance characteristics of many practical arrays. Of particular interest is the location of principle maxima, relative values of secondary maxima, directivity and gain, and beamwidth. In this discussion, a uniform linear array, the simplest configuration, will be analyzed; however, the concepts may be similarly applied to more complex linear arrays. Additional details regarding the impact these properties have on radar

systems can be found in reference [10].

In a uniform array, the excitation magnitudes of all elements are equal, and by taking the magnitude of Equation (2.5) and using algebra, a normalized array factor can be expressed

$$|AF_n(\psi)| = \left| \frac{\sin \frac{M\psi}{2}}{M \sin \frac{\psi}{2}} \right| \quad (2.7)$$

Noting that Equation (2.7) is similar to a sinc function of  $\psi$  but is periodic in  $2\pi$ , it can be further analyzed to observe a number of properties of linear arrays.

### Principle Maxima and Main Beam Direction

The normalized array factor, (2.7), produces principle maxima for

$$\psi = \pm 2\pi m, \quad m = 0, 1, 2, 3, \dots \quad (2.8)$$

The angular position of these maxima,  $\theta_m$ , can be obtained by equating (2.6) and (2.8) and solving

$$\sin \theta_m = \frac{\alpha}{k_0 d} \pm \frac{2\pi m}{k_0 d}, \quad m = 0, 1, 2, 3, \dots \quad (2.9)$$

The lobe containing the  $m = 0$  maximum is generally referred to as the main beam and the direction it points,  $\theta_0$ , is the steering angle of the array. The steering angle is easily found from Equation (2.9) as

$$\theta_0 = \sin^{-1} \left( \frac{\alpha}{k_0 d} \right) \quad (2.10)$$

This relation demonstrates the ability of a phased array to scan its main beam. Through control of the progressive excitation phase shift,  $\alpha$ , the maximum radiation can be steered in a desired direction. In phased arrays, this is accomplished by feeding elements with electronically controlled ferrite or diode phase shifters. In frequency-scanned arrays, this phase shift is controlled through a frequency-dependent feed.

Lobes containing maxima which occur for values of  $m$  other than zero are called grating lobes. In many applications, their appearance is a detriment to performance. In these cases, the element spacing,  $d$ , must be sufficiently small to ensure Equation (2.9) only has a solution for  $m = 0$ . An element spacing of  $\lambda_0/2$  is often selected to ensure only the main beam appears in the visible angular range  $-\pi \leq \theta \leq \pi$ .

Larger spacings may be used without generating grating lobes provided that

$$d \leq \frac{\lambda_0}{1 + |\sin \theta_0|} \quad (2.11)$$

### Secondary Maxima and Side Lobe Levels

The normalized array factor also produces secondary (local) maxima. These maxima are referred to as side lobes and occur approximately where

$$M\psi = \pm (2s + 1)\pi, \quad s = 1, 2, 3, \dots \quad (2.12)$$

Thus from Equation (2.6), side lobes occur at angles

$$\theta_s = \sin^{-1} \left( \frac{\alpha}{k_0 d} \pm (2s + 1) \frac{\pi}{M k_0 d} \right), \quad s = 1, 2, 3, \dots \quad (2.13)$$

where  $s = 1$ , corresponds to the first side lobe,  $s = 2$  the second, and so on. The side lobe level (SLL) is typically defined as the magnitude of the largest secondary maximum, measured in decibels, relative to the peak magnitude of the main beam. For large uniform arrays, the first side lobe is largest and its SLL is approximately 13.5 dB lower than the maximum of the main beam.

### Directivity and Gain

Two important and related figures of merit of antenna performance are directivity and gain. Their values provide a measure of an antenna's ability to focus its radiated power in a particular direction. Directivity describes this ability with respect to only the radiation pattern, while gain accounts for the power lost in the antenna itself.

Directivity may be defined as the ratio of power radiation intensity in a specified direction to the average radiation intensity. This may be formulated as

$$D(\theta, \phi) = \frac{4\pi U(\theta, \phi)}{\iint U(\theta, \phi) d\theta d\phi} \quad (2.14)$$

The magnitude squared of the array factor given in (2.7) can be substituted for the radiation intensity in this expression to obtain an approximation of the maximum directivity,  $D_o$ , of a uniform array. The result is

$$D_o \approx \frac{2Md}{\lambda_o} \approx \frac{2L}{\lambda_o} \quad (2.15)$$

where  $L$  is the approximate physical length of the array. Equation (2.15) shows the important relation between the maximum directivity and the size of the array. Thus, a large directivity requires a long, relative to wavelength, array.

The gain of an antenna is similar to its directivity, however it accounts for conductor and dielectric dissipation losses in the antenna. It can be expressed as

$$G(\theta, \phi) = \epsilon_r D(\theta, \phi) \quad (2.16)$$

where  $\epsilon_r$  is the radiation efficiency of an antenna and is the ratio of radiated power to input power. In radar applications, where maximum range is largely dependent on actual power transmitted or received, gain is more commonly used as a design specification than directivity.

### Half Power Beamwidth

The half-power (or 3dB) beamwidth of an antenna is defined as the angle between two directions where the radiation intensity is one-half the maximum in a plane containing the beam maximum. An approximation for the half power beamwidth of the uniform linear array is found by setting the magnitude squared of the normalized array factor in (2.7) to one half. The resulting expression is

$$\theta_{BW} \approx \frac{2.65\lambda_o}{\pi M d} \quad (2.17)$$

In many applications this approximation is reduced to simply

$$\theta_{BW} \approx \frac{\lambda_o}{L} \quad (2.18)$$

Comparing Equations (2.17) and (2.15) shows an important relation between beamwidth and maximum directivity. That is, an narrow beamwidth implies a large directivity and vice versa. This reinforces the requirement of a large array to ensure a narrow beamwidth.

The above approximations are applicable for a beam directed toward broadside. If the beam is steered to an angle,  $\theta_o$ , the approximations must be adjusted to account for the reduction in the projected array length,  $L' = L \cos(\theta_o)$ . Thus, for scanning arrays the beamwidth may be estimated by

$$\theta_{BW}(\theta_o) \approx \frac{\lambda_o}{L \cos(\theta_o)} \quad (2.19)$$

## 2.2 Frequency Scanned Arrays

Frequency scanned arrays achieve beam steering through varying their frequency of operation. These arrays are typically implemented using series feed networks. By feeding an antenna array with a serpentine structure as seen in Figure 2.2, a progressive phase shift,  $\alpha$ , that varies with frequency is generated. With  $\alpha$  given by

$$\alpha = \frac{2\pi fl}{v} = \frac{2\pi l}{\lambda_0} = k_o l \quad (2.20)$$

where  $f$  is the operating frequency of the antenna,  $l$  is the length of transmission line between adjacent elements, and  $v$  is the propagation velocity in the transmission line. To simplify this analysis,  $v$  is assumed to be equal to the speed of light in a vacuum,  $c$ , and the substitution  $v/f = \lambda_0$  is used. Additionally, the expressions derived for a uniform linear array will be used. It may, however, be noted that the frequency scanning behaviour is the same for tapered excitations with uniform phase progressions.

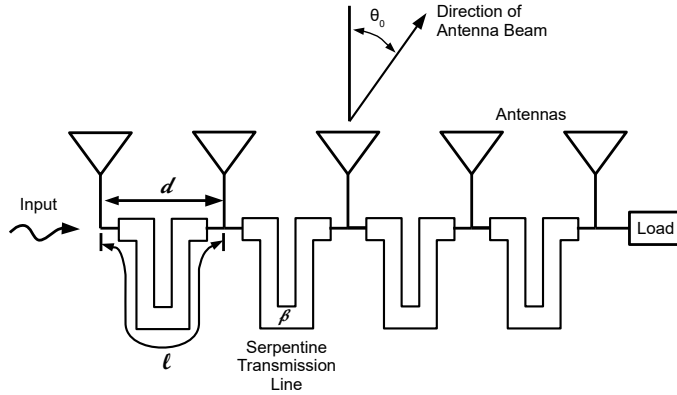


Figure 2.2: Frequency Scanned Antenna Array.

From the discussion on linear array properties, the directions in which principle maxima occur in the uniform linear array factor were given in Equation (2.9). Substituting the frequency-dependant phase-shift into this equation yields an expression for the location of array factor maxima as a function of wavelength

$$\begin{aligned} \sin \theta_m &= \frac{l}{d} \pm \frac{2\pi m}{k_o d} \\ &= \frac{l}{d} \pm \frac{m\lambda_0}{d}, \quad m = 0, 1, 2, 3, \dots \end{aligned} \quad (2.21)$$

It was stated that for linear arrays the value of  $m = 0$  is generally taken as the location of the main lobe. In frequency scanning applications, it is convenient to set  $m = l/\lambda_c$ , where  $\lambda_c$  is the wavelength corresponding to the main lobe occurring at broadside. This is equivalent to setting the transmission

line length to be an integer number of wavelengths at broadside. Taking the negative sign in Equation (2.21), and substituting the expression for  $m$ , gives a simplified expression for the location of the main beam maximum

$$\sin \theta_m = \frac{l}{d} \left( 1 - \frac{\lambda_o}{\lambda_c} \right) = \frac{l}{d} \left( 1 - \frac{f_c}{f} \right) \quad (2.22)$$

where  $f_c$  is the operating frequency that steers the beam to broadside.

Equation (2.22) provides some insight into the behaviour and design of frequency-scanned arrays. The ratio  $l/d$  determines how rapidly the beam will scan as a function of frequency. An initial design for an array can begin by determining a minimum element spacing from Equation (2.11). The serpentine length can then be calculated for a specified scan angle and frequency range.

### 2.2.1 Bandwidth Considerations

From the above discussion, it is apparent that for an antenna to scan a large angular region, it must either use a large frequency range or a large ratio of  $l/d$ . Increasing  $l/d$  and thus the beam scanning rate however, limits the available signal bandwidth at a given angle. As the beam scans continuously with frequency, a finite angle will correspond to zero bandwidth. A common method to establish a bandwidth for a fixed angle is to allow the beam to steer over a range of angles corresponding to its width. It is assumed the beam is fixed at the center angle and the range of frequencies specifies the bandwidth available at this angle. Increasing the scan rate or  $l/d$ , therefore reduces the bandwidth available at each fixed steering angle.

The bandwidth available using the above method can be expressed

$$\Delta B = \frac{df}{d\theta_o} \theta_{BW} \approx \frac{df}{d\theta_o} \frac{\lambda_o}{Md} \quad (2.23)$$

where the beamwidth approximation (2.18) was used. Differentiating Equation (2.22) gives

$$\Delta B = \frac{f}{f_c} \frac{\cos \theta_o}{(l/d)(Md/c)} \quad (2.24)$$

This equation illustrates the trade-off between available bandwidth, beamwidth, and total angular scan range. For a given scan angle, the available bandwidth is inversely proportional to both the  $l/d$  ratio and product,  $Md$ , the latter of which is required to be large for a narrow beam width.

## 2.3 Array Pattern Synthesis

The first section of this chapter introduced the concept of the array factor or pattern and derived a number of expressions describing the performance of an array based on the excitation of its elements. In the design of arrays however, the reverse of this process is desired and referred to as array pattern synthesis. The excitation of the array's elements should be designed such that the antenna's radiation pattern meets a set of design specifications. In this work, the design of arrays with the minimum beamwidth for a specified side lobe level is of particular interest.

There are a number of antenna synthesis techniques; here, Schelkunoff's polynomial representation of the array factor is presented. This method achieves specified radiation characteristics through proper placement of nulls in an array's radiation pattern.

Schelkunoff's method begins with the array factor as expressed in Equation (2.5) and by letting

$$z = e^{j\psi} = e^{j(k_0 d \sin \theta - \alpha)}. \quad (2.25)$$

The array factor can then be expressed as a function of the complex variable  $z$

$$AF(z) = \sum_{n=0}^{M-1} A_n z^n = A_0 + A_1 z + a_2 z^2 + \dots + A_{M-1} z^{M-1}. \quad (2.26)$$

This is a polynomial of degree  $(M - 1)$ , thus has  $(M - 1)$  roots. Equation (2.26) can also be expressed as a product

$$\begin{aligned} AF(z) &= A_{M-1}(z - z_1)(z - z_2)(z - z_3)\dots(z - z_{M-1}) \\ &= A_{M-1} \prod_{n=1}^{M-1} (z - z_n) \end{aligned} \quad (2.27)$$

where  $z_n$  are the  $M - 1$  roots of  $AF(z)$ . For the array factor to be a real valued function, the complex zeros,  $z_n$ , must occur in conjugate pairs.

The benefit of Equation (2.27) is through an appropriate transformation, the roots of the array factor can be mapped to those of a known polynomial exhibiting the desired characteristics of the radiation pattern. From the substitution (2.25), the progressive phase shift of the excitations is included in  $z$  and thus only the magnitude of the excitation need be determined. Consequently and without loss of generality,  $\alpha$  may be set to zero, corresponding to maximum radiation at broadside. Equating (2.26) and (2.27) then yields these magnitudes for a given element spacing,  $d$ . The progressive excitation phase,  $\alpha$ , for a specified steering angle can then be determined using Equation (2.10).

Two sets of polynomials commonly used in array designs to obtain element excitation magnitudes are the Chebyshev polynomials and the related Taylor-Villeneuve patterns. These polynomials produce array factors with defined side lobe levels and optimal narrow beamwidths.

### 2.3.1 Dolph-Chebyshev Array

In Section 2.1.3 it was noted that a uniform linear array will exhibit a first side lobe in its radiation pattern approximately 13.5 dB below the maximum. In many applications, particularly in radar systems, lower side lobe levels are desired. These levels can be reduced through tapering the excitation magnitude of the array elements from a maximum at the center to lower values at the edges. This tapering however, reduces the effective length of the array, increasing the antenna's beamwidth and reducing its maximum directivity. The resulting compromise between side lobe level and directivity is one consideration in the design of arrays.

To optimize the trade off between side lobe levels and beamwidth, Dolph [31] introduced an array factor based on the Chebyshev polynomials. These Dolph-Chebyshev arrays are considered optimum in that they produce radiation patterns with a minimum beamwidth for a specified side lobe level or conversely, a minimum side lobe level for a specified beamwidth. They achieve this by ensuring all side lobe maxima are equal.

The Chebyshev polynomials are given by

$$\begin{aligned} T_m(x) &= \cos[m \cos^{-1}(x)] \quad \text{for } -1 \leq x \leq 1 \\ T_m(x) &= \cosh[m \cosh^{-1}(x)] \quad \text{for } |x| > 1 \end{aligned} \tag{2.28}$$

where  $m$  is the order of the polynomial. Chebyshev polynomials exhibit a number of important properties relevant to antenna radiation patterns. All order polynomials pass through the point  $(1,1)$ . For  $|x| \leq 1$  the polynomials' values range between -1 and 1. Additionally, all roots occur in this domain and are separated by local maxima and minima, having values of only +1 or -1,

Using the Dolph transformation

$$x = x_0 \cos\left(\frac{\psi}{2}\right) \tag{2.29}$$

the array factor for an  $M$  element array can be equated to a Chebyshev polynomial of order  $m = M - 1$ . This transformation allows the beneficial properties described above to be mapped to the design parameters of an array pattern. Side lobes in the array pattern occur between its nulls, thus their locations will be restricted to the range of  $\psi$  that maps to  $|x| \leq 1$ . It follows that all side lobes will have equal magnitude. Finally, it was shown in Section 2.1.3 that an array's pattern maximum occurs

for  $\psi = 0$ , and from Equation 2.29, this corresponds to a  $x = x_o$  where  $x_o > 1$ . The value  $R = T_m(x_o)$  will be the pattern maximum relative to the side lobe levels.

As the location of the roots of  $T_m(x)$  are known and given by

$$x'_n = \cos \left[ \frac{(2n-1)\pi}{(2m)} \right], \quad n = 1, 2, 3 \dots m \quad (2.30)$$

the roots of the array factor as a function of  $\psi$  or  $z$  can be found through equations (2.29) and (2.25). Their determination is simplified, as the roots are symmetric with  $x_n = -x_{(m+1)-n}$ , for  $n \leq m/2$ . These roots can be used with Schelkunoff's method to obtain the required excitation magnitudes.

In summary, the design process for a broadside Dolph-Chebyshev array for a specified side lobe level,  $R$ , and given number of elements,  $M$ , and spacing,  $d$  is:

1. Use the Chebyshev polynomial,  $T_m(x)$ , of order  $m = M - 1$
2. Determine the value of  $x_o$  by equating (2.28) to  $R$  and invert:

$$x_o = \cosh \left[ \frac{\cosh^{-1}(R)}{m} \right] \quad (2.31)$$

3. Obtain  $x'_n$ , the roots of  $T_m(x)$ , using Equation (2.30)
4. Calculate the roots of the array factor as a function of  $\psi$ , using the inverse of Equation (2.29):

$$\psi'_n = 2 \cos^{-1} \left[ \frac{x'_n}{x_o} \right] \quad (2.32)$$

5. Use the Schelkunoff transformation,  $z_n = e^{\psi'_n}$ , and substitute into Equations (2.26) and (2.27) to obtain the required excitation magnitudes  $A_n$

One characteristic of Dolph-Chebyshev arrays with large number of elements, is that the excitation magnitudes of edge elements become large relative to the remaining elements. In many practical arrays, these excitations can be difficult to achieve. For this reason, alternative polynomials that provide a specified maximum side lobe levels have been developed.

### 2.3.2 Taylor-Villeneuve Array

Taylor-Villeneuve arrays are commonly used in applications of arrays of discrete elements, such as waveguide-fed slot arrays, to practically achieve low side lobe levels. Taylor [32] first derived an ideal equal-side-lobe distribution for continuous line source antennas based on the Dolph-Chebyshev array. A

modified pattern was also developed where only the first  $\bar{n}$  side lobes on either side of the main beam were maintained at equal levels, while side lobes further from the main beam decayed as  $\frac{\sin x}{x}$ . The result was a distribution with finite values at its edges and slightly larger beamwidths when compared to the optimal Dolph-Chebyshev array.

Villeneuve [33] extended Taylor's approach to arrays of discrete elements. A polynomial is generated from the first  $\bar{n} - 1$  zeros of a Dolph-Chebyshev pattern on either side of the array factor's maximum. The remaining zeros are obtained by replacing the zeros of the Dolph-Chebyshev pattern with those of a uniform linear array. The result is an array factor equivalent to the modified Taylor pattern, from which discrete excitation magnitudes can be obtained using Schelkunoff's method.

In the previous section, it was stated that the main beam of the array factor in terms of  $\psi$  is mapped to the Chebyshev function at the value of  $x_0$ . By nature of the Chebyshev polynomials' (anti)symmetry and the periodicity of the array factor, this is equivalent to being mapped to the value at  $-x_0$ . Thus for  $\bar{n}$  equal level side lobes, the  $\bar{n} - 1$  zeros nearest to  $x_0$  and  $-x_0$  must be used in the array factor polynomial.

In Section 2.1.3, it was shown that the array factor for the uniform linear array has a periodic sinc shape. This is the desired shape for the Villeneuve pattern away from the main beam. For  $A_n = 1$ , the array factor can be expressed

$$AF(z) = \sum_{n=0}^{M-1} A_n z^n = \frac{1 - z^M}{1 - z} \quad (2.33)$$

with zeros located at

$$z_n = e^{j 2\pi n / M}, \quad n = 1, 2, \dots, M - 1 \quad (2.34)$$

It follows from the Shelkunoff transform, (2.25), that the zeros of the uniform linear array factor as a function  $\psi$  are

$$\psi_n = \frac{2\pi n}{M}, \quad n = 1, 2, \dots, M - 1 \quad (2.35)$$

Once the required  $2(\bar{n} - 1)$  Chebyshev zeros,  $\psi'_n$ , are determined from Equation (2.30), the remaining roots can be found from Equation (2.35).

A final modification proposed by Taylor and Villeneuve is to shift the  $\psi'_n$  locations of the Chebyshev zeros such that the value of  $\psi'_{\bar{n}}$  corresponds to the value of  $\psi_{\bar{n}}$ . This is accomplished by multiplying all  $\psi'_n$  by a factor  $\sigma$  given by

$$\sigma = \frac{\bar{n}2\pi}{M\psi_{\bar{n}}} \quad (2.36)$$

Once all roots are determined, Schelkunoff's method can again be used to obtain the discrete element

excitations.

To summarize the design process for a broadside Taylor-Villeneuve array for a specified number of side lobes,  $\bar{n}$ , of equal magnitude,  $R$ , with a given number of elements  $M$ , and spacing,  $d$ :

1. Use the Chebyshev polynomial,  $T_m(x)$ , of order  $m = M - 1$
2. Determine the value of  $x_o$  by equating (2.28) to  $R$  and invert:

$$x_o = \cosh \left[ \frac{\cosh^{-1}(R)}{m} \right] \quad (2.37)$$

3. Calculate the required  $\sigma$  to shift the Chebyshev zeros,  $\psi'_n$ , from Equation (2.36)
4. Obtain the  $\bar{n} - 1$  roots of  $T_m(x)$  nearest  $x_o$  and the  $\bar{n} - 1$  nearest  $-x_o$ , using Equation (2.30). This corresponds to the zeros for  $n < \bar{n}$  and  $n > m + 2 - \bar{n}$ .
5. Calculate the shifted roots of the array factor as a function of  $\psi$ , using the inverse of Equation (2.29) and multiplying by  $\sigma$ :

$$\psi'_n = 2\sigma \cos^{-1} \left[ \frac{x'_n}{x_o} \right] \quad (2.38)$$

6. Determine the remaining roots of the array factor as a function of  $\psi$  from equation (2.34) for the remaining values of  $n$ .  $\bar{n} \leq n \leq m - \bar{n}$
7. Use the Schelkunoff transformation,  $z_n = e^{\psi'_n}$ , and substitute into Equations (2.26) and (2.27) to obtain the required excitation magnitudes  $A_n$

Figure 2.3 depicts a comparison of the array factor and relative amplitude distribution of 48-element Dolph-Chebyshev and Taylor-Villeneuve arrays. Both arrays have the same element spacing and are specified for -25 dB side lobe levels. For the Taylor-Villeneuve array,  $\bar{n} = 12$ . The array factors for both arrays have equal maximum side lobe levels. The equal valued side lobes characteristic of the Dolph-Chebyshev array are clearly seen, while the side lobes away from broadside in the Taylor-Villeneuve array factor are seen to decay. The most notable difference in the amplitude distribution is the relative values of the end element excitations. For the Dolph-Chebyshev array, the distribution is maximized at its ends, while this effect is reduced in the Taylor-Villeneuve array. As will be discussed in the next chapter, these relatively large amplitudes are difficult to achieve in travelling-wave designs like that of the proposed antenna of this work.

Figure 2.4 further illustrates the motivation behind the Taylor-Villeneuve array and the importance of the end element excitations. The array factor and amplitude distribution for a modified Dolph-

Chebyshev array are plotted. To achieve a more easily implemented amplitude distribution, the end element amplitudes are set to their nearest neighbour's value. The resulting array factor's side lobe values are no longer constant and decay at a faster rate than the Taylor-Villeneuve array. Moreover, an increase in beamwidth is observed as the reduction in end element excitation has shortened the effective length of the array. It follows that in specifying the number of constant-valued side lobes, the Taylor-Villeneuve array permits a compromise between the array's beamwidth and practical end excitation magnitudes, with larger  $\bar{n}$  values requiring larger end element amplitudes. To allow for this versatility in the design process, the Taylor-Villeneuve array factor will be incorporated in this work.

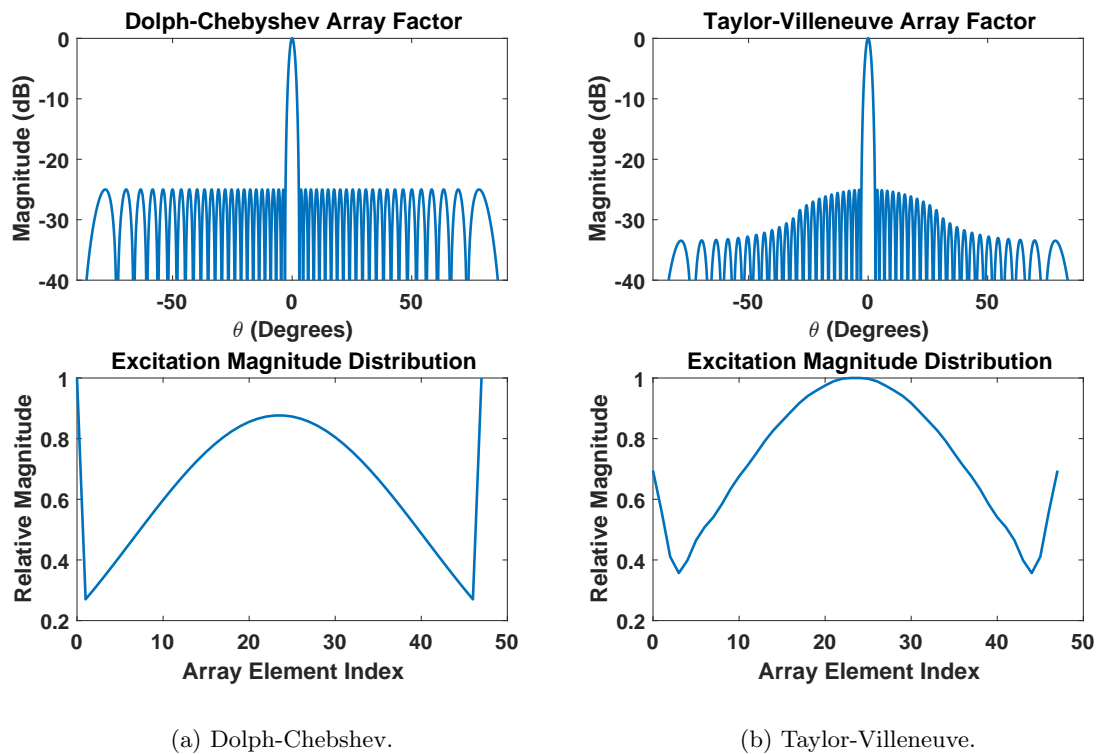


Figure 2.3: Array Factor and Amplitude Distribution Comparison.

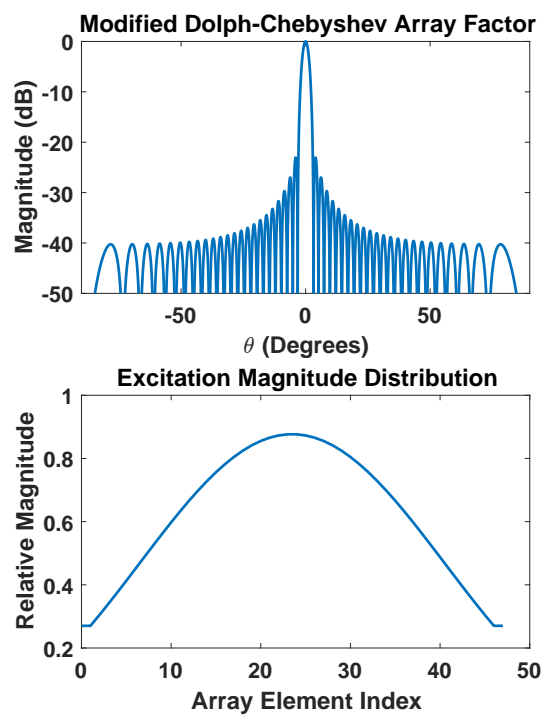


Figure 2.4: Modified Dolph-Chebyshev Array Factor.

## Chapter 3

# Waveguide-fed Slot Array Theory and Design

The waveguide-fed slot array is a phased array antenna consisting of slots cut in the wall of a rectangular waveguide. Widely used in radar applications at microwave and higher frequencies, these antennas feature low loss, simple fabrication and controllable excitation magnitudes. Electrically long arrays may be fabricated to achieve highly directive radiation patterns with low side lobe levels. They have been thoroughly studied, and modelling and design techniques for a number of configurations have been developed.

The proposed design of this work is based on a waveguide-fed slot array. Thus, a review of the principle of operation of the discrete slot antenna element and their implementation in arrays is presented first. Secondly, techniques to model and design arrays that produce the synthesized radiation patterns of Section 2.3 are introduced. The design of waveguide-fed slot arrays for frequency scanning applications is then discussed. Finally, fabrication technologies and practical considerations of manufacturing waveguide-fed slot arrays are addressed.

### 3.1 Slot Antenna

The discrete element of a slot array is the waveguide-fed slot aperture antenna. A slot in a wall of a rectangular waveguide interrupts currents on the surface, and an electric field is induced across the aperture. From the well-known behaviour of electromagnetic fields in a waveguide and knowledge of the field induced across the slot, equivalent circuit impedances and radiation behaviour can be determined.

These characteristics permit the implementation of arrays synthesized from the methods described in Section 2.3.

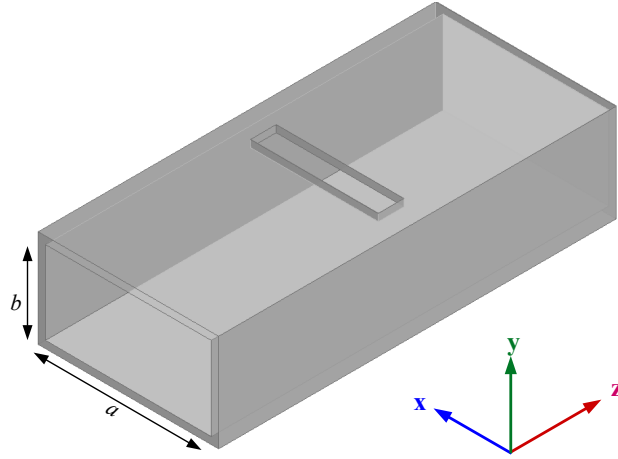


Figure 3.1: Waveguide-fed Slot Antenna.

An example of an isolated waveguide-fed slot is depicted in Figure 3.1. The dimensions of the interior broad and narrow walls are  $a$  and  $b$  respectively. It is assumed the waveguide is excited by the dominant TE<sub>10</sub> mode propagating in the positive z-direction. The normalized fields existing inside the waveguide of which are given in [34] as

$$\begin{aligned} H_z &= j \cos\left(\frac{\pi x}{a}\right) e^{-j\beta_{10}z} \\ H_x &= -\frac{\beta_{10}}{\pi/a} \sin\left(\frac{\pi x}{a}\right) e^{-j\beta_{10}z} \\ E_y &= -\frac{\omega\mu_0}{\pi/a} \sin\left(\frac{\pi x}{a}\right) e^{-j\beta_{10}z} \end{aligned} \quad (3.1)$$

$H_z, H_x$  are the  $z$ - and  $x$ -components of the internal magnetic field and  $E_y$  is the  $y$ -component of the electric field. The factor  $\beta_{10}$  is the propagation constant of the TE<sub>10</sub> mode and is given by

$$\beta_{10} = \sqrt{(k_0)^2 - \left(\frac{\pi}{a}\right)^2} = \frac{2\pi}{\lambda_g} \quad (3.2)$$

where the term,  $\lambda_g$ , in the right expression is the guided wavelength of fields propagating in waveguide. The vector surface current density on the walls of the waveguide can be found from the boundary condition of the magnetic field to a conductor

$$\mathbf{J} = \hat{\mathbf{n}} \times \mathbf{H}. \quad (3.3)$$

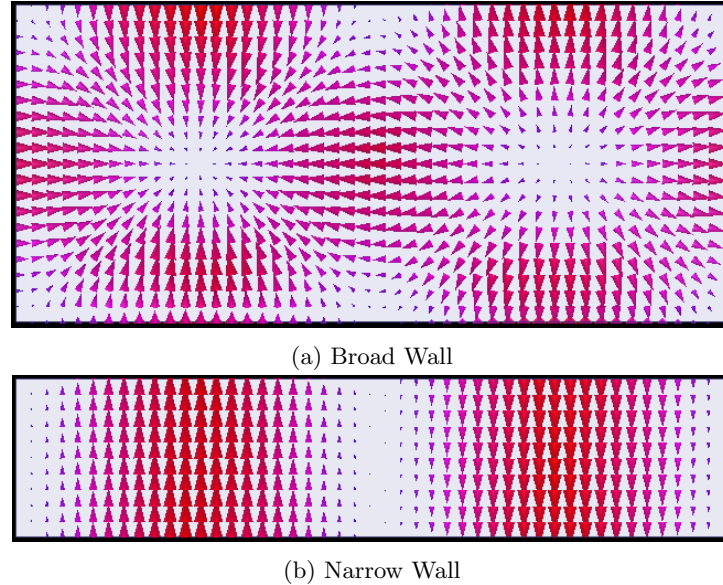


Figure 3.2: Vector surface currents of a rectangular waveguide

Figure 3.2 depicts the resulting vector surface currents on the broad and narrow walls. If a narrow slot is cut into the waveguide and interrupts this current, an electric field will be induced on the aperture. For example, the transverse slot depicted in Figure 3.1 interrupts the longitudinal component of the surface current on the broad wall. This induced field can be thought of as a displacement current, maintaining continuity in the conduction current. The magnitude of the aperture's electric field is proportional to the interrupted current. In the transverse slot example, its length can be adjusted to interrupt a specific amount of the current lines seen in Figure 3.2(a). It is this mechanism that allows waveguide-fed slot antennas to control their excitation magnitudes.

Waveguide-fed slots are generally modelled as series or shunt elements on a transmission line. Figures 3.3 and 3.4 depict a few typically used configurations of slots and their equivalent circuit models. Slots displacing longitudinal currents are modelled as series impedances, this includes the transverse slot and the rotated center slot. The longitudinal slot along the length of the waveguide, and the inclined sidewall slot interrupt transverse currents and are modelled as shunt elements. The magnitude of the modelled impedance or admittance is proportional to the induced electric field. The amount of displaced current, and thus slot excitation, can be controlled by varying slot parameters such as rotation, displacement, or length.

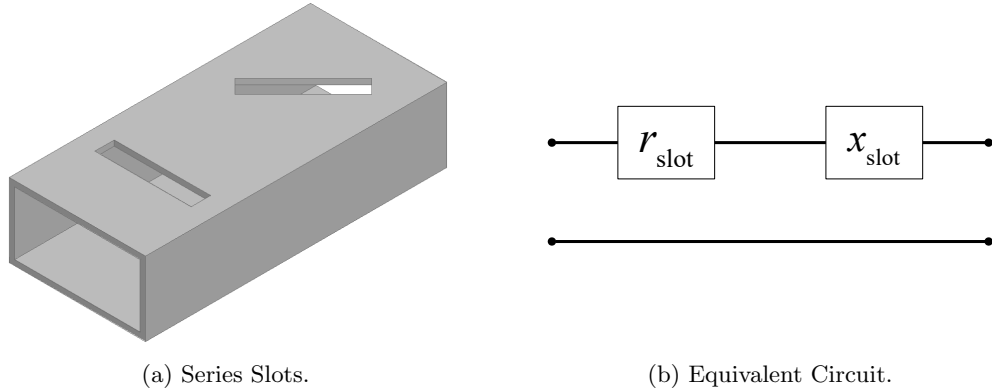


Figure 3.3: Series Slots and Their Equivalent Circuit.

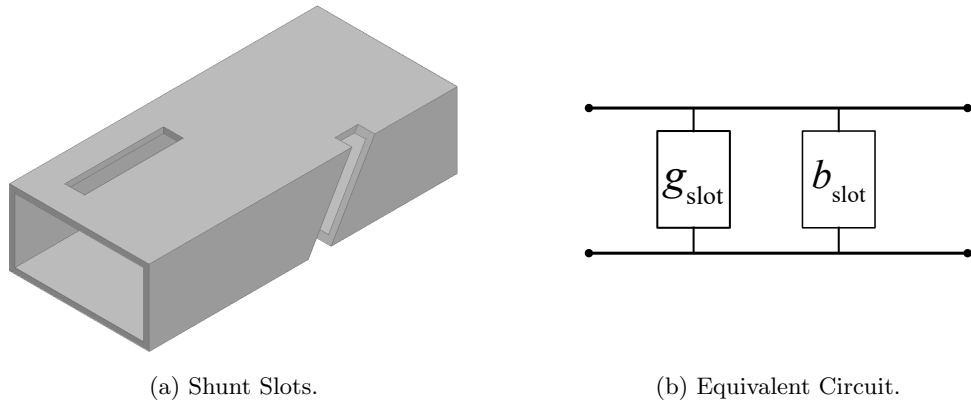


Figure 3.4: Shunt Slots and Their Equivalent Circuit.

To determine the radiated fields due to the induced field on the slot's aperture, the equivalence principle can be applied. An equivalent magnetic current [30] can be obtained from the aperture field using

$$\mathbf{M}_S = \mathbf{E}_a \times \hat{n} \quad (3.4)$$

where  $\mathbf{E}_a$  is the vector electric field on the aperture. For a resonant slot, with length,  $l \approx \lambda_0/2$ , and width,  $w \ll l$ , the magnitude of this electric field is, to a good approximation [34], given by

$$|\mathbf{E}_a(\zeta)| = V_m \sin \left[ k \left( \frac{l}{2} - |\zeta| \right) \right] \quad (3.5)$$

where  $\zeta$  is the distance from the slot's center. The narrowness of the slot permits the assumption that the electric field has only one component, pointing across its narrow dimension. For a slot oriented along

the z-axis, centred at the origin in the z-x plane, the resulting equivalent magnetic current is

$$\mathbf{M}_S(z) = \hat{z} V_m \sin \left[ k \left( \frac{l}{2} - |z| \right) \right] \quad (3.6)$$

Equation (3.6) can be recognized as having the same form as the electric current on a half-wave dipole. It follows that the narrow resonant slot and the half-wave dipole will have the same radiation patterns, with the exception that the roles of electric and magnetic fields are reversed. This is a consequence of the Duality Theory that arises due to symmetry in Maxwell's equations when fictitious magnetic sources are introduced. In this manner, the slot antenna is the dual of the dipole.

A number of radiation characteristics relevant to the design of waveguide-fed slot arrays can be inferred from the duality between the slot and dipole. As is the case for a dipole antenna, the slot's radiation pattern will be slightly directive in the plane containing the slot's length and uniform in the plane containing its width. Additionally, the directive pattern will contain nulls corresponding to the ends of the slot. A dipole's radiation is polarized along its length, thus duality dictates the slot's polarization will be along its width. From the principle of pattern multiplication, these characteristics will also exist in arrays of slots, and therefore must be considered in their design.

## 3.2 Waveguide-fed Slot Array Design

The design of waveguide-fed slot arrays is facilitated through an equivalent transmission line network. Slots are modelled as series or shunt elements fed in series by the transmission line equivalent to the rectangular waveguide's TE<sub>10</sub> mode. The power radiated by each slot is then determined by its impedance and the voltage or current that excites it. The benefit of this approach is that simple circuit analysis can be used to determine equivalent slot impedances that produce specified relative excitations obtained using array synthesis methods described in Chapter 2. The difficulty in designing waveguide-fed slot arrays is in determining equivalent circuit values for a slot as a function of its geometry in the waveguide.

### 3.2.1 Active Slot Impedance Determination

The concept of a slot's equivalent circuit model was introduced in the previous section. For the case of an isolated slot excited by two wires, a self-impedance can be obtained through its relation to its dual dipole antenna [35]. In a waveguide array environment, the determination of equivalent circuit parameters is more complicated. The slot's impedance is affected by the scattered fields, internal to the waveguide, that are generated by the slot itself and depend on its geometry and placement within

the waveguide. In addition, external mutual coupling between the radiated fields of nearby slots and internal mutual coupling between the scattered fields of nearby slots will contribute to a slot's active impedance. In the array environment, the slot's equivalent circuit parameters are referred to as its active slot impedance [34].

As mentioned in Chapter 1, computer-based full-wave solvers, such as Ansys' High Frequency Structure Simulator (HFSS), greatly simplify the determination of a slot's circuit equivalent in modern applications. These programs numerically solve a discretization of Maxwell's equations to obtain fields in a modelled volume subject to specified boundary conditions and excitations. The solved fields are used to characterize scattering matrices and radiation patterns of modelled structures.

To determine a slot's active impedance, a single waveguide-fed slot antenna may be modelled as depicted in Figure 3.5. A length of waveguide is modelled with a slot cut in a wall of finite thickness, representing the thickness of a practical waveguide. The total waveguide length is approximately one guided wavelength, and the slot is located at its centre. For this length, it is assumed only the TE<sub>10</sub> mode exists at each end of the waveguide where it is terminated by waveports. In this configuration, the waveports essentially act as ideal sources and terminations of the TE<sub>10</sub> mode. Thus, any scattered fields within the waveguide can be attributed to the presence of the slot. The region external to the waveguide is truncated with a radiation boundary. In planar array designs, the external region may be further reduced by assuming the slot is embedded in a ground plane as shown. The slot's equivalent impedance may be calculated from the solved model's scattering matrix using

$$Z_{\text{slot}} = 2 \frac{S_{11}}{1 - S_{11}} \quad (3.7)$$

The effects of mutual coupling can be approximated by replacing the radiation boundary with a periodic boundary condition (PBC) in the direction of the array's axis. Alternatively, the above process may be used to model a finite array of identical slots and interpolating the resulting impedance value for a single slot. A finite array model may provide a more accurate approximation and accounts for both internal and external mutual couplings. PBCs provide a more computationally efficient method by effectively modelling the radiation behaviour of an infinite array, but only external mutual coupling effects are included, thus, internal mutual coupling effects are unaccounted for.

Simulations are repeated as the slot's physical parameters are varied. In this manner, the slot's scattering matrix is characterized for a set of possible geometries. A set of achievable active impedances may be calculated from the scattering matrices and expressed as a function of the slot's physical parameters. Array design can then proceed with an equivalent transmission line network model.

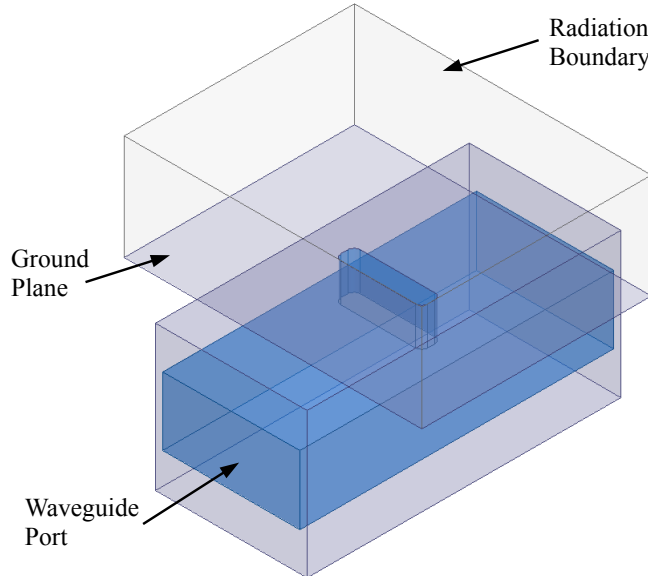


Figure 3.5: Slot Antenna Simulation Model.

### 3.2.2 Travelling-Wave Arrays

Waveguide-fed slot arrays are categorized based on their excitation as either resonant or travelling-wave. Resonant arrays are excited by a standing wave, with radiating elements spaced  $\lambda_g/2$  apart and a short circuit termination. Successive elements are alternated in rotation or displacement with respect to the centre of the waveguide. These arrays produce broadside radiation, but are inherently narrow band. Moreover, they do not allow for frequency scanning and will not be detailed here. Waveguide-fed slot arrays can also be excited by travelling-waves. Alternately oriented slots are spaced slightly more or less than  $\lambda_g/2$ , resulting in few degrees of beam tilt. A matched termination is placed at the end of the waveguide to prevent reflected waves from generating a second beam in the opposite direction, referred to as a conjugate beam. The resulting arrays generally exhibit larger bandwidth and allow for frequency scanning [36].

The equivalent transmission line network for a linear array of  $N$  transverse slots is depicted in Figure 3.6. The waveguide is characterized by its propagation constant for the TE<sub>10</sub> mode,  $\beta_{10}$ . Slots are assumed resonant, such that their active impedance is purely resistive, and are uniformly separated by  $d$ , as is typically the case in practical arrays [34]. The following recursive equations from transmission line theory then apply

$$z_n = r_n + \frac{z_{n-1} + j \tan(\beta_{10}d)}{1 + j z_{n-1} \tan(\beta_{10}d)}, \quad (3.8)$$

$$I_n = I_{n-1} [\cos(\beta_{10}d) + j z_{n-1} \sin(\beta_{10}d)], \quad (3.9)$$

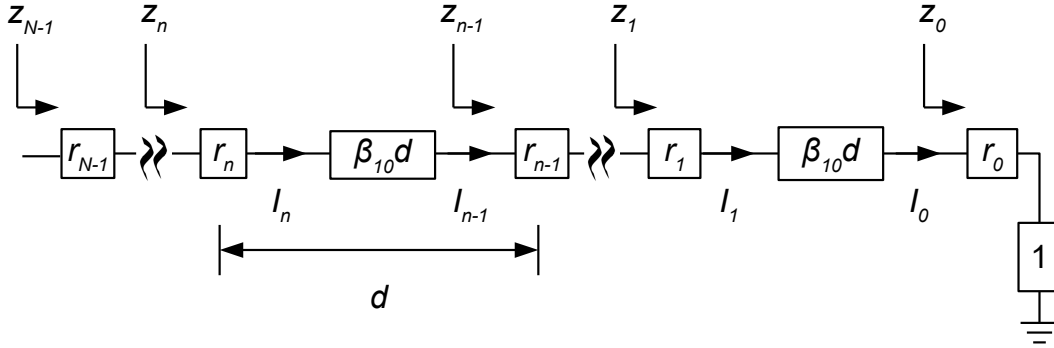


Figure 3.6: Traveling-Wave Array Transmission Line Model.

where  $z_n$  is the normalized input impedance looking into  $n$ -th slot and  $I_n$  is the current exciting it.

The power radiated by an individual slot is  $|I_n|^2 r_n$ . It follows from Section 2.3 that the power radiated from a single element in a synthesized array will be proportional to the square of its excitation magnitude. Thus

$$|I_n|^2 r_n = BA_n^2 \quad (3.10)$$

for some constant  $B$ . If the total radiated power is  $P_{\text{rad}}$  then

$$P_{\text{rad}} = B \sum_{n=0}^{N-1} A_n^2. \quad (3.11)$$

A portion of incident power at each node is coupled to a slot. Thus, for practical amplitude distributions, slots must progressively couple more power as distance from the array input is increased. If all incident power is to be radiated, this coupling becomes impractically large for slots near the termination. It is therefore common for designs to include a small amount of power delivered to the termination [36]. If this power is denoted  $P_l$ , the radiated power is ideally the difference between the incident power and  $P_l$ . This allows the constant in (3.11) to be determined. Assuming a normalized incident power of unity magnitude, it is obtained from

$$B = \frac{1 - P_l}{\sum_{n=0}^{N-1} A_n^2}. \quad (3.12)$$

Equations (3.8) to (3.12) represent a set of linear equations that can be solved for the required active slot impedances for a specified set of slot excitations,  $A_n$ , spacing,  $d$ , and normalized input impedance,  $z_{N-1}$ . The normalized input impedance is ideally  $1 + 0j$ , presenting a matched impedance to the source.

Once the required slot impedances are known, the geometry of each slot is obtained from the results of the process described in Section 3.2.1. This completes the design of the array.

Here, the transmission line model was used to represent a linear array of slots cut in a straight length of rectangular waveguide. It can be seen that successive slots will be excited with a uniform phase shift,  $\alpha = \beta_{10}d$ . From previous discussions in Sections 2.1.3 and 2.2, the direction of the main beam will vary with frequency. A detailed discussion of this effect follows later in this section.

The transmission line model also illustrates one of the limitations of arrays excited by travelling-waves when compared to resonant excitations. That is, the inability to radiate at broadside. Broadside radiation occurs when all slots are excited in phase. Under these conditions, the equivalent transmission line is resonant, and the sum of the slot impedances and matched load presents a large series impedance or open circuit to the input. This corresponds to the reflected fields internal to the waveguide adding in phase. The result is that power cannot enter the structure, and the array does not radiate. This in-phase addition is exploited in the design of resonant arrays of series slots to allow for radiation at broadside. Replacing the matched load with a short circuit allows the slots to be designed such that the sum of their normalized impedances is unity, presenting a matched input impedance to a source. The requirement of a standing wave excitation, however, dictates that they are inherently narrow band. To benefit from the broader bandwidths characteristic of travelling-wave arrays while permitting radiation at broadside, reflection cancelling methods have been developed to suppress the reflections from individual slots when excited in phase.

### 3.2.3 Reflection Cancelling Arrays

In applications where broadside radiation is required, and bandwidth or frequency scanning specifications prevent the use of a resonant array design, reflection cancelling techniques must be adopted. These techniques introduce an additional discontinuity in the waveguide that produces a reflected wave that adds destructively with, or cancels, the reflections from the original slot. Originally proposed as pairs of slots [23], alternative non-radiating discontinuities can also be used. The resulting reflection-less array element allows for a simplification in the design of travelling-wave arrays which will be detailed here.

The principle behind reflection cancelling arrays is that two waves equal in magnitude but differing in phase by  $\pi$  will sum to zero. If an element produces an equal reflected wave to that of the slot, it can be placed  $\lambda_g/4$  away and the reflected waves will cancel as the two-way electrical length is  $\pi$ . The most intuitive discontinuity is a similar slot as mentioned above and depicted in Figure 3.7(a).

Disadvantages in the application of reflection cancelling slots led to the development of non-radiating

reflection cancelling elements [23–26], some possibilities of which are depicted in Figures 3.7(b) and (c). The element pattern of a slot-pair is directed slightly off-broadside. When implemented in arrays, this can produce large side lobes or grating lobes. Furthermore, mutual coupling between the slots complicates the design. When a non-radiating discontinuity is used to suppress reflections, the effect on the radiation pattern is minimal and the reduction of mutual coupling simplifies the modelling of the combination slot and element.

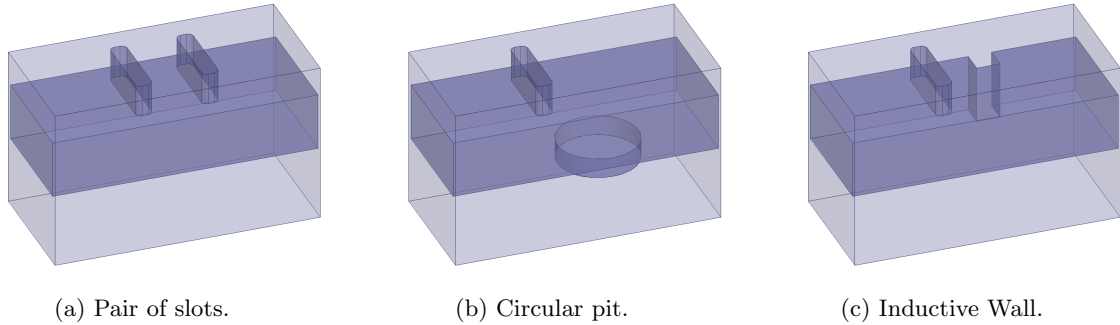


Figure 3.7: Refection Cancelling Array Elements.

The design process for reflection cancelling arrays was developed with the use of computer-based modelling. It is similar to that of the travelling-wave array, however it is based on scattering parameters. The radiating slot and its reflection cancelling element are first modelled as a two port network using the techniques described in Section 3.2.1. A parametric study or alternative optimization technique is then used to reduce the reflection coefficient seen at the input by varying the physical parameters and placement of the reflection cancelling element. The two port scattering matrix and radiation characteristics are then extracted from the model’s solution.

The coupling,  $C$ , of the combined element is then defined as the ratio of radiated power to the input power

$$C = \frac{P_{\text{rad}}}{P_{\text{in}}} = 1 - |S_{11}|^2 - |S_{21}|^2, \quad (3.13)$$

where the right-most expression is valid for a lossless structure. The phase of the radiated field is denoted  $\alpha_{\text{rad}}$ . The above process is then repeated for additional slot geometries to obtain  $C$  and  $\alpha_{\text{rad}}$  as a function of the slot and reflection cancelling element physical parameters.

To implement a synthesized array factor, the required coupling value for each element must be determined from the calculated excitation amplitudes. For an array of  $M$  elements numbered from

$n = 0$  at the input to  $n = M - 1$  at the termination, the required couplings are determined from

$$C_n = \frac{A_n^2}{\sum_{m=n}^{M-1} A_m^2} \quad (3.14)$$

This expression is analogous to Equations (3.10) to (3.12) for the travelling-wave array with no power delivered to the termination.

In contrast to the design of travelling-wave arrays, the elements of a reflection cancelling array are not assumed to be resonant. Consequently, the excitation phase of the slots will vary with their magnitude. If an array factor's amplitude distribution is implemented, the element spacing must be adjusted to correct this phase variation and produce radiation in a specified direction. For broadside radiation, the following expression determines the required element spacing,  $d_n$ ,

$$\beta_{10} d_n = \alpha_{rad,n} + \angle S_{21,n-1} - \alpha_{rad,n-1} \quad (3.15)$$

Equations (3.13) to (3.15) demonstrate the simplicity of implementing reflection cancelling arrays once coupling and phase values have been determined for a set of elements. These arrays however, suffer from their use of non-uniform spacing. This has a tendency to reduce the bandwidth as the beam will deteriorate or grating lobes may result if the frequency varies too much from the design.

### 3.3 Frequency Scanning Waveguide-fed Slot Arrays

From previous discussions, it has been established that a waveguide-fed slot array excited by a travelling wave will produce a beam that steers with frequency. To enable beam steering to appreciable angles, the waveguide must be meandered as illustrated in Figure 3.8 to achieve a sufficiently large frequency-dependent phase shift. The result is an array that can be designed to scan over a specified angular range for a given bandwidth.

An expression describing the scanning characteristic of a uniformly excited meandered waveguide can be obtained from the approach outlined in Section 2.2. When the waveguide's propagation constant, or guided wavelength, is included, Equation (2.22) becomes

$$\sin \theta_m = \frac{l}{d} \lambda_0 \left( \frac{1}{\lambda_{g,c}} - \frac{1}{\lambda_g} \right) \quad (3.16)$$

where  $\lambda_g$  is the guided wavelength of the  $TE_{10}$  mode given in Equation (3.2), and  $\lambda_{g,c}$  is the guided

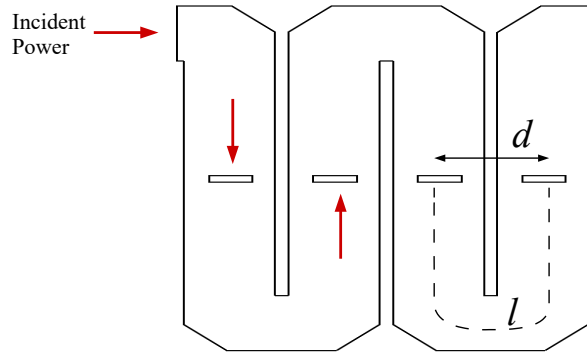


Figure 3.8: Frequency Scanned Waveguide-fed Slot Array. Direction of excitation wave indicated in red.

wavelength at the broadside frequency. It can be observed in Figure 3.8 that successive slots are excited by the same wave travelling in opposite directions. For the slots to radiate in phase, an extra half guided wavelength at broadside must be added to the serpentine length when compared to the derivation in Section 2.2. Thus, (3.16) is valid for  $l = (m + 0.5)\lambda_{g.c}$ , where  $m$  is an integer.

The alternation in incident excitation orientation also affects the radiation patterns of frequency scanned waveguide antennas. The resulting array factor for a uniform linear array implementation is given as

$$AF(\psi) = \sum_{n=0}^{M-1} (-1)^n e^{jn\psi}, \quad (3.17)$$

where

$$\psi = k_o d \sin \theta - \beta_{10} l \quad (3.18)$$

and the  $(-1)^n$  term accounts for the alternation. Practically, this results in grating lobes being generated for spacings smaller than that predicted by Equation (2.11).

As the excitation phase of successive slots is determined by the length of serpentine transmission line, physical element spacing can be maintained constant for any specified phase distribution. It follows that if the design process for reflection cancelling arrays is followed, Equation (3.15) can be satisfied by substituting  $l_n$  for  $d_n$ . In this case the serpentine length is no longer constant. Noting that the resulting electrical length,  $\beta_{10} l_n$ , is periodic in  $2\pi$ , each  $l_n$  should be selected as close as possible to the value of  $l$  that produces the desired scanning characteristic given in Equation (3.16).

It should be noted however, that (3.16) is for the ideal scenario and (3.15) corresponds to a single frequency. In practice however, the elements of an array will also exhibit a frequency dependent phase shift. This tends to introduce a phase error in non-uniformly excited arrays that manifests in the radiation pattern as higher side lobe levels or shoulders in the main beam.

### 3.4 Fabrication of Waveguides

There are a number of fabrication technologies available for the manufacturing of slotted waveguide arrays. Computer numerical controlled (CNC) milling is most commonly used in microwave designs [36]. The smaller wavelengths of MMW designs however, has led to the use of manufacturing technologies with more strict tolerances such as diffusion bonding [37] and micromachining [38]. Inaccuracies in the manufacturing process will cause the performance of the antenna to suffer; however, employing more advanced fabrication technologies results in significantly increased costs. The selection of an appropriate technology must consider this compromise between performance and cost.

Antenna designs for operation in the same Ka-band as this work have been successfully implemented with economical CNC processes [12, 27]. In these processes, a milling machine removes material from a block of conducting metal using a circular cutting tool. This generally produces two or more pieces that must be joined to form a waveguide. The above referenced works simply used screws or clamps to join their components, while [39] has found that laser welding or brazing is preferred at lower MMW frequencies.

From Figure 3.2, it can be inferred that the location of the joint will impact the performance of an array. The joint effectively reduces the conductivity of the waveguide, resulting in increased losses proportional to the ideal surface currents where the components meet. This impact is compounded if the joint contains air gaps, as the interruption of surface currents can excite fields within them. These fields generate additional surface currents inside the gaps, and conduction losses are further increased. The waveguide's surface current is minimum along the center of the top and bottom walls, thus a small discontinuity along this line will have a negligible impact on the waveguide's operation. In many slotted waveguide applications, the waveguide is fabricated as a channel in a solid block, with slots cut in a thin cover that is bolted to the channel. The resulting structure is simple, and thus economical, to implement, though efficiency is sacrificed.

## Chapter 4

# Frequency Modulated Radar

Radar systems detect and locate reflecting objects using electromagnetic radiation. A signal is radiated in an observed direction and a received echo indicates the presence of a target. The distance to the object can be determined from the time delay between the transmitted and received signals. Pulsed radars use finite duration signals and measure the delay directly. Frequency Modulated Continuous Wave (FMCW) radars continuously transmit a signal with a frequency that varies with time. The difference in frequency between the received and transmitting signals indicates the time delay and thus range to the reflecting object.

The FMCW technique has been demonstrated to be compatible with frequency scanning [40] and MMW frequencies [41]. These radars have a number of characteristics that make them well suited for a demonstration of the designed antenna's application [10]. Continuously transmitting a signal increases the total energy intercepted by a target, reducing the required peak power of the transmitter. Additionally, the time delay between transmit and receive can be on the order of micro- or nanoseconds. To measure this delay directly requires a large receiver bandwidth. The bandwidth requirement to determine an FMCW difference frequency is generally much smaller. Reducing receiver bandwidth and peak transmitting power greatly simplifies the design of a radar front-end. This is particularly advantageous for MMW applications, as components are costly and introduce significant losses.

The FMCW technique and its basic principle of operation in determining target range will be detailed here. One example implementation of a frequency-scanning radar will be presented and practical effects that impact the detection of targets will be discussed. Reference [10] should be referred to for additional details and derivations relevant to the concepts presented here.

## 4.1 Principle of Operation

The basic principle of a frequency modulated radar is illustrated in Figure 4.1. A transmitting signal with linearly increasing frequency,  $f_t$ , is radiated in the direction of a target. The signal is scattered by the target, and a time-delayed copy of the transmitted signal, or echo, is received where the delay,  $T_p$ , is proportional to the target's range. The received echo is mixed with the transmitted signal to generate a beat signal of frequency,  $f_d$ , that is proportional to the time delay.

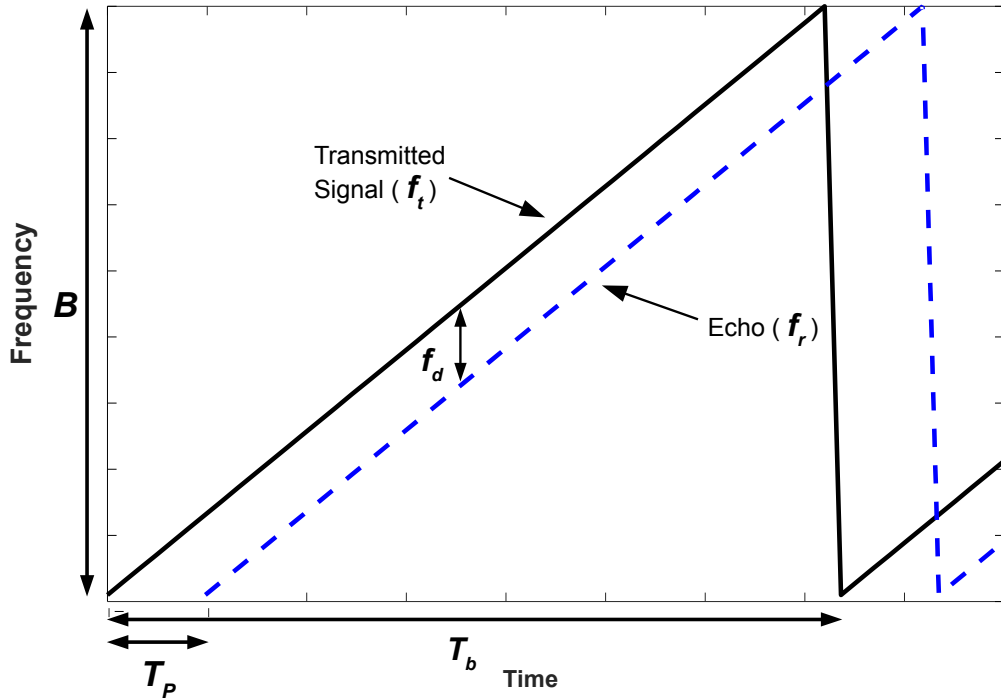


Figure 4.1: FMCW Principle.

If the transmitted frequency,  $f_t$ , is increased by a bandwidth,  $B$ , over a period,  $T_b$ , the beat frequency is found to be

$$f_d = \frac{B}{T_b} T_p \quad (4.1)$$

The time delay is simply the round-trip time for the signal to travel the distance  $R$  and back. Thus

$$T_p = \frac{2R}{c} \quad (4.2)$$

The range of the target is therefore proportional to the measured beat frequency. It is given by

$$R = \frac{cT_b}{2B} f_d \quad (4.3)$$

### 4.1.1 Range Resolution

The range resolution,  $\Delta R$ , of a radar is the smallest distance that two equal targets can be distinguished in range. From Equation (4.3) it follows that it will be determined by the frequency resolution of the radar system. The frequency resolution,  $\delta f$ , is generally defined as the half-power bandwidth of a single frequency signal of length  $T_b$ , where  $\delta f \approx 1/T_b$ . The resulting expression for the range resolution is

$$\Delta R = \frac{c}{2B} \quad (4.4)$$

This simple relation demonstrates the importance of the radar's bandwidth. It is inversely proportional to the range resolution of a system, thus large bandwidths are desirable for precise range measurements.

## 4.2 Frequency Scanning Implementation

A simplified block diagram of a frequency-scanned FMCW radar is depicted in Figure 4.2. The principle described above is used to determine the range of the target, assuming the transmitting and receiving antennas are co-located or can be approximated as such. This antenna configuration is referred to as a quasi-monostatic radar and is generally used in MMW FMCW applications [41]. This provides increased isolation between the transmitter and receiver when compared to a single antenna configuration, and is beneficial for reasons that will be described in the next section. The use of a frequency-scanning antenna allows the target's angular position to be determined based on the transmitted signal's frequency.

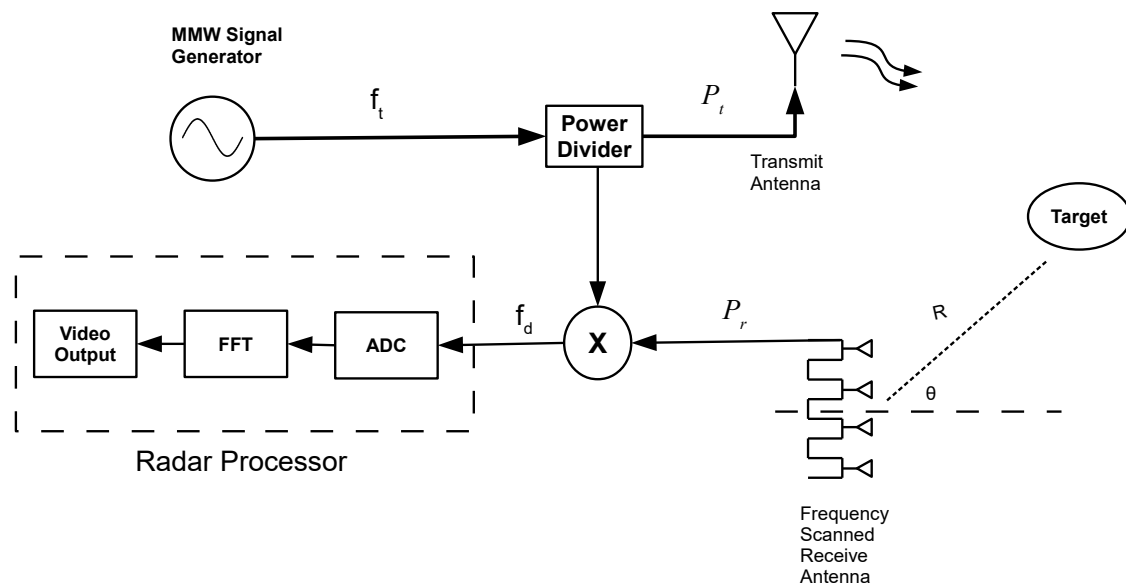


Figure 4.2: Frequency Scanned FMCW Radar Block Diagram.

The elements featured in Figure 4.2 act as a radar front-end, to produce and radiate the required FMCW signal, and measure the difference frequency from a received echo. The MMW signal generator acts as the transmitter, generating the linearly modulated signal with frequency  $f_t$ . A power divider directs an equal amount of the generated signal to the transmitting antenna and mixer. The wide beam width transmitting antenna radiates energy in the general observation direction. The transmitted signal is scattered by a target and received by a frequency scanning antenna. A mixer multiplies the received echo with a portion of the transmitted signal to produce the beat frequency. The radar processor samples the beat signal in time and determines its frequency domain representation to be presented on a radar display.

In order to determine a target's location in both angle and range, the radar's total bandwidth is subdivided into smaller bandwidths,  $\Delta B_n$ . Each  $\Delta B_n$  is centred at a frequency that corresponds to a fixed observation angle,  $\theta_n$ , according to the frequency scanning characteristic of the receive antenna. The radar transmits a signal with the frequency-time characteristic previously shown in 4.1, where the sub-bandwidth,  $\Delta B_n$ , is used in place of  $B$ . The use of a frequency-scanned receiving antenna results in an echo being measured only if it contains frequencies for which the antenna's beam is directed toward the target. Thus, if an echo is observed, the transmitted centre frequency will indicate a target's angular position. The measured beat frequency can be used to determine the target's range from Equation (2.18), with  $\Delta B_n$  substituted for  $B$ .

This method represents a discretization of the frequency scanning characteristic of the receive antenna. The radar's observation direction is steered by setting the transmitted centre frequency to discrete values that correspond to fixed angles. The beam is scanned sequentially, with the radar continuously performing range measurements at one angle until the transmitted frequency is set for the next. If data storage and appropriate processing is available, a measured beat signal for each transmitting frequency can be stored and a two-dimensional polar radar image produced by combining the stored signals.

### 4.3 Practical Considerations

There are a number of practical considerations in the implementation of an FMCW radar that affect the accurate determination of a target's location. The use of frequency scanning introduces additional factors that can impact the design of a system.

### 4.3.1 Range and Angular Resolutions

From Equation (4.4), it is clear that the reduction in effective bandwidth required for frequency scanning will have a detrimental effect on the range resolution. Additionally, the discretization of the antenna's continuous beam scanning characteristic reduces the angular resolution. It follows that in this frequency scanned FMCW implementation there is an inherent trade-off between angular and range resolutions. In general, the discrete steering angles are determined by the beamwidth of the frequency scanned antenna and the bandwidths determined accordingly. This is a design consideration however, and can be modified depending on the application.

### 4.3.2 Radar Equation

The radar equation relates the performance of a radar to the characteristics of its components, environment, and target. It is used to express key performance metrics of a system and the factors that influence them. Here, it is presented as an expression to determine the received power,  $P_r$ , for a specific radar configuration and target. It is given by

$$P_r = \frac{P_t G_t G_r \sigma \lambda_o^2}{(4\pi)^3 R^4} \quad (4.5)$$

where  $P_t$  is the transmitted signal's power,  $G_t, G_r$ , represent the gain of the transmitting and receiving antennas, and  $\sigma$  is the radar cross section of a target at a range  $R$ , from the radar. If system losses are to be accounted for, a factor,  $L$ , can be included in (4.5) to reduce the calculated received power proportionally.

### 4.3.3 Radar Cross Section

The radar cross section represents the strength of an echo a target will produce. It is a measure of the reflectivity of an object and can be defined as the area of an isotropic radiator that would produce the same echo strength as the object. Assumed in this definition is that for both the isotropic radiator and object, the incident power is the same and the echo strength is measured at the receiver. Formally, it can be expressed as

$$\sigma = \frac{\text{power reflected toward source/unit solid angle}}{\text{incident power density}/4\pi} = 4\pi R^2 \frac{P_s}{P_i} \quad (4.6)$$

where  $P_s$  is the scattered power from the target and  $P_i$  is the power incident. In Equation (4.6), the RCS is expressed in square metres; however, it is also often expressed in decibels relative to one square

metre.

A table of typical radar cross section values for common objects is found in [10]. Of interest to the highway monitoring application described in Chapter 1, is the radar cross sections of cars, persons, and large animals such as deer or moose. The values for persons and cars are given as 0 and 10 dBm<sup>2</sup> respectively. An explicit value for large animals was not found in any literature; however, it is not expected to differ greatly from that of a person. Thus, where relevant in this work its value will be assumed 0 dBm<sup>2</sup>.

In general, the radar cross section of an object is a function of both observation angle and frequency. Thus, the single valued cross sections given above should be thought of as example or averaged values. In later chapters of this work, their values will be used solely for illustrative purposes, therefore their accuracy is not critical.

#### 4.3.4 Signal to Noise Ratio

As presented, the radar equation is insufficient to predict a radar's ability to determine the presence of a target. In practice, received radar signals are corrupted by the presence of noise. The random nature of the noise can act to increase or reduce the measured received signal regardless of a target echo. Radars commonly use threshold detection, where the presence of a target is established if the measured signal exceeds a set value. Thus, if the noise power is larger than the threshold in the absence of a target, a false detection occurs. Similarly, if the noise reduces the magnitude of an echo from a target below the threshold, a missed detection occurs. Clearly, both of these scenarios are undesirable.

As a received echo must compete with the noise in a radar system, the signal to noise ratio is a more appropriate figure of merit for the successful detection of a target. It can be expressed

$$\frac{S}{N} = \frac{P_r}{N} = \frac{P_t G_t G_r \sigma \lambda_o^2}{(4\pi)^3 R^4 N} \quad (4.7)$$

where  $N$  is the available noise power. A large signal to noise ratio allows a suitable threshold to be established that reduces both the probability of false and missed detections.

#### 4.3.5 Receiver Noise and Noise Figure

The dominant contribution to the noise measured by a radar is typically generated internal to the receiver. In the absence of other sources, a thermal noise is generated in the receiver. This noise arises due to thermal agitation of charge carriers in conducting portions of the receiver. The thermal noise power,  $N_o$ , is proportional to the system temperature,  $T$  and the receiver's noise bandwidth  $B_n$ . It's

value in watts is calculated as

$$N_o = k T B_n \quad (4.8)$$

where  $k$  is Boltzmann's constant with  $k = 1.38 \times 10^{-23}$  J/deg. In radar applications, the noise bandwidth is approximated by the video bandwidth of the radar processor, i.e. the components left of the mixer in Figure 4.2. The consequence of this thermal noise, is that even in the most ideal case the signal to noise ratio will be finite and inversely proportional to the radar's video bandwidth.

Additional sources of noise in the components of a radar receiver are characterized by their noise figure. The noise figure may be defined as the ratio describing the degradation in signal to noise ratio as the signal propagates through the component. It is expressed in decibels and is given by

$$F = 10 \log \left( \frac{S_{in}/N_{in}}{S_{out}/N_{out}} \right) \quad (4.9)$$

where  $F$  is the noise figure,  $S_{in}$ ,  $S_{out}$  are the input and output signal powers and  $N_{in}$ ,  $N_{out}$  are the noise powers.

In the case of systems of  $N$  cascade connected components, the resulting noise figure is

$$F_{sys} = F_1 + \frac{F_2 - 1}{G_1} + \frac{F_3 - 1}{G_1 G_2} + \frac{F_4 - 1}{G_1 G_2 G_3} + \cdots + \frac{F_N - 1}{\prod_{n=0}^{N-1} G_n} \quad (4.10)$$

where  $G_n$  and  $F_n$  are the gain and noises figure of the  $n$ -th device, with  $n$  numbered from 1 at the input of the receiver. This expression highlights the importance of an input stage with a low noise and high gain. For this reason, many radars include a low noise amplifier in the receiver, inserted between the receiving antenna and mixer in Figure 4.2.

### 4.3.6 Transmitter Phase Noise and Leakage

An ideal signal source would produce a pure, single-frequency sinusoidal output corresponding to an impulse function in the frequency domain. Practical sources however, exhibit random, short term fluctuations in phase. Referred to as jitter in the time-domain, it can be observed as random deviations of the position of the signal. In the frequency domain it is referred to as phase noise and manifests as a broadening of the ideal impulse. This effect can result in received signals from large targets masking nearby smaller targets, and when combined with transmitter leakage, impose a minimum observation range over which the radar can observe.

As an FMCW radar simultaneously transmits and receives, there is a potential for the transmitted

signal to be measured directly by the receiver. This effect is referred to as leakage and in a practical radar system, there are a number of paths through which this can occur. In the system presented in Figure 4.2, this can arise due to reflections from the transmitting antenna and limited isolation in the power divider and mixer. In addition, while the quasi-monostatic configuration presented in this chapter provides an isolation that is typically greater than that of a circulator in a single antenna system, there is still a possibility of a leakage through space. In this case, the signal propagates directly from the transmitting antenna to the receiving antenna.

The leaked transmitted signal accumulates a slight delay proportional to the leakage path length. As it appears at the receiver's input, it is mixed with the reference transmitting signal, effectively appearing as a target at approximately the same location as the radar. Limited isolation and relatively high transmitting powers result in a large amplitude leakage signal appearing at DC. This large amplitude can saturate or damage receiver components reducing the radar's sensitivity. Furthermore, the broadening effect of the signal generator's phase noise leads to the leakage signal occurring for a larger spectrum of frequencies. Its large magnitude tends to over power the received echoes of small targets near the radar, reducing the radar's effectiveness at short ranges.

#### 4.3.7 Clutter

When placed in a practical environment, a radar will receive signals reflected from its surrounding environment in addition to those from its intended target. These signals are referred to as clutter. Whether a received signal is classified as clutter is application specific; in many cases, example sources of clutter include the ground, weather, and buildings. Clutter can be considered a location dependent noise power, effectively reducing the signal to noise ratio in specific directions. This can increase the difficulty in detecting targets using simple thresholding, thus methods to reduce their impact are used.

In applications where the clutter is generally stationary relative to the radar, one method to reduce clutter effects is to record only the changes in successive radar measurements. As a result, only moving targets will be detected. Radars using this technique are referred to as Moving Target Indicator (MTI) radars and are commonly used in surveillance applications.

An alternative technique to reduce clutter effects is the use of a clutter map. The received radar signals from the environment can be stored and used to establish location dependant thresholds. Thus, the radar will detect targets that produce echoes with magnitudes greater than the surrounding clutter. Targets producing smaller echoes will result in missed detections. Regardless of the technique used, the presence of noise reduces the radar's effectiveness in detecting objects with small radar cross sections.

## Chapter 5

# Antenna Design and Simulation

Chapters 2 and 3 introduced relevant array theory and design considerations for waveguide-fed slot arrays. In addition, expressions governing the behaviour of the various performance characteristics of a frequency scanning array were derived. In this chapter, an array will be designed incorporating these concepts to meet the specifications for the envisioned radar described in Chapter 1. Practical considerations regarding the fabrication of the antenna will also be included.

An overview of the design will first be introduced, discussing initial design considerations regarding the antenna's geometry and fabrication. A uniform serpentine waveguide is then designed with reduced reflections for an approximate scanning characteristic. Next, a set of reflection cancelling elements is generated and characterized in a uniform array to determine their coupling and required phasing. Finally, an approximate Taylor-Villeneuve array is implemented from the set of reflection cancelling elements. Calculations and relevant electromagnetic simulations will be used to illustrate steps of this process.

The designed antenna's predicted performance will be analyzed through full-wave analysis using Ansys HFSS. Simulation results of the antenna's full structure will demonstrate the produced radiation pattern satisfies the required specifications. Finally, the effect of the antenna's scanning characteristic in a radar system will be determined from the radiation patterns.

### 5.1 Design Overview and Initial Considerations

The basic geometry of the designed antenna is presented in Figure 5.1. Transverse slots cut in the broad-wall of a meandered WR22 rectangular waveguide radiate a beam that scans from its maximum angle through broadside as its excitation frequency increases. The array's one-dimensional geometry produces a fan beam, characterized by a narrow beamwidth in the azimuthal scanning plane and an approximately

uniform pattern in the perpendicular elevation plane. Circular pits embedded in the bottom broad wall suppress the reflections generated from each slot when the array is excited in phase. The resulting structure is compatible with CNC milling, allowing it to be fabricated quickly and economically.

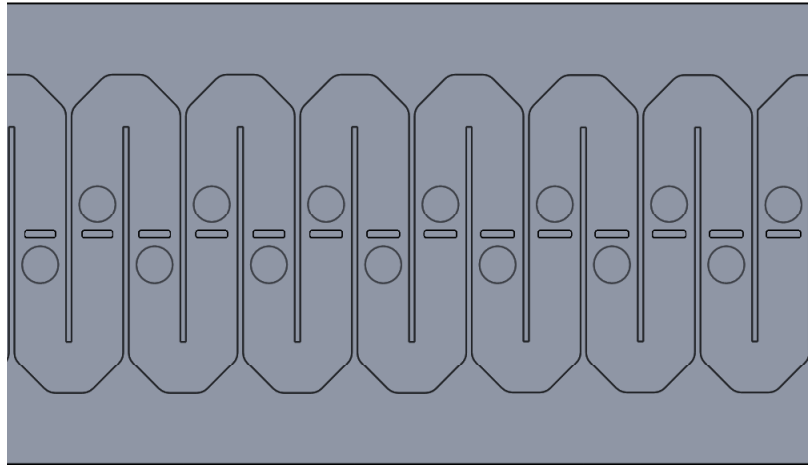


Figure 5.1: Antenna Design Concept.

Of the slot configurations presented in Section 3.1, transverse broad wall slots were selected based on their simplicity and vertical polarization. This slot configuration is avoided in many array applications as its excitation magnitude and phase are both determined solely by its length. This is in contrast to the alternative slots shown in Figures 3.3 and 3.4 of Chapter 3 which provide control over both magnitude and phase independently through an additional degree of freedom in geometry. Thus, if the lengths of a set of transverse slots lengths are adjusted for a specific amplitude distribution, the resonant active impedance requirement for a uniformly spaced travelling wave design cannot be satisfied. In the design of reflection cancelling arrays, this simplifies the determination of the coupling and phase terms as only a single physical parameter is varied. Finally, it can be easily fabricated by milling the slot out of a thin sheet of aluminum.

The operating frequency of the antenna dictates the possible cross-sectional areas that support a single  $\text{TE}_{10}$  excitation. Only standard rectangular waveguide cross-sections were considered in this design to simplify integration with a radar front end. The Ka-Band frequency range proposed here falls within the operating frequencies of both WR22 and WR28 waveguides. The smaller WR22 dimensions of  $a = 5.69$  mm and  $b = 2.84$  mm were selected as the broad wall width allows sufficiently small spacing for grating-lobe free operation over the design's entire scan range.

Circular pits were selected to suppress the reflections from the slots. Of the available discontinuities depicted in Section 3.2.3 they are most compatible with CNC milling due to the rounded nature of

their geometry, resulting in increased fabrication accuracy. Additionally, they can be designed with a fixed radius, varying only their depth to cancel reflections from arbitrary slot excitations. This further simplifies the determination of coupling and phase terms for the reflection cancelling design.

The antenna was designed with consultation from the University of Toronto's MC-78 Machine Shop. To minimize costs, it was suggested to use CNC milling to carve the waveguide interior in a block of aluminum and cut slots in a thin cover. The two pieces could then be joined using screws. For sufficient mechanical mating, a minimum cover thickness of one sixteenth of an inch was recommended, establishing the height of the radiating slots.

Characteristics of the recommended CNC machining process were accounted for in the design. The standard tolerance available for this work was quoted as three mil or approximately 0.076 mm. A slightly larger minimum feature resolution of 0.1 mm was adopted to reduce performance errors introduced by this tolerance. Minimum radii were imposed to account for the size of the cutting tools used. These were 1.65 mm for features internal to the waveguide, and 0.25 mm for the corners of the slots. Finally, a width of 0.8 mm was recommended for the slots. These values are incorporated in any full-wave simulation included in this section.

## 5.2 Serpentine Waveguide Design

The serpentine-waveguide is the feeding structure that the array is built upon, and its behaviour dictates the environment in which the array elements operate in. The geometry of the waveguide provides the majority contribution to the progressive phase shift between slots, thus has the most impact on the frequency scanning characteristic of the array. It is therefore an appropriate starting point for the detailed design of the array.

A single unit cell of the WR22 waveguide is illustrated in Figure 5.2 with design parameters indicated. As an initial value, the serpentine length was approximately set such that,  $l = 2.5\lambda_{g,c} = 32.5$  mm, with  $\lambda_{g,c}$  corresponding to broadside radiation at 35 GHz. The modified frequency-scanned array factor, (3.17), was used to obtain an approximate maximum slot separation. For scanning to  $-22^\circ$ , the resulting separation was  $d = 6.2$  mm. Equation (3.16) predicts this geometry will result in the array scanning from  $-23.3^\circ$  to  $+2.4^\circ$  over the operating frequency. It is expected that these dimensions will change due to the inclusion of the array elements; however, a close approximation to the final design allows the element design to incorporate the effects of the waveguide. It may be noted that the predicted angular scan range is slightly greater than the design specification. This was by intent, to allow for some manufacturing tolerance errors while ensuring the specified range was achieved.

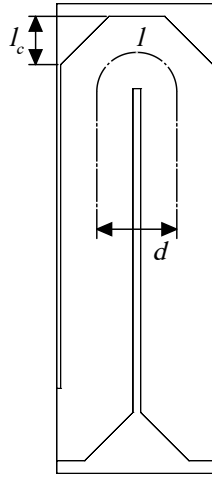
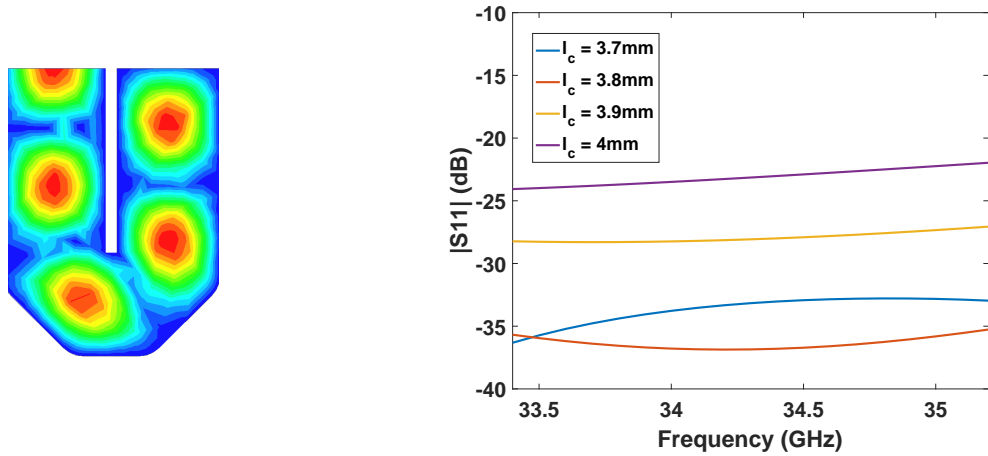


Figure 5.2: Waveguide Unit Cell.

The waveguide bends are distributed periodically along the length of the waveguide. Similar to the in-phase excitation of slots, reflections from the bends can add coherently to produce a large reflection at the input to the array. These reflections must therefore be sufficiently reduced. In rectangular waveguides, this may be achieved through angling, or chamfering, the 90° bends. Here, a pair of 90° bends were simulated over the operating frequency for varying set-back distances,  $l_c$ . The bends were spaced as they would appear in an array with  $d = 6.2$  mm. The simulation results in Figure 5.3 show that reflections at 35 GHz were lowest for  $l_c = 3.8$  mm.

(a) Simulated Waveguide Bend.  
Magnitude of electric field indicated.

(b) Reflection coefficient magnitude

Figure 5.3: Waveguide Bend Simulation Results.

To finalize the initial geometry of the waveguide, a lossless section of ten unit cells was simulated to

determine the reflection coefficient. As expected, a maximum occurred near 35 GHz. It was observed that increasing the separation,  $d$ , reduced this magnitude. The separation was therefore nominally increased to  $d = 6.3\text{mm}$ , resulting in a reduction of 5.6 dB in the maximum reflection. These observations are shown in the reflection coefficients plotted in Figure 5.4.

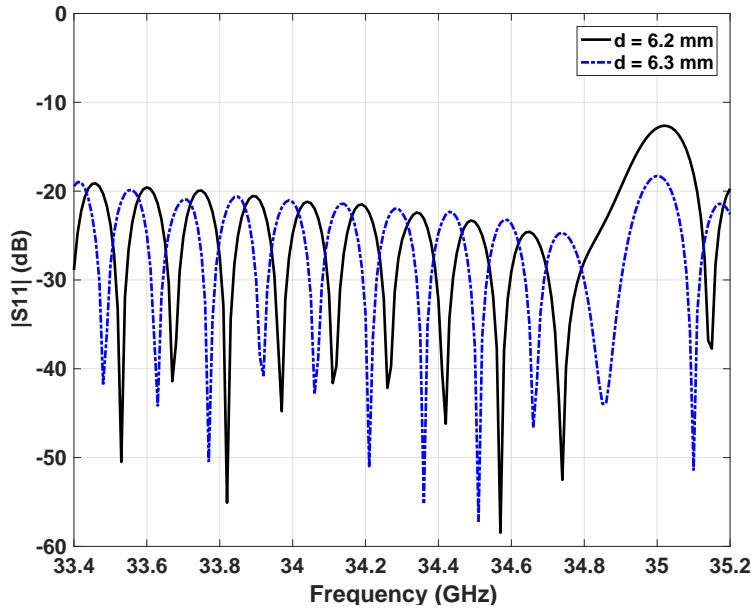


Figure 5.4: Reflection Coefficient of 10 Serpentine Waveguide Unit Cells.

Table 5.1 summarizes the resulting waveguide dimensions of this stage. The algebraic array factor corresponding to this structure is plotted in Figure 5.5 for the extreme and center operating frequencies. The onset of a grating lobe at  $\theta = 90^\circ$  can be seen for the extreme steering angle and is an expected result of increasing the slot separation. Its effect on the total radiation pattern of the antenna will be limited however, as the orientation of the slots imposes a null in the element factor for  $\theta = \pm 90^\circ$

Table 5.1: Initial Serpentine Waveguide Dimensions.

Dimension	Symbol	Value
Broad Wall Width	$a$	5.69 mm
Narrow Wall Height	$b$	2.85 mm
Serpentine Length	$l$	32.5 mm
Slot Separation	$d$	6.3 mm
Symmetric Chamfer	$l_c$	3.8 mm

### 5.3 Slot-Pit Pair Design

In order to implement a synthesized radiation pattern satisfying the specifications of this work, the excitation magnitude and phase of each slot must be controlled. Furthermore, broadside radiation

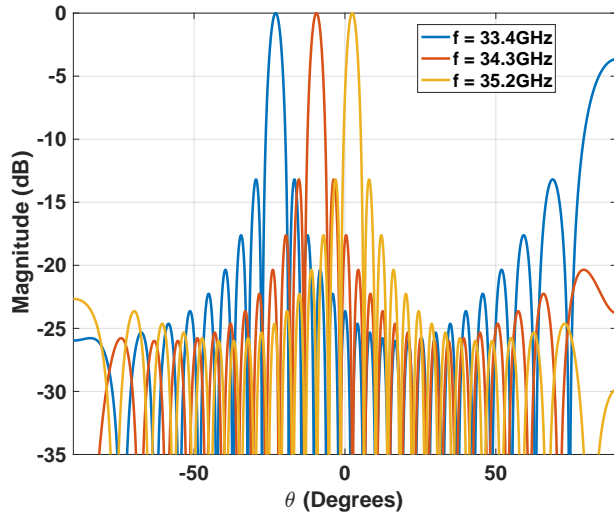


Figure 5.5: Algebraic Uniform Array Factor for 10 Unit Cells.

requires the reflection of each slot be suppressed. For the transverse slot used in this design, the excitation magnitude may be controlled through varying its length. The magnitude of the reflected wave will vary proportionally to the excitation and the pits' dimensions must be adjusted accordingly. Finally, the excitation phase is determined through the combined interactions of the slots, pits, and serpentine waveguide. The design of the array elements must account for all of these effects.

The design process followed here was to first generate a set of slot-pit pairs for varying slot lengths with reduced reflections at 35 GHz. Simulating a single pair of elements permitted an efficient parametric analysis to determine suitable configurations for reduced reflections. Uniform arrays of each pair in the serpentine waveguide were then modelled. The uniform array model allowed the serpentine length to be adjusted for the required slot phasing and provided an accurate estimation of the slot coupling. The resulting coupling values permitted the approximate implementation of a synthesized array factor.

### 5.3.1 Reflection Cancelling

The combined slot-pit pair was characterized using the approach described in Section 3.2.1 of Chapter 3. The simulated model and relevant physical parameters are depicted in Figure 5.6. The slot and pit are centred on opposing broad walls and separated a distance  $p$  along the length of the waveguide. The slot's width is fixed to 0.8 mm, while its length,  $l_{\text{slot}}$ , is varied. The 1.59 mm thickness of the waveguide's top plate is accounted for in the slot's height. The circular pit is described by its radius,  $r_{\text{pit}}$ , and depth,  $d_{\text{pit}}$ , both of which are varied.

As proposed in [24], the individual elements were first characterized separately to obtain the com-

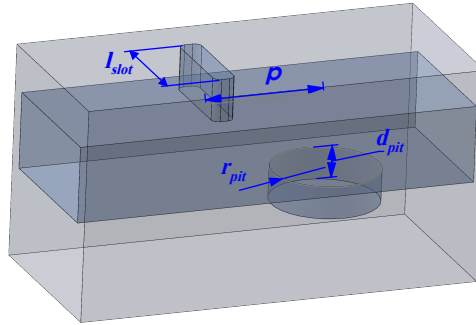


Figure 5.6: Simulated model of a slot-pit pair.

plex reflection coefficient,  $\Gamma$ , for varying slot lengths and pit dimensions. The slot's equivalent series impedance,  $Z_{slot}$  was also calculated and its behaviour as the length varied served to provide an estimate of suitable lengths for use in an array. For each slot length selected, a corresponding pit depth and radius was determined such that the magnitude of their reflections were approximately equal. An initial separation distance was determined by the phase of reflected waves to ensure they interfered destructively. The resulting set of dimensions were then incorporated in a parametric analysis of the combined element model described above.

Figure 5.7(b) plots the equivalent series impedance of an isolated slot as its length is varied for a simulated excitation frequency of 35 GHz. For a length of approximately 4.3 mm, the slot is resonant and its radiation resistance maximized. In the array, each slot will radiate an amount of incident power proportional to this resistance. To ensure a sufficient amount of power reaches all slots in the array, it is desirable to use slots below this resonant length. For short lengths, the reactance of the slot is seen to be inductive.

Figure 5.8 compares the complex reflection coefficient of an isolated slot and those of a pit. The slot's reflection coefficient corresponds directly to the equivalent impedance. The maximum magnitude for the slot occurs at resonance, while the circular pit's reflection coefficient magnitude asymptotically approaches a maximum as its depth increases. For below resonant length slots, the positive phase is equivalent to the inductive impedance noted above. It can also be seen that away from resonance, the phase characteristic of the slot is relatively flat. The reflected phase of the pit is observed to maintain an approximately constant value of  $\pi/2$  over the antenna's operating frequencies.

In order to reduce the number of parameter variations required for the characterization of the combined slot-pit pair, the results of the above comparison were used to generate an initial set of dimensions with suppressed reflections. The depth and radius of the circular pit are used to control the magnitude of its reflection coefficient, while the separation distance controls the phase of the reflective wave relative

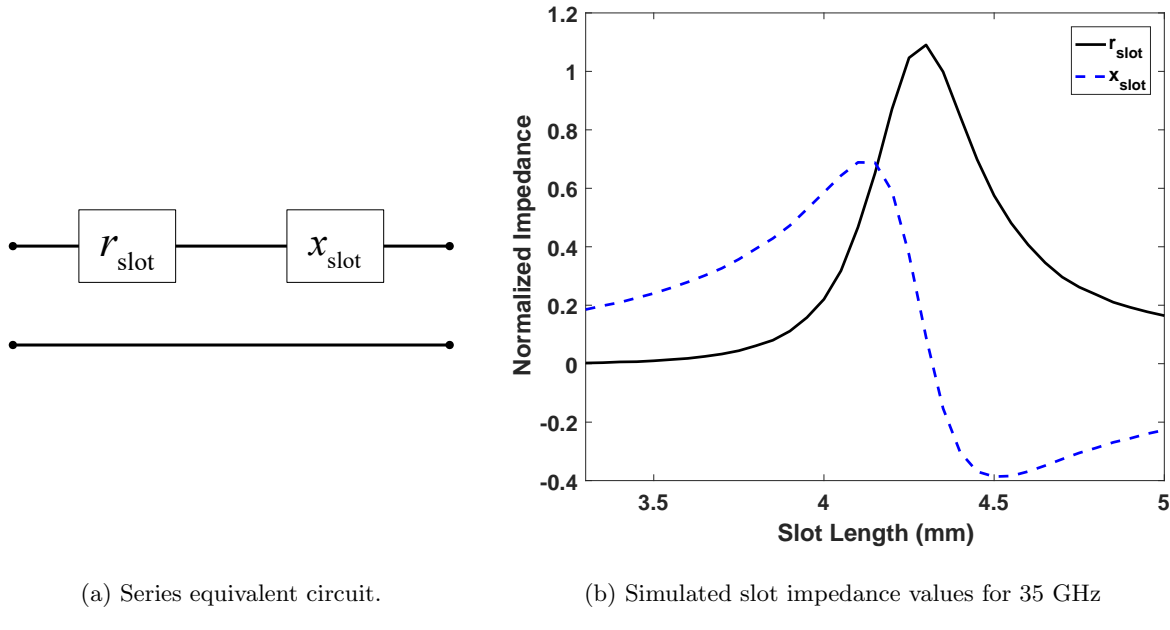


Figure 5.7: Slot equivalent series impedance.

to the slot's reflection coefficient. It was observed that equal magnitude reflections for slot lengths up to 4 mm could be obtained with a fixed pit radius of 2 mm and varying only the pit depth. Thus for each slot length, an initial pit depth was selected such that their isolated reflection coefficient magnitudes were equal.

As noted above, Figure 5.8 shows the phase characteristic of the reflection coefficient of short slots is relatively flat and constant for the circular pits. Furthermore, the phase of the short slots is relatively close in value to the constant phase of  $\pi/2$  observed for the pit. To specify an initial separation distance, these phases were assumed equal, thus an initial value of  $p = \lambda_{g,c}/4 = 3.25$  mm was used for all slot lengths. Assuming the reflection coefficient phases are equal, the resulting two-way path length of  $\lambda_{g,c}/2$  ensures reflections from the pit are out of phase with reflections from the slot. Therefore, these reflected waves will sum to zero if their magnitudes are also equal.

The pit depth and separation were varied slightly from the generated initial values for slot lengths ranging from 3.4 to 4 mm. The resolution of the parameters was limited to 0.1 mm due to the considerations discussed in the design overview. It was found that reflections could be reduced by 18 dB or better for a constant separation slightly larger than  $\lambda_{g,c}/4$ . To simplify the array's implementation, the separation was set to a constant 3.3 mm and only the depth of the pit was varied, with one exception. In the case of the 4.0 mm slot, the pit radius was required to be increased to 2.2 mm to sufficiently suppress the reflection. Figure 5.9 shows the resulting reflection coefficient for a slot of length 3.7 mm and a pit of depth 0.6 mm over the operating frequency range of the antenna. A minimum is clearly

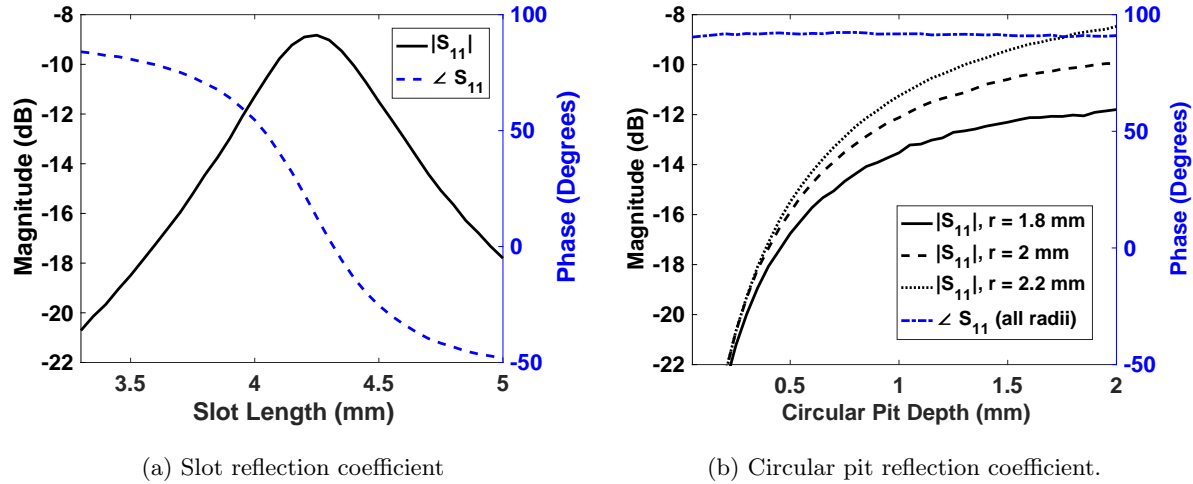


Figure 5.8: Reflection Coefficient of Isolated Elements.

seen near 35 GHz. A summary of the resulting pit sizes and the improved reflections is seen in Figure 5.10.

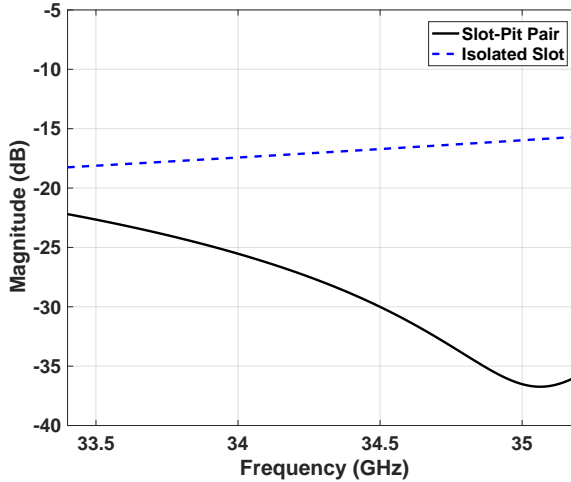
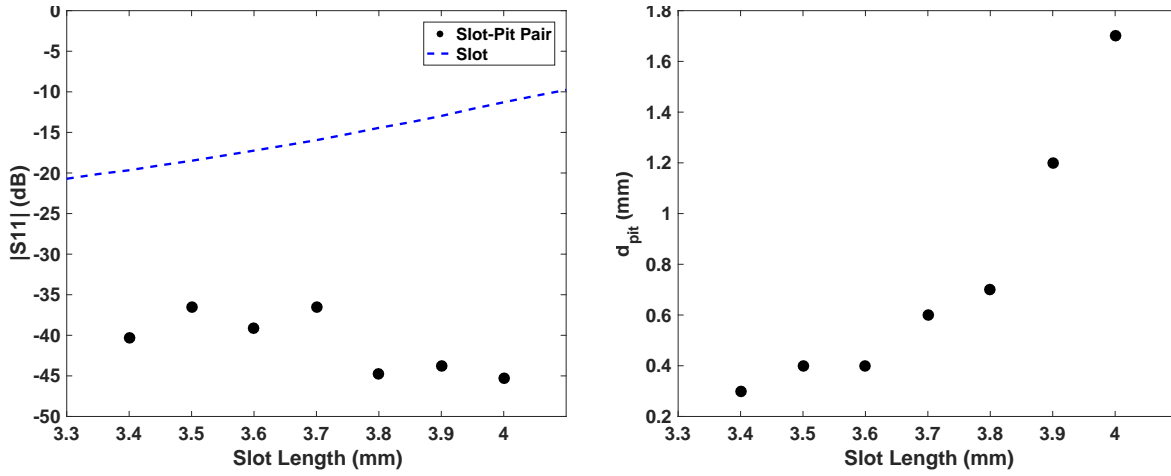


Figure 5.9: Reflection coefficient improvement for a 3.7mm slot with a circular pit of depth, 0.7mm.

### 5.3.2 Element Coupling and Phasing

To determine the coupling values of the designed set of slot-pit pairs, a uniform array was simulated. Modelling an array similar in length to what is expected in the implemented design allows for the effects of both mutual coupling between radiating slots and the multiple reflections internal to the waveguide to be accounted for. In observing the resulting beam steering angle, the serpentine length can be adjusted to ensure element's are excited by the desired progressive phase shift.

The simulated array is seen in Figure 5.11. The total length of the array was selected based on the



(a) Reflection coefficient with and without circular pits.

(b) Circular pit depths for each slot length. Pit radius was 2.0mm except for a slot length of 4.0mm, where it was increased to 2.2mm.

Figure 5.10: Summary of Slot-Pit Pair Design.

beamwidth estimate given in Equation (2.18) of Chapter 2. For a two degree beamwidth and element spacing of 6.3 mm, 40 slots are required. The total waveguide then consists of 20 unit cells seen in Figure 5.2. Slots, 1.59 mm in height, were placed along the center of the antenna's axis, with their corresponding pits placed 3.3 mm away. A modified length parameter,  $l'$  is indicated on the array. This dimension was introduced to simplify adjusting the serpentine length while maintaining a fixed element spacing. To increase the speed of simulation for the numerous variations, the waveguide was modelled as a perfect conductor and the external ground plane assumed infinite to allow the modelled external region to be localized to a relatively small volume above the slots. This volume was dimensioned such that the distance from any wall to its nearest slot was one half wavelength.

The array synthesis and design techniques presented in Chapters 2 and 3 and used in this work, produce an excitation distribution applicable to a single frequency. It was expected that the array's radiation pattern will deviate from the design as it scans due to the frequency dependencies of its elements. To minimize this effect, the array was designed at its centre frequency to reduce the maximum frequency deviation as the array is steered to its extreme angles. Thus, the uniform array was simulated for an excitation frequency of 34.3 GHz.

The uniform array was simulated for each of the slot-pit pairs described in Figure 5.10(b). The length parameter,  $l'$ , was nominally set to 29.5 mm to approximate the serpentine length of the waveguide designed in Section 5.2. To satisfy the phase relation for reflection cancelling arrays, Equation (3.15),  $l'$  was adjusted in 0.1 mm increments until the main beam was directed toward  $\theta_o = -9^\circ$ . This

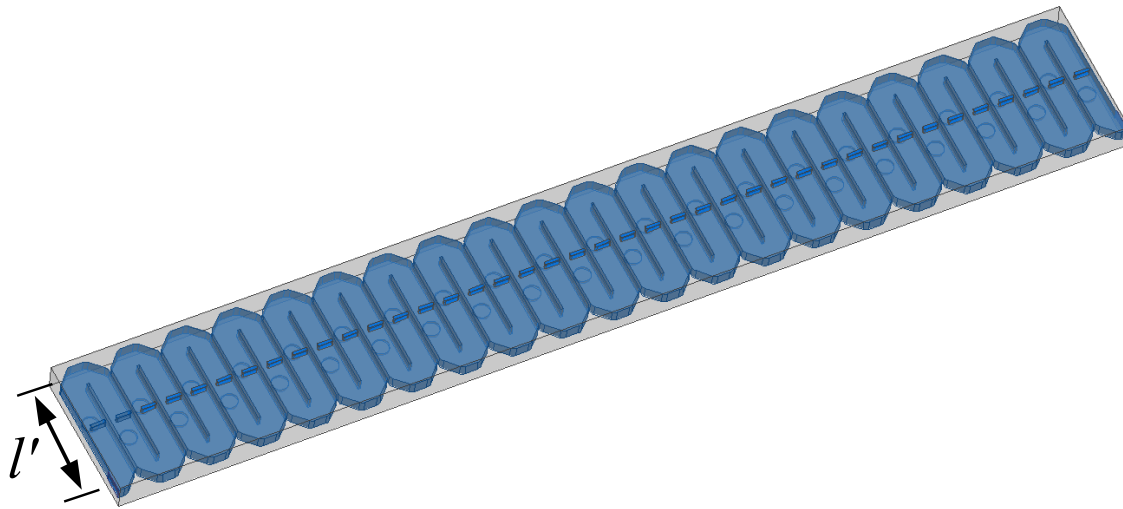


Figure 5.11: Simulated Uniform Array.

corresponded to the scan angle predicted by Equation (3.16) for the unadjusted waveguide. Figure 5.12 depicts an example radiation pattern for the  $l_{slot} = 3.6$  mm pair and the effect of the value of  $l'$  on the direction of the main beam.

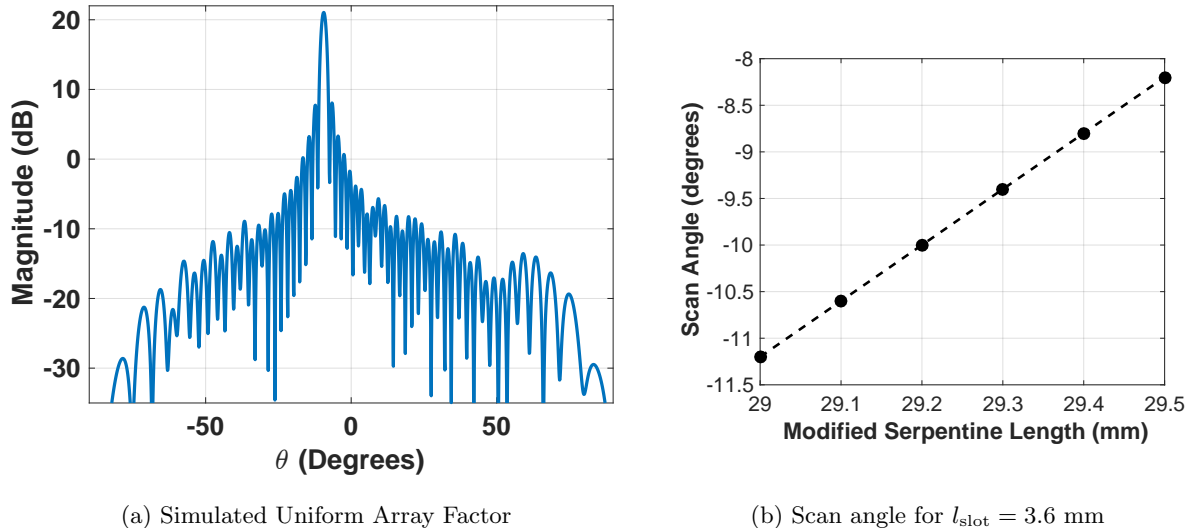


Figure 5.12: Uniform Array Simulation Results.

An estimate of the coupling value of a single slot-pit pair was obtained from the simulation result of the waveguide with the adjusted length. The estimate was calculated assuming all power not delivered to the termination at the end of the waveguide was radiated. This results in the expression

$$(1 - C)^M = |S_{21}|^2 \quad (5.1)$$

where  $M$  is the total number of slots. Equation (5.1) can be solved for the element's slot coupling  $C$ . Figure 5.13 summarizes the results of this design stage. The coupling values and waveguide lengths obtained for the slot-pit pairs designed in the previous section are shown.

It should be noted that the serpentine waveguide length between elements is not expected to be constant for the entire array. To realize a desired array factor, the slot lengths will be varied across the aperture of the antenna to taper its excitation. The serpentine length between each slot will then be adjusted to compensate for the variation in excitation phase of the slots as their length,  $l_{slot}$ , changes. Thus, the length of waveguide following a slot of length,  $l_{slot}$ , will be specified by the corresponding value of  $l'$  seen in Figure 5.13.

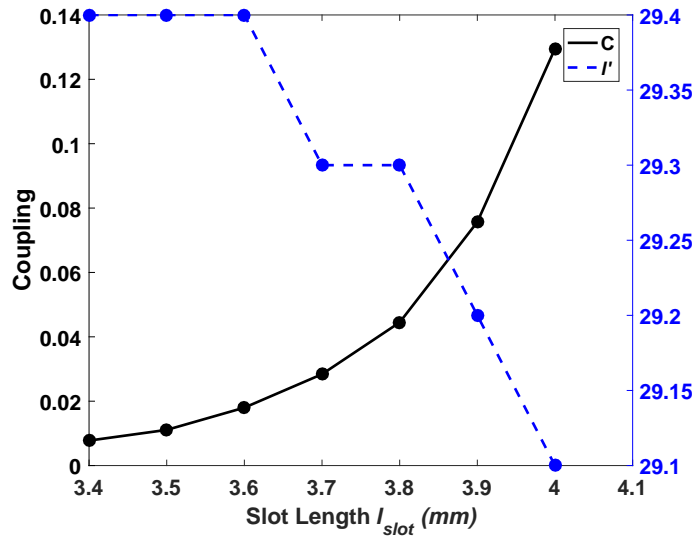


Figure 5.13: Summary of coupling values and adjusted lengths.

For the designed set of radiating elements, coupling values from approximately 0.008 to 0.13 were achieved. In the  $l_{slot} = 4.0$  mm case, the power absorbed in the load was reduced such that it was comparable to the reflected power magnitude. As negligible reflections were assumed in (5.1), it was decided to treat this case as the largest achievable coupling to maintain the simple design procedure. Furthermore, from Section 5.3.1, it was seen that this was the approximate limiting case where reflections could be suppressed with a fixed spacing. Smaller coupling values could be achieved; however, it was thought that the minimum coupling value of 0.008 would be sufficient for array synthesis. Thus, it was decided to proceed with implementing an array from the above values.

## 5.4 Taylor-Villeneuve Implementation

For the array to meet the specified SLL of -20dB, its amplitude distribution must be tapered. From the discussion in Chapter 2, the Taylor-Villeneuve array tapering permits a design with specified SLLs and results in excitation amplitudes that are practical to obtain in travelling-wave designs. The reflection cancelling element design of the previous section, however, resulted in a limited, discrete set of available coupling values due to fabrication resolution. As the functions determining the excitation values of the Taylor-Villeneuve array are continuous, a significant deviation may result.

In order to achieve the desired SLL without requiring increased fabrication tolerances and associated costs, an approximate Taylor-Villeneuve distribution was designed. The excitation magnitudes and corresponding ideal coupling values for an array with a SLL exceeding the specification were first calculated. The slot lengths producing the coupling values nearest those calculated were then selected. To account for the resulting increase in beamwidth, the length of the array was increased. For this design, the calculated array factor was specified for a -25 dB SLL and 48 slots.

As it was introduced in Chapter 2, the Taylor-Villeneuve array is a compromise between the Chebyshev array and a uniformly excited array. The  $\bar{n}$  parameter specifies the dominant behaviour of the Taylor-Villeneuve array. A value of  $\bar{n} = 0$  produces a uniform array, while  $\bar{n} = N/2$  results in a Chebyshev distribution. An initial value of  $\bar{n} = 12$  was selected as it represented an equal compromise. The excitation amplitudes,  $A_n$ , of the resulting  $M = 48$ , -25 dB SLL Taylor-Villeneuve were then calculated.

To determine the required coupling values for the calculated excitation amplitudes, the process described in Chapter 3 for reflection cancelling arrays was modified to include a specified amount of power to be absorbed in the load,  $P_l$ . For this array, a value of  $P_l$  was selected, corresponding to five percent of the total power absorbed in the load at the centre frequency. The normalized radiated power from each slot was found from

$$P_{\text{rad},n} = (1 - P_l) \frac{A_n^2}{\sum_{m=0}^{N-1} A_m^2} \quad (5.2)$$

where the  $(1 - P_l)$  term represents the total radiated power. The following recursive relationship was used to estimate the incident power,  $P_{\text{inc},n}$ , to each slot

$$P_{\text{inc},n} = P_{\text{inc},n-1} - P_{\text{rad},n-1} \quad (5.3)$$

where  $P_{\text{inc},0} = 1$  is the total normalized power at the input of the array. From Equations (5.2) and (5.3)

the calculated coupling of each slot-pit pair is

$$C_n = \frac{P_{\text{rad},n}}{P_{\text{inc},n}} \quad (5.4)$$

These calculated coupling values were used to select each slot's length based on the nearest available coupling value in Figure 5.13. Figure 5.14(a) shows the resulting variation in slot length along the array's aperture, while Figure 5.14(b) compares the corresponding simulated coupling values,  $C'_n$ , with the ideal values,  $C_n$ , calculated for the synthesized array distribution. It can be seen that as the required coupling values increase, the deviation in the available simulated coupling from the calculated value also increases. This should be expected from the discrete slot lengths used and the exponential-like growth in element coupling as slot length increased.

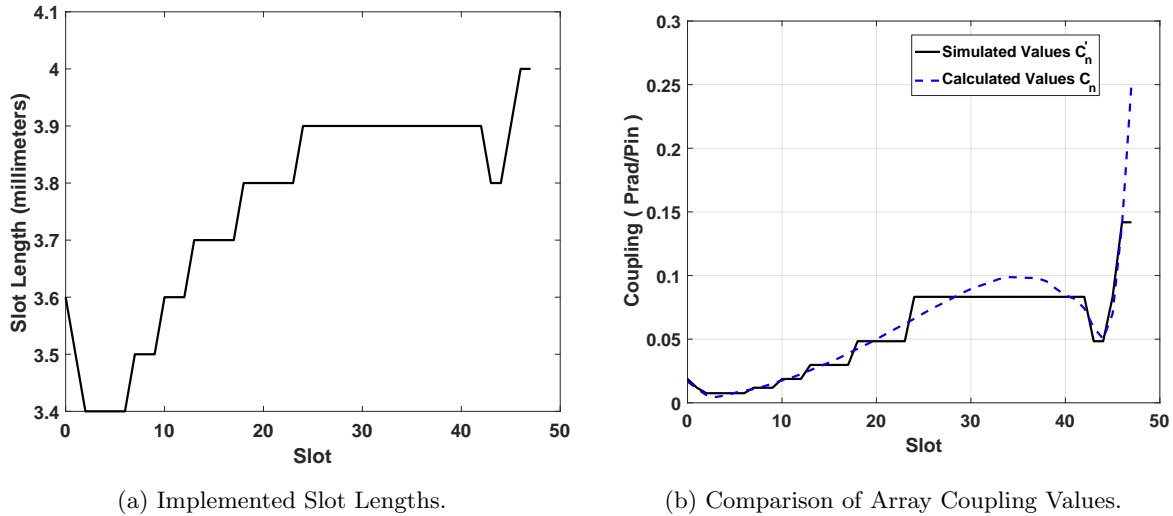


Figure 5.14: Summary of Selected Slot Lengths and Coupling Values.

To observe the effect of the coupling value discrepancies on the radiation pattern of the array, the predicted excitation amplitudes,  $A'_n$ , that result from the simulated coupling values were calculated using

$$A'_n = \sqrt{C'_n P'_{\text{inc},n}} \quad (5.5)$$

where the incident powers were determined recursively from

$$P'_{\text{inc},n} = P'_{\text{inc},n-1} (1 - C'_{n-1}) \quad (5.6)$$

assuming  $P'_{\text{inc},0} = 1$ . These estimated amplitudes are compared with the ideal excitation distribution for the Taylor-Villeneuve array in Figure 5.15(a). The corresponding array factors were also calculated

and plotted in 5.15(b). As expected, the predicted array factor differs from the ideal case; however, the maximum SLL is approximately -22.5 dB and satisfies the antenna specifications. Based on these results, it was decided to proceed with this design and simulate the entire structure.

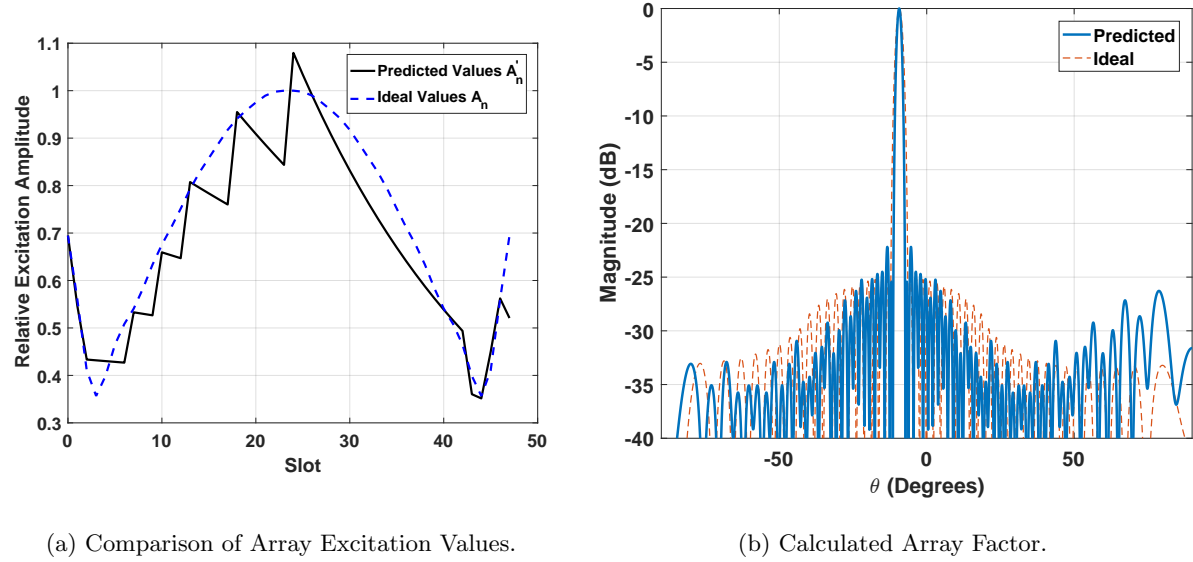


Figure 5.15: Summary of Approximate Taylor-Villeneuve Distribution.

## 5.5 Simulation Results

The approximate Taylor-Villeneuve array designed in the previous section was modelled in HFSS and is seen below in Figure 5.16. The slot lengths from the input on the left to the termination on the right are given in Figure 5.14(a). For each length, the corresponding modified serpentine length and pit depth are described in Figures 5.13 and 5.10(b) respectively. The waveguide is modelled in an aluminum conductor with dimensions 18 x 4 x 0.3125 in. The length and width were selected in consultation with the machine shop to be as large as practical to provide the largest possible ground plane. The total height was determined by the thickness of the cover in which the slots are cut, the waveguide height, and the maximum pit depth. In modelling the total aluminum structure, the effect of conductor losses are incorporated in the simulation's results. Furthermore, the external ground plane from the uniform array simulation was removed, and the exterior modelled region and radiation boundary extended to encompass the entire antenna structure.

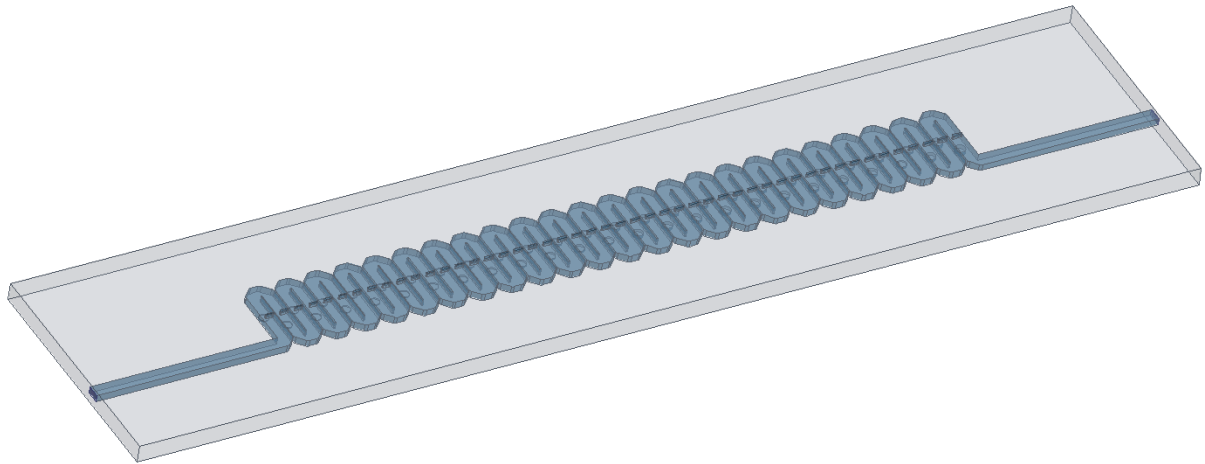


Figure 5.16: Simulated Designed Array. Grey region indicates the aluminum conductor.

### 5.5.1 Radiation Patterns

The simulated total gain of the array in its scanning plane is plotted in Figure 5.17. The radiation patterns for a number of example frequencies are shown, including the maximum and minimum frequencies, and the resulting broadside frequency of 34.93 GHz. As plotted here, the gain incorporates the directivity of the array, conductor losses in the waveguide, and power reflected at the input and absorbed in the load. The gain ranged from 19.5 dB to 20.09 dB over the array's operating frequencies. Broadside radiation occurs for a frequency slightly lower than intended, and is attributed to designing the array distribution at the center frequency of 34.3 GHz. The maximum gain at this frequency is comparable to the patterns of other frequencies, indicating that the reflections of the slots and bends were successfully suppressed. With the exception of the 33.4 GHz pattern, the SLLs are more than 20 dB below the maximum. In this case, the SLL is -19.77 dB, negligibly worse than the specified requirement.

### 5.5.2 Scanning Performance

The simulated radiation patterns described above indicated the designed antenna was suitable for the envisioned radar. To further verify its viability, performance metrics of the array were determined over its operating bandwidth. In particular, the beam scanning direction, reflected and absorbed powers, and beamwidth and gain demonstrate the capabilities of the simulated antenna.

Figure 5.18 illustrates the scanning characteristic curve of the array. The antenna scans from  $-22.8^\circ$  to  $+3.6^\circ$  as its operating frequency increases. The scanning characteristic flattens slightly as it approaches broadside, requiring a larger frequency shift to scan the beam in this region. The result is that larger bandwidths and thus, increased range resolutions are achievable near broadside when compared

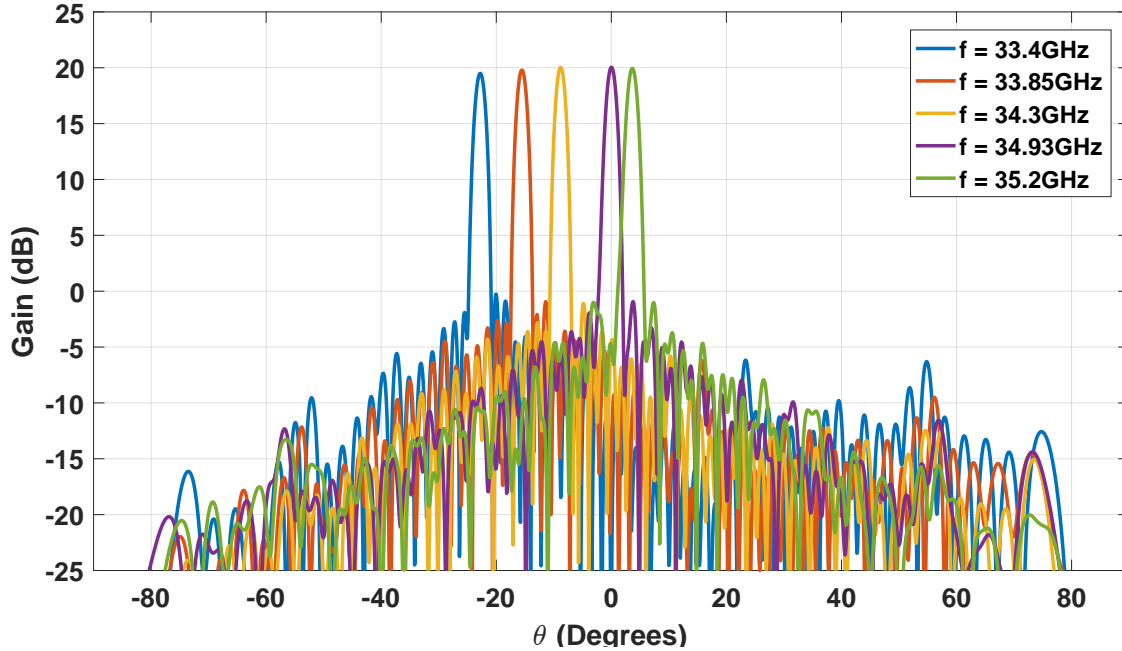


Figure 5.17: Simulated Gain of Designed Antenna.

to other steering angles.

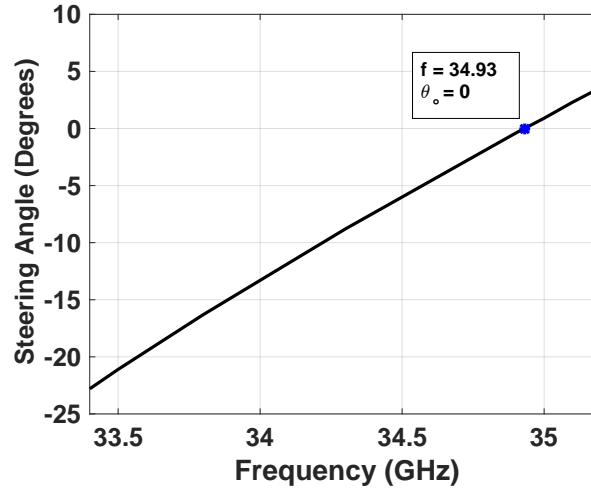


Figure 5.18: Simulated Array Scanning Characteristic.

The  $S_{11}$  and  $S_{21}$  network parameters, representing the reflection coefficient and the power absorbed in the load, are plotted in Figure 5.19. The antenna is seen to be well matched, with a worst-case return loss of 19.69 dB within its operating frequency range. It should be noted that at the broadside frequency of 34.93 GHz, there is no significant increase in return loss. This indicates the circular pits successfully suppress the reflections of the slots at this frequency. The magnitude of  $S_{21}$  demonstrates the frequency

dependence of the slots' radiation efficiency. At higher frequencies, the slots radiate more power and less power is absorbed in the load. At the design frequency of 34.3 GHz,  $S_{21} = -14.64$  dB, corresponding to 3.44 percent of the array's incident power absorbed in the load. The discrepancy between this value and the designed value of five percent, used in Equation 5.2, is attributed to the inclusion of conductor loss in the detailed array simulation.

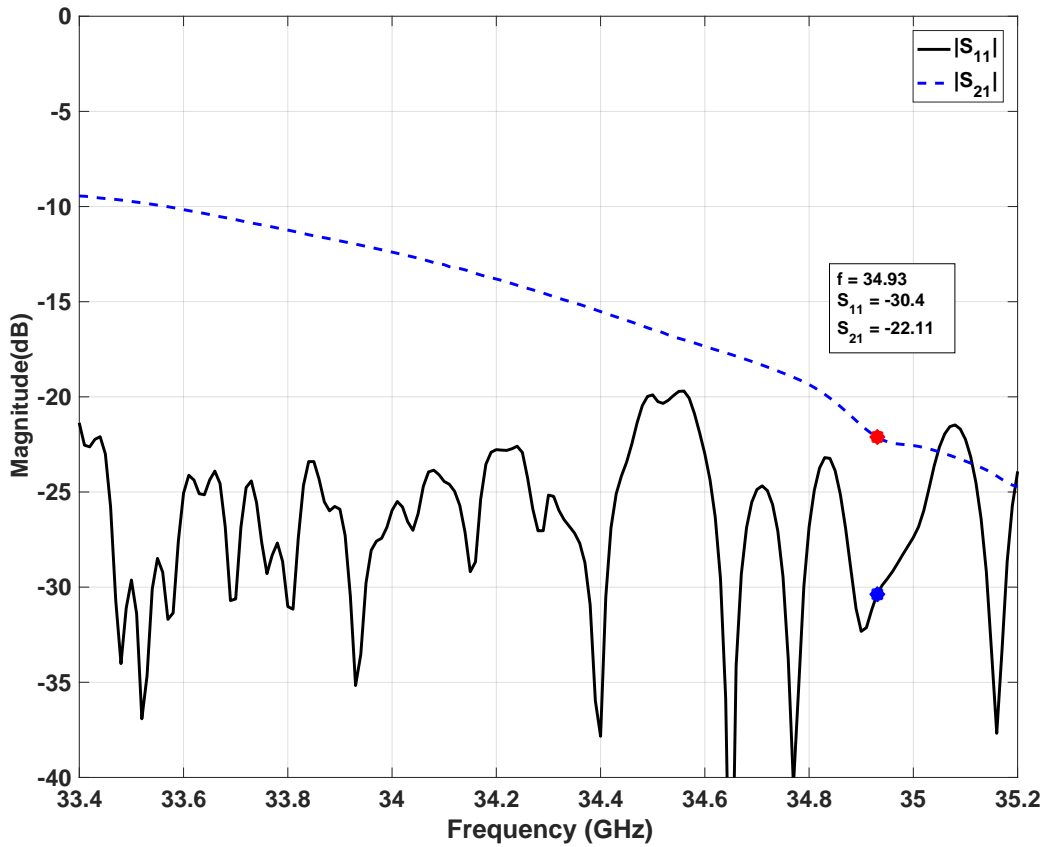


Figure 5.19: Simulated Network Parameters.

Figure 5.20 depicts the variation in gain and beamwidth over the antenna's total bandwidth. Both values are seen to be relatively flat with respect to frequency, with no significant performance degradation observed at broadside. This is in agreement with the reflection coefficient plotted in Figure 5.19 and further confirms the inclusion of the circular pits was effective in suppressing the reflections generated by the slots. The gain varied from 19.5 dB at 33.4 GHz to a maximum of 20.1 dB near 34.8 GHz. The beamwidth increased slightly from its minimum of  $1.67^\circ$  around the centre frequency to  $1.78^\circ$  and  $1.77^\circ$  and the minimum and maximum frequencies respectively. This will ensure a consistent performance in a radar system as the beam is steered.

The flat gain characteristic is one advantage of exciting the array with a travelling wave. As described

in Section 5.4, the radiated power from each slot is proportional to frequency. Designing the array excitation distribution for the centre frequency limits the resulting performance variation by minimizing the frequency deviation as the array scans. Moreover, the travelling-wave excitation leads to an additional self-regulating effect. At higher frequencies, the increased coupling limits the amount of power that reaches slots near the termination, effectively reducing the array's length and therefore directivity. This opposes the increase in gain due to the increase in power radiated and is indicated by the slight increase in beamwidth at higher frequencies. At lower frequencies, the opposite effect occurs. The reduction in slot coupling results in a more uniform array excitation and an increase in directivity that counters the reduction in gain due to the reduced radiated power. This effect is evident in the increased side lobe levels in the 33.4 GHz radiation pattern of Figure 5.17. The slight increase in beamwidth for lower frequencies is attributed to the reduction in the projected array length for increasing scan angles as described in Chapter 2.

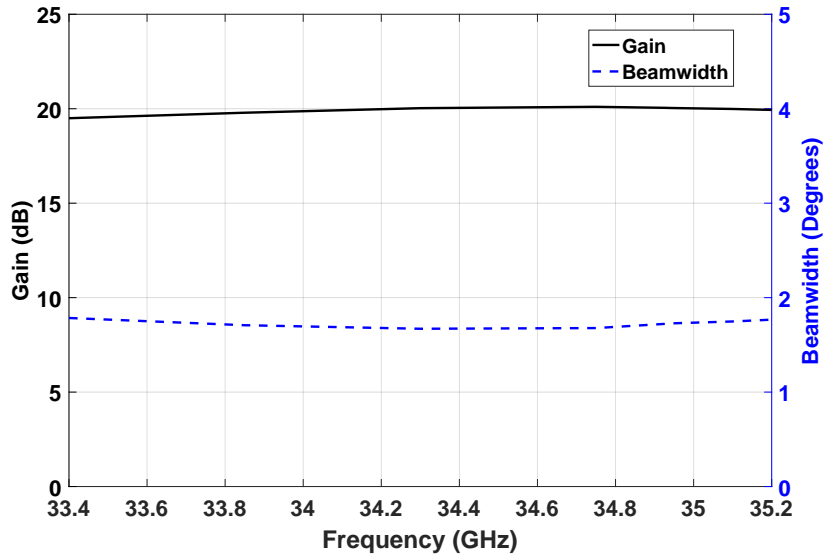
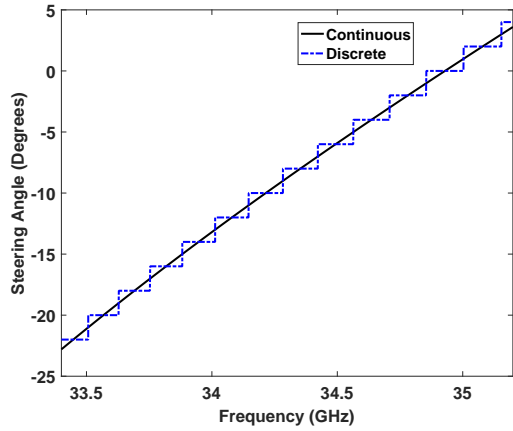


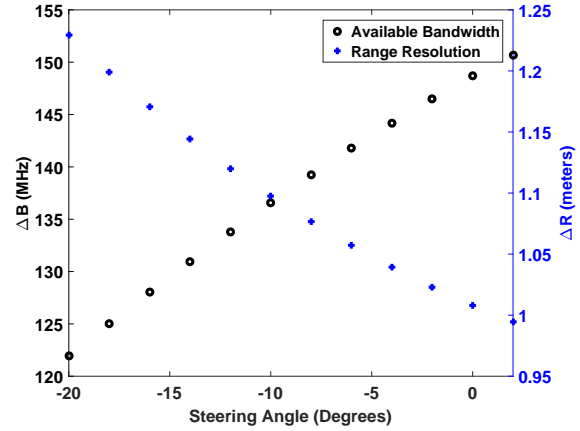
Figure 5.20: Simulated maximum gain and beamwidth over the operating frequency range of the array.

An estimate of the range resolution was calculated by mapping the minimum and maximum angles in Figure 5.18 to the frequency-scanned waveguide characteristic, Equation (3.16). The resulting expression was used to calculate the array's steering angle for a set of finely-spaced frequencies. Figure 5.21(a) shows the result of discretizing this relation using the approach described in Section 4.2 and assuming a two degree scanning beamwidth. The discrete scan angles have a fixed amount of bandwidth,  $\Delta B$ , associated with them that can be utilized for range resolution. Figure 5.21(b) plots these bandwidths and the corresponding range resolutions,  $\Delta R$ , for each discrete steering angle. The worst case range resolution is calculated to be approximately 1.23 metres and improves to approximately 1.01 metres at

broadside.



(a) Calculated Scanning Characteristics.



(b) Calculated Bandwidths and Range Resolutions.

Figure 5.21: Calculated Discretized Scanning Characteristic and Range Resolution.

## 5.6 Summary

The overall dimensions and performance characteristics are summarized in Table 5.2. Where applicable, the values of the design specifications are repeated from Chapter 1. It can be seen that all design specifications have been satisfied in the simulation results, with the exception of the negligible increase in SLL that occurred for the largest beam steering angle. Based on these results, it was decided to proceed with the implementation and measurement of the designed waveguide-fed slot array.

Table 5.2: Proposed Radar and Antenna Specifications.

Dimension / Specification	Model Value	Specified Value
Physical Length	18"	-
Physical Width	4"	-
Radiating Aperture Length	29.6 cm	-
Gain	20 dB (typ)	-
Range Resolution	< 1.25m	1.5 m
Maximum Scan Angle	22.8°	20°
Scanning Beam width	1.8° (typ)	2°
Side Lobe Levels	-20 dB (typ)	-20 dB
Polarization	Vertical	Vertical

## Chapter 6

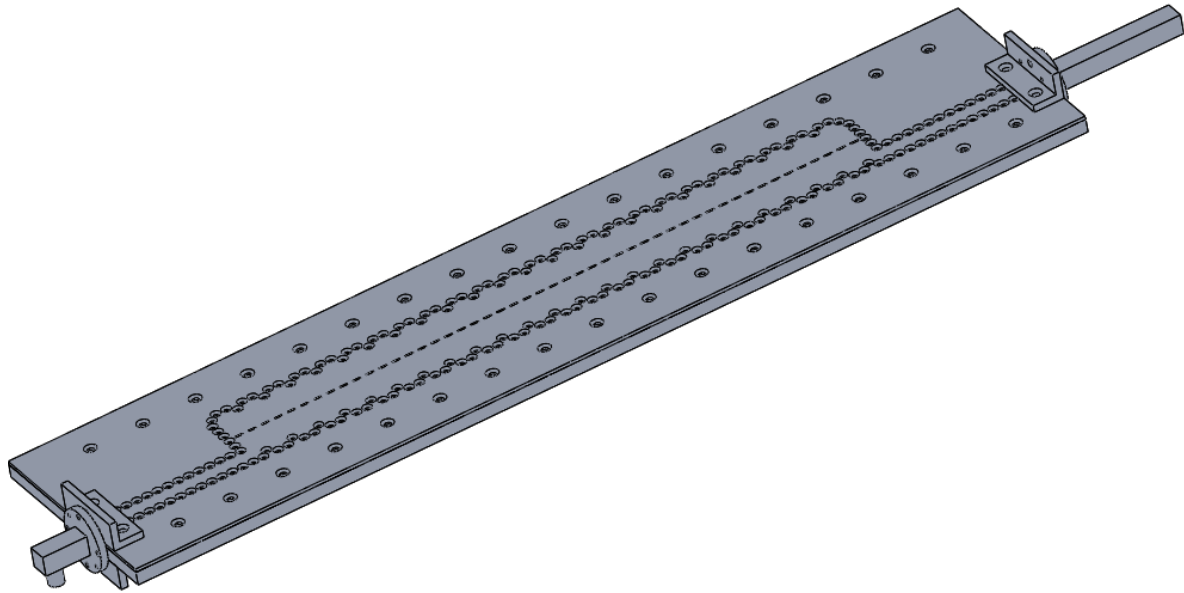
# Antenna Fabrication and Measurement Results

This chapter details the implementation and fabrication of the waveguide-fed slot array designed in the previous chapter. Its performance was verified through far-field and vector network analyzer measurements and the results are presented here. The scanning characteristics of the array will be used to estimate the antenna's effect on the range resolution of a frequency-scanning radar. A simple example using the radar equation will further illustrate the performance impact of the implemented antenna in the envisioned radar system. Finally, possible sources of discrepancies will be addressed through simulations.

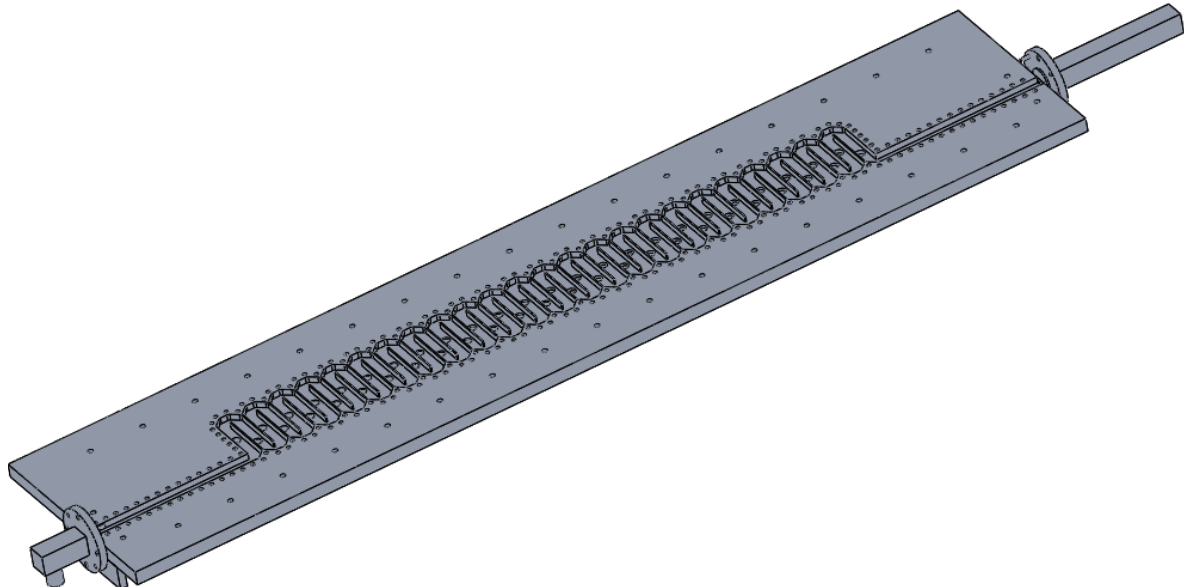
### 6.1 Antenna Fabrication

The SolidWorks model submitted to the University of Toronto's Machine Shop for fabrication is depicted in Figure 6.1, with detailed dimensioned drawings found in Appendix A. Based on the discussions in the previous Chapter, the antenna was fabricated as two main components. The waveguide with circular pits was milled from a solid aluminum block one quarter inch thick. Slots were cut into a sheet of aluminum one sixteenth of an inch thick, forming a top cover for the waveguide. The total length and width of the antenna were the same as previously simulated, 18 x 4 inches. Many finely-spaced threaded screws holes were drilled into the aluminum block around the perimeter of the serpentine waveguide. The large number of screws used in joining the pieces was to ensure the best possible electrical contact between the waveguide sidewalls and the top plate. The corresponding screw clearance holes in the top plate were

countersunk to provide an approximately uniform ground plane to the slots. Mounting brackets were also machined to allow mating to a standard WR22 coaxial transition at the input and a termination at the output.



(a) Complete Antenna.



(b) Antenna With Top Plate Removed.

Figure 6.1: SolidWorks Model of Fabricated Antenna.

## 6.2 Antenna Measurements

### 6.2.1 Radiation Patterns

The fabricated antenna's radiation performance was measured using the University of Toronto's far-field measurement facilities. The vertically polarized gain in the scanning plane was obtained over the antenna's operating frequency range in 10 MHz increments. The measured radiation patterns for select frequencies from 33.5 GHz to 35.07 GHz are plotted in Figure 6.2. These patterns correspond to scanning angles from  $-23.2^\circ$  to broadside. Immediately, it is seen that the antenna's measured patterns are shifted toward the negative  $\theta$  direction compared to the simulation. However, the specified angular scanning range was achieved, including the beam scanning through broadside. The measured pattern for a frequency of 33.4 GHz contained a grating lobe at  $\theta = +90^\circ$ , but was omitted as the main beam was steered to  $-24.9^\circ$ , which was further than required.

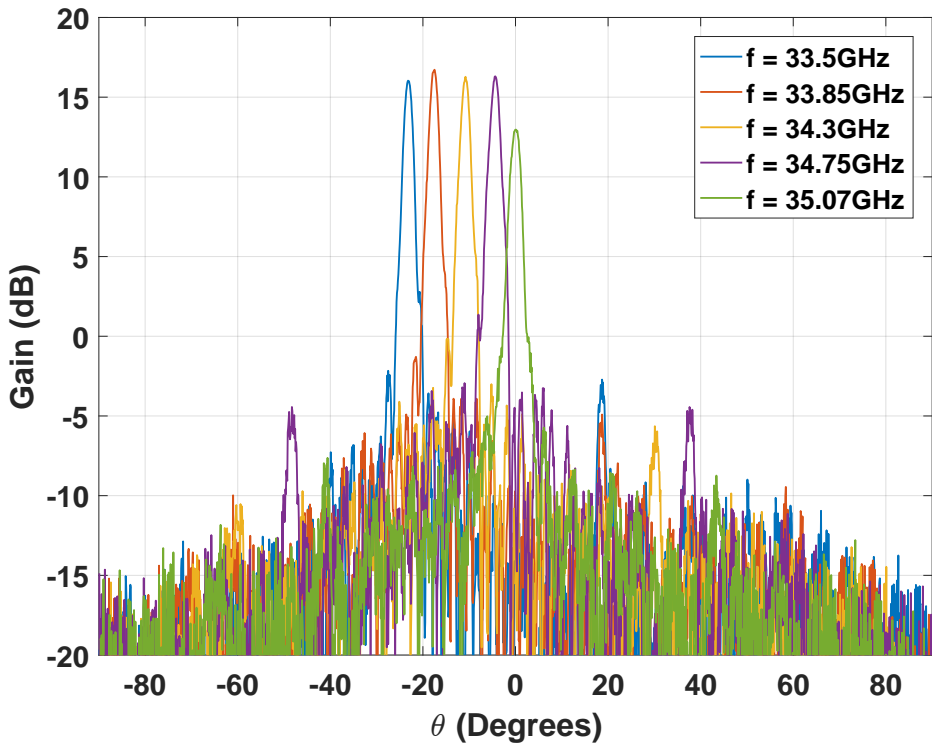


Figure 6.2: Measured realized gain of the fabricated antenna.

The radiation patterns in Figure 6.2 demonstrate a number of quantitative performance characteristics of the antenna. The maximum gain of each pattern is observed to be approximately 16 dB except near broadside where the gain is reduced by 3 dB. The side lobe levels range from approximately 16.5 to

18 dB below the main beam's maximum, suggesting a phase and/or magnitude error in the excitation of the slots relative to the designed distribution. These measured performance values are noticeably reduced when compared to the simulated performance discussed in Section 5.5 and are further addressed in Section 6.4.

Qualitatively, a number of irregularities can be seen in the radiation patterns. Increased side lobe levels occur approximately  $\pm 45^\circ$  away from the main beam direction. The magnitudes of these additional side lobes are at least 20 dB below the maximum, falling within the specified SLL performance of the array. Thus, they should not significantly impact the performance of a radar using this antenna. Shoulders can also be seen in the main beam for certain frequencies and indicate slight errors in the slots' excitation phases. The pattern measured at 33.5 GHz contains one such example. The narrow angular width of these shoulders will limit their degradation of radar performance. These irregularities will also be further addressed in Section 6.4.

### 6.2.2 Scanning Performance

To summarize the antenna's performance over its angular scanning range, performance metrics were extracted from the measured radiation patterns for frequencies in 10 MHz increments. Furthermore, the antenna's behaviour at its input was observed using a vector network analyzer. These characteristics permitted a more detailed comparison of the simulated and measured performances of the antenna, as well as provided more insight on some of the observed characteristics of the radiation patterns.

Figure 6.3 plots the measured scanning characteristic curve of the array as it scans from  $-24.9^\circ$  to  $+1.4^\circ$ . The total absolute scanning range compares with the simulation's curve, with both results scanning approximately  $26.3^\circ$  total. It can be seen here that the shift in the scanning behaviour, noted in the previous section, is approximately  $2.2^\circ$ . Some of this effect can be attributed to alignment error in the measurement. Nevertheless, the design accounted for some tolerance in the scanning characteristic, and the specified scanning range is still achieved.

The magnitude of the measured reflection coefficient is plotted in Figure 6.4. The measurement shows the antenna is well matched for frequencies between 33.8 and 35 GHz, with a return loss better than 10 dB. Outside of this range however, there is a noticeable increase in return loss when compared with the simulated values. As expected from the radiation patterns, the reflection coefficient's magnitude reaches its maximum of approximately -4 dB near the broadside frequency of 35.07 GHz. The increase in the reflection coefficient magnitude for frequencies near 33.8 GHz and lower agree with the increased side lobe levels that occurred  $45^\circ$  from the main. In this frequency range, the beam is steered near  $-22.5^\circ$ .

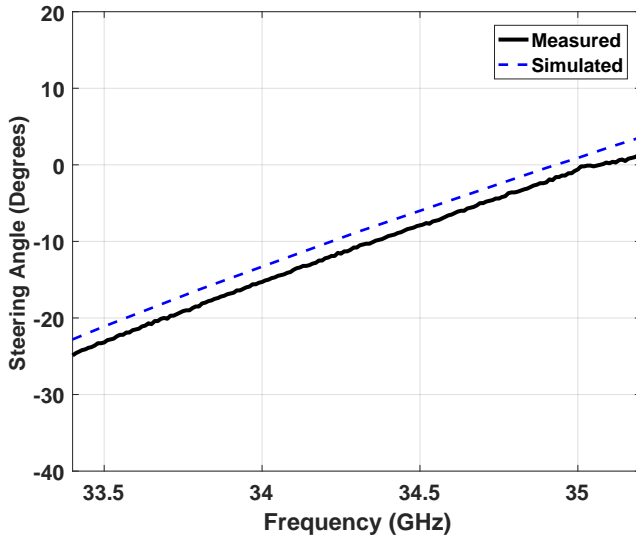


Figure 6.3: Measured Array Scanning Characteristic.

and the increased side lobe level appears as an approximate conjugate beam. This corresponds to a larger reflected wave produced inside the waveguide for these frequencies. This effect is illustrated in Figure 6.5. Figure 6.5(a) plots the pattern measured at 33.7 GHz where the effect was most prominent, while Figure 6.5(b) illustrates an exaggeration of the resulting fan beams.

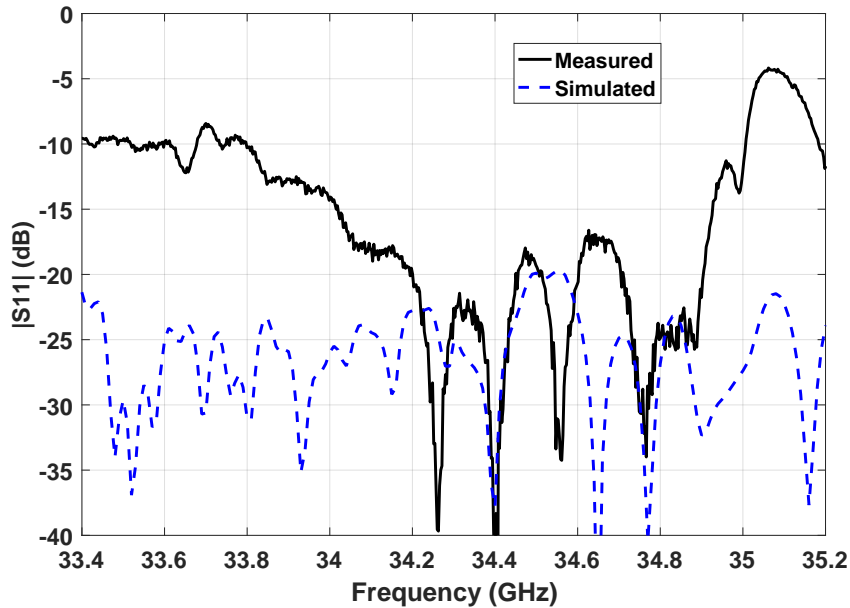
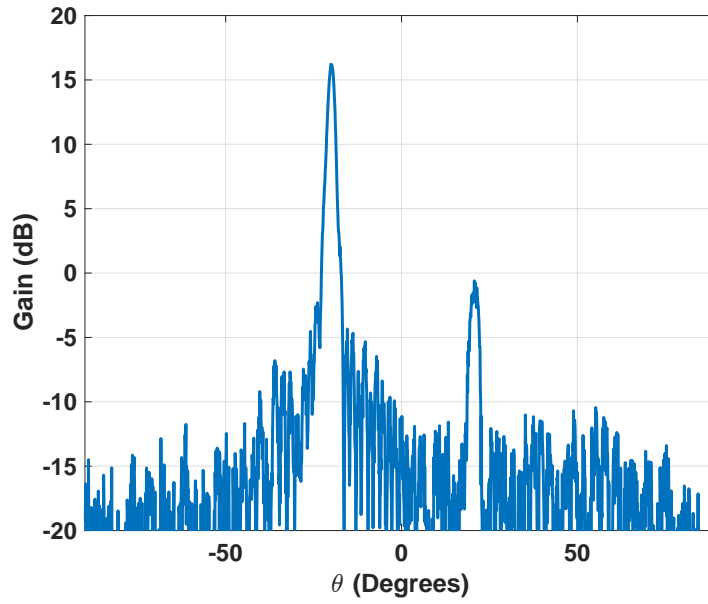
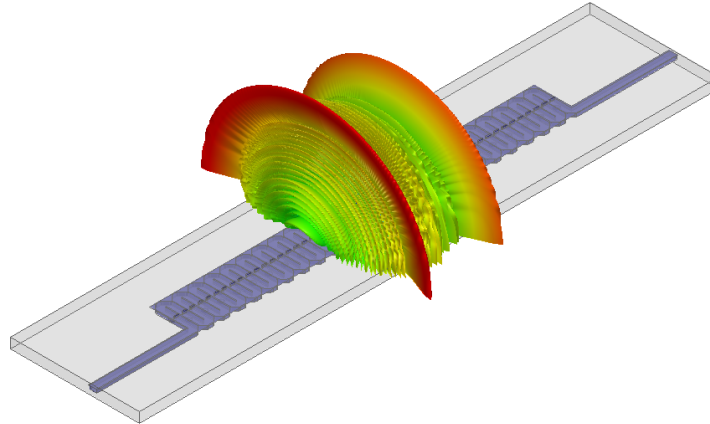


Figure 6.4: Measured Reflection Coefficient.



(a) Measured Radiation Pattern for 33.7 GHz.



(b) Illustration of the Conjugate Fan Beam.

Figure 6.5: Apparent Conjugate Beams.

The maximum gain and half-power beamwidth were extracted from the measured radiation patterns for each frequency point and are plotted in Figure 6.6. Away from broadside, both characteristics agree with the relatively flat shape of the simulation results; however, the value of the gain is reduced by approximately 4 dB when compared with the simulated model. As the measured beamwidth agrees with the simulated value in this region, it suggests that the primary reason for this reduction in gain is due to losses within the waveguide and not due to reduced directivity. Again, the gain is seen to be further reduced as the beam is steered toward broadside, while the beamwidth is observed to increase significantly. The performance near broadside is explained by the large reflection coefficient magnitude seen in Figure 6.4. Much of the incident power is reflected, limiting the total power radiated, and thus

gain. This effect also prevents an appreciable amount of power from reaching slots near the end of the array, effectively reducing the antenna's length and producing a broader beam.

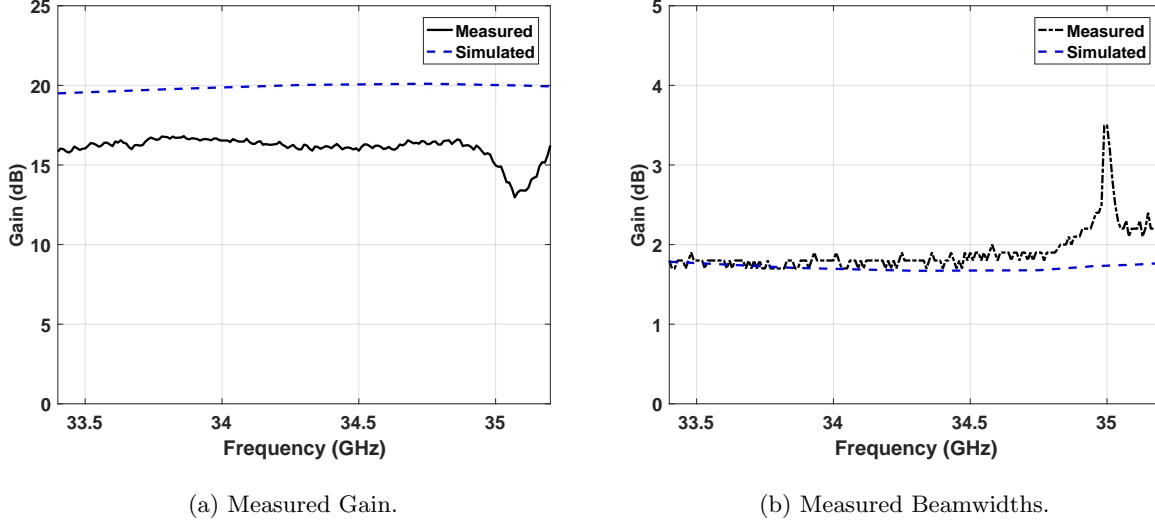
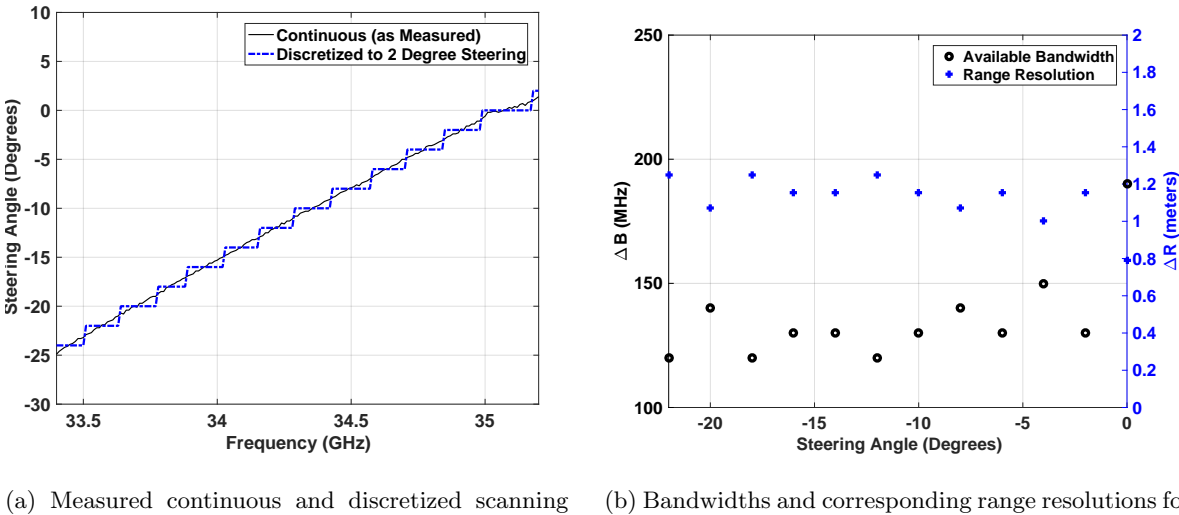


Figure 6.6: Measured Gain and Beamwidth.

The discretized measured scanning characteristic and resulting bandwidths and range resolution are depicted in Figure 6.7. The range resolution can be seen to be better than the specified 1.5 metres for all scanning angles and the shape of its characteristic agrees with the calculated estimate of Figure 5.21.



(a) Measured continuous and discretized scanning characteristics. (b) Bandwidths and corresponding range resolutions for each discrete steering angle of the antenna.

Figure 6.7: Measured scanning characteristic and resulting range resolution

### 6.2.3 Measurement Summary

Table 6.1 compares the measured and simulated typical values of the performance characteristics described in this section. The noticeable reduction in gain and the increased side lobe levels will negatively impact the performance of a radar system, particularly near broadside. The maximum range will reduce proportionally with the gain. The increased SLL will limit the ability to accurately resolve a target's angular position in applications where targets are expected to differ significantly in RCS values. Nevertheless, the measured range resolution, beamwidth, and angular scanning range agree with the simulated values and satisfy the design requirements outlined in Chapter 1. As these parameters determine a radar's ability to accurately detect and locate targets, the results suggest a viable antenna for use in a radar system.

Specification	Measurement	Simulation
Gain	16 dB (typ)	20 dB (typ)
Range Resolution	$\leq 1.25m$	$< 1.25m$
Maximum Scan Angle	$23.2^\circ$	$22.8^\circ$
Scanning Beam width	$1.8^\circ$ (typ)	$1.8^\circ$ (typ)
Side Lobe Levels	-16.5 dB (max)	-19.77 dB (max)

Table 6.1: Comparison of measured and simulated performance.

## 6.3 Radar Equation Example

To illustrate the impact the gain of the fabricated antenna may have on a radar system, a simple example calculation may be completed using the radar equation. Here, the maximum predicted range will be calculated for the highway monitoring example described in Chapter 1 using the antenna configuration depicted in Figure 1.7. The receive antenna is assumed to be the designed frequency-scanned waveguide-fed slot array. To represent a practical scenario, the transmit antenna is assumed to be a commercially available horn antenna with a relatively wide beamwidth. One candidate antenna for this application is found in reference [42], with a gain of 20 dB over an azimuthal beamwidth of approximately  $17^\circ$ . From the discussion on radar cross sections in Section 4.3.3, a minimum expected RCS value of  $1 \text{ m}^2$  will be assumed to represent either a person or large animal.

In order to determine a maximum range using the radar equation, additional factors related to the radar's performance are required. As this work focused solely on the design of the receiving antenna, practical values were adopted from a radar implemented by Daimler and described in [7, 43]. This radar was designed for a similar frequency-scanned application in the same frequency-band as this work and relevant performance parameters are found in table 6.2. From the FMCW range equation (4.3), the

maximum range the radar can display is specified by the product of its FMCW ramp rate and receiver bandwidth. For the 600 kHz receiver bandwidth and 27 GHz/s ramp rate, the maximum instrument range is 3.33 km. For a more realistic maximum range for a radar incorporating the proposed antenna scheme of this example, this bandwidth was reduced to 150 kHz to provide a maximum instrument range of 833 m.

Parameter	Symbol	Value
Centre Frequency	$f_o$	34.3 GHz
Transmitter Power	$P_t$	0.5 W
FMCW Ramp Rate	$B/T_b$	27 GHz/s
Receiver Bandwidth	$B_r$	600 kHz
Receiver Noise Figure	$F_{sys}$	3.5 dB

Table 6.2: Daimler Radar Performance Parameters [7, 43].

Parameter	Symbol	Value
Transmitter Power	$P_t$	0.5 W
Transmitter Gain	$G_t$	20 dB
Receiver Gain	$G_r$	16 (20) dB
Target RCS	$\sigma$	1 m <sup>2</sup>
Wavelength	$\lambda_o$	8.75 mm
Minimum SNR	$(S/N)_{min}$	10 dB
Receiver Bandwidth	$B_r$	150 kHz
Receiver Noise Figure	$F_{sys}$	3.5 dB
Temperature	$T_o$	290 K

Table 6.3: Radar Range Equation Parameters.

The relevant factors for the radar range equation in this example are summarized in Table 6.3. In addition to the considerations described above, a minimum SNR of 10 dB was assumed as suggested by Skolnic in [44]. To calculate the predicted maximum range of a radar given a minimum SNR, the radar equation as presented in Equation (4.7) can be solved for  $R$  with substitutions from Equations (4.9) and (4.10). The resulting expression for a maximum range is then

$$R_{max}^4 = \frac{P_t G_t G_r \sigma \lambda_o^2}{(4\pi)^3 k T_o B F_{sys} (S/N)_{min}} \quad (6.1)$$

The maximum predicted range was calculated for both the simulated antenna gain of 20 dB as well as the measured typical gain of 16 dB. For the simulated antenna, the maximum range was 317 m, while for the measured antenna, it was reduced to 252 m. This simple calculations suggests that an improved antenna fabrication will result in an approximately 25 percent increase in radar range.

## 6.4 Discrepancies

In the discussions of Section 6.2, a number of discrepancies were noted in the measured performance of the antenna as compared to its predicted performance from simulations. Noticeable reductions in the antenna's performance were observed with respect to gain, side lobe levels, and return loss. It was expected that the dominant source of these discrepancies was the mechanical assembly of the antenna's top plate and bottom block. The use of screws to join the top plate to the waveguide allowed for air gaps to exist between the waveguide's interior sidewalls and its top broad wall. From the discussion in Chapter 3, this will result in increased conduction losses. The large number of countersunk screws used in joining the components, also introduced a significant source of error in alignment. The effect of these fabrication errors were investigated through simulations with HFSS.

The simulated model of the designed array was modified to incorporate approximations of the described assembly errors. A uniform height air gap was inserted between the sidewalls and the top broad wall, spanning the interior of the waveguide structure and is highlighted in green in Figure 6.8. The slots, as a set, were allowed to shift in the directions of the antenna's width and length. This was to account for the misalignment in bolting the top plate to the waveguide. The model was simulated as the air gap height and slot displacement varied. As there were a number of variations and frequencies to solve for, the infinite ground plane assumption and localized exterior volume were used to reduce simulation time.

The antenna's radiation performance degradation for increasing air gap heights was investigated first. Example radiation patterns for three frequencies with an air gap height of  $10 \mu\text{m}$  are plotted in Figure 6.9(a). Included for comparison are the patterns with no gap. An approximate 3 dB reduction in gain occurs for the patterns away from broadside. Near broadside, the gain is further reduced to approximately 6 dB below the ideal case. Figure 6.9(b) summarizes the result for increasing air gap heights. The maximum gain at the broadside frequency of 34.93 GHz is seen to decrease strongly with the height of the air gap while the reduction at other frequencies is less sensitive. This suggests that the return loss when the array is excited in phase is significantly impacted by the introduction of an air gap.

The effect of assembly misalignment on the antenna's radiation pattern was determined by simulating the array with increasing slot displacements. The radiation pattern was seen to be relatively insensitive to small slot displacements along its length, corresponding to the x-direction in Figure 6.8. For increasing displacements in the y-direction, denoted  $e_y$ , side lobes levels at angles  $\pm 45^\circ$  increased proportionally. This agrees with the measured results of Figure 6.2, where the effect was most prominent for the pattern measured at 34.75 GHz. The simulated pattern for this frequency is plotted in Figure 6.10 for a number

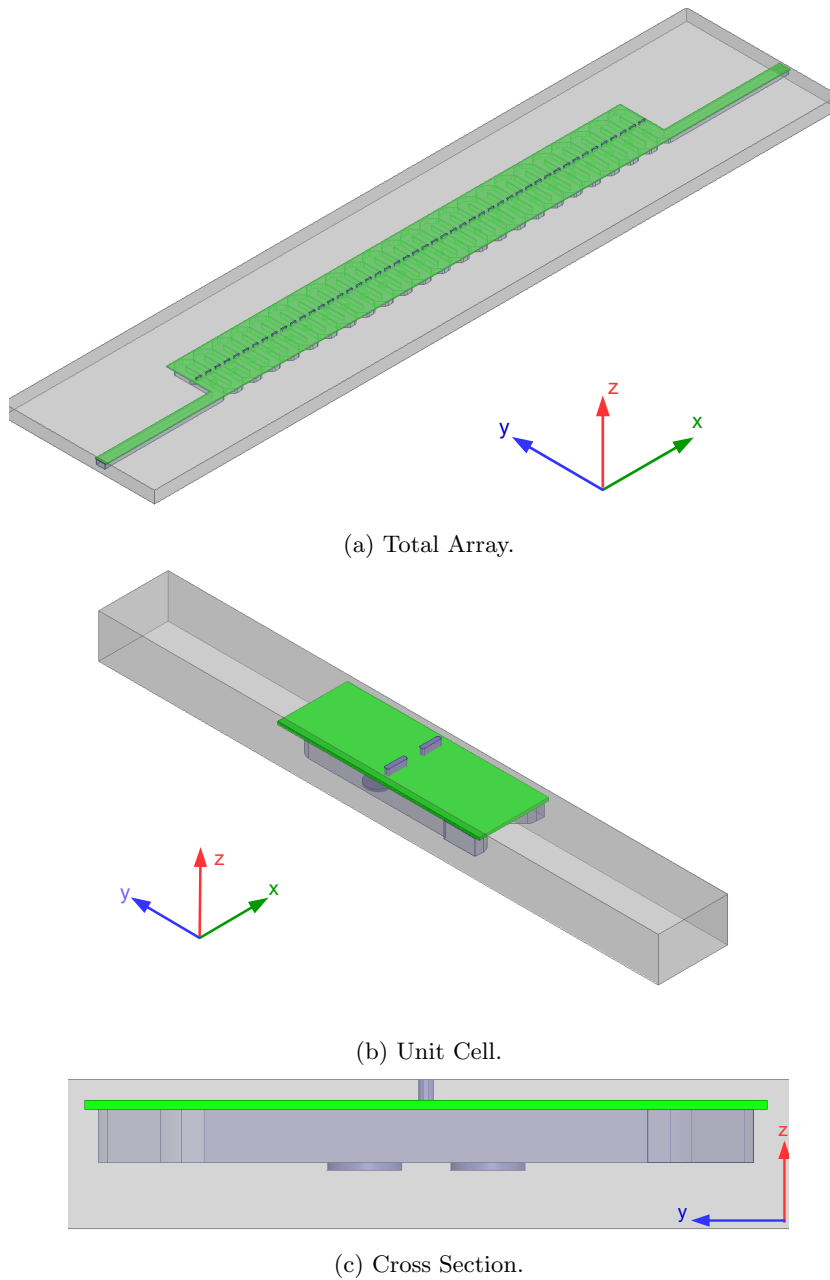
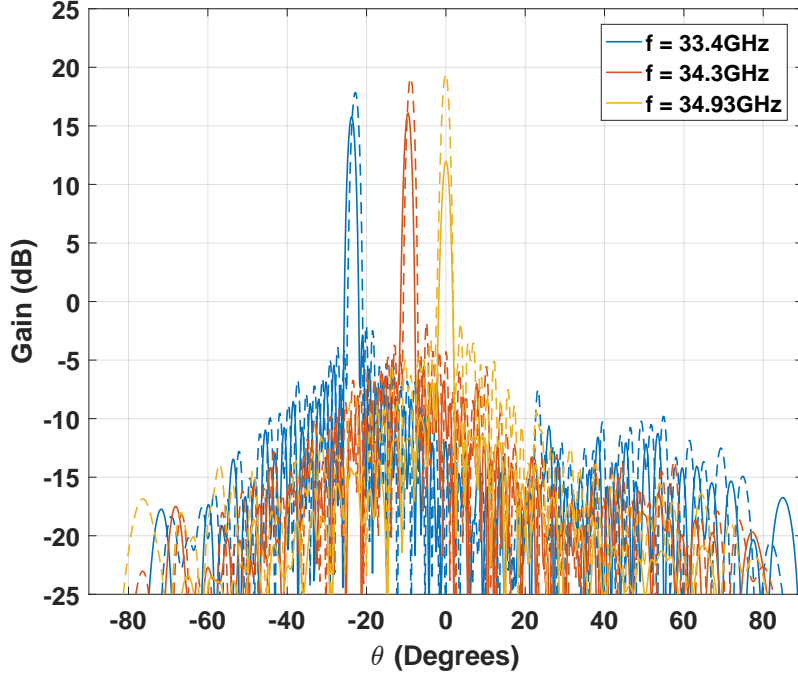
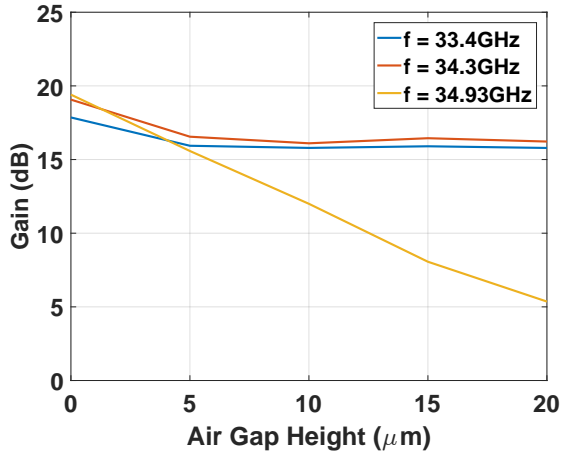


Figure 6.8: Simulated Model with Air Gap. Air gap is indicated in green.



(a) Simulated radiation patterns with a 10 $\mu\text{m}$  air gap. Dotted line patterns indicate gain without a gap.



(b) Maximum gain variation with air gap height.

Figure 6.9: Gain Reduction with Air Gap.

of values of  $e_y$ . The increase in side lobe levels is attributed to the error that arises in the progressive phase shift of successive slots. If all slots are displaced equally in the positive y-direction, the effective waveguide length between slots alternates between slightly shorter than designed and slightly longer. The result is an excitation phase error that reverses in sign between each slot and produces side lobes at  $\theta_0 \pm 45^\circ$ . This effect was reported and verified for a similarly constructed waveguide-fed slot array in [12].

Based on the results described in Figures 6.9 and 6.10 a possible configuration that may account for

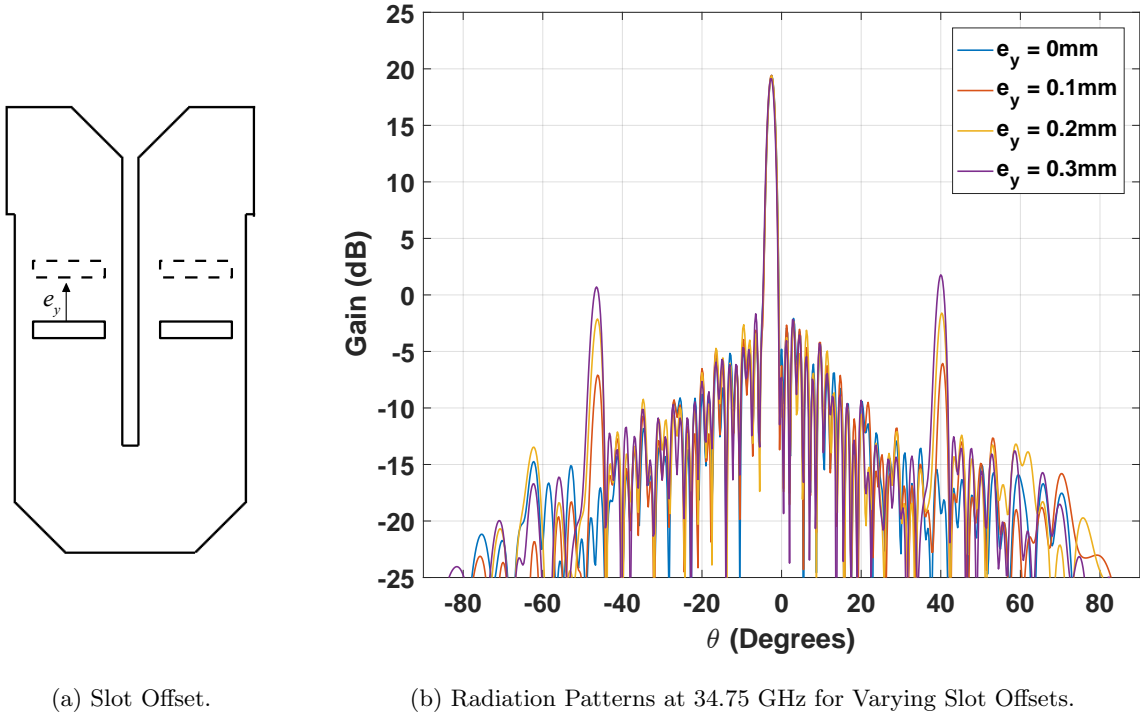


Figure 6.10: Increased Side Lobe Levels with Slot Offset.

the discrepancies between the measured and designed performance was determined. An air gap height of  $10 \mu\text{m}$  and slot displacement,  $e_y = 200 \mu\text{m}$ , resulted in performance that better approximated the measured results. Radiation patterns from the adjusted simulated model are shown in Figure 6.11. The peak gain away from broadside is approximately 16 dB, agreeing with the measured values of Figure 6.2. The simulated gain at broadside is slightly below 12 dB which is approximately 1 dB below the measured gain at broadside. This result is not unexpected as the air gap was modelled with uniform height. In reality, the air gap's profile is non-uniform and likely exists as many smaller air gaps distributed along the array. In this manner, the modelled gap is a worst case. In addition, the side lobes at  $\theta_0 \pm 45^\circ$  are increased to levels similar to those measured. Finally, although not observed when the air gap height or slot displacement were varied independently, side lobe levels near the main beam are increased to values ranging from approximately -19dB to -17dB. This is attributed to a compounding effect from both the excitation magnitude error resulting from losses in the air gap, and the excitation phase error due to misalignment.

Figure 6.12 plots the simulated reflection coefficient of the adjusted model of the antenna and the reflection coefficient obtained when the slots and pits are removed, with the latter demonstrating the effect of the air gap on the serpentine waveguide. Both plots show a large reflection coefficient near the broadside frequency, agreeing with the measured results. From this, it can be inferred that the

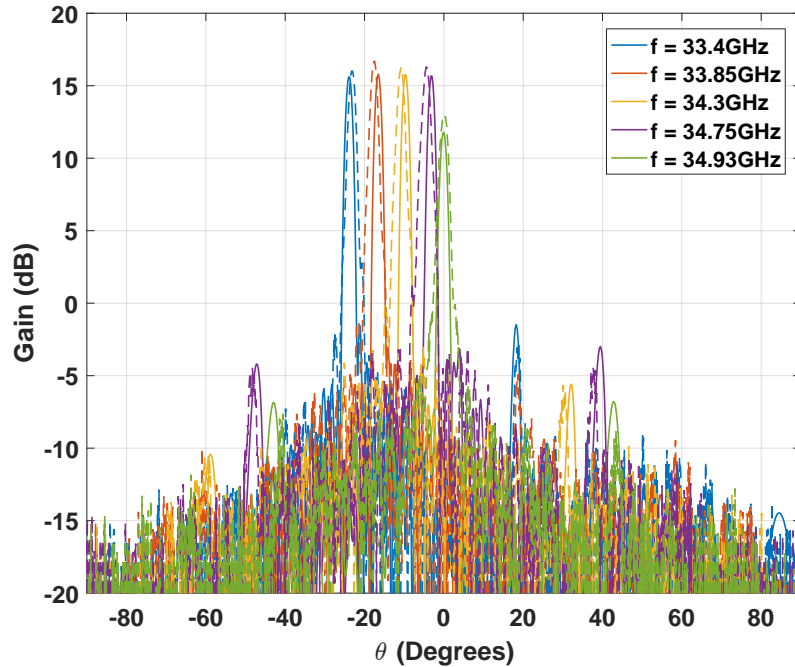


Figure 6.11: Modified Simulated Model Radiation Patterns. Measured patterns from Figure 6.2 are shown as dashed lines. Measured broadside and extreme steering angle patterns are corrected to 35.07 and 33.5 GHz respectively.

dominant source of the reflections is the air gap in the waveguide. An additional effect observed here is the increased return loss that occurred for beam steering to approximately  $-22.5^\circ$ .

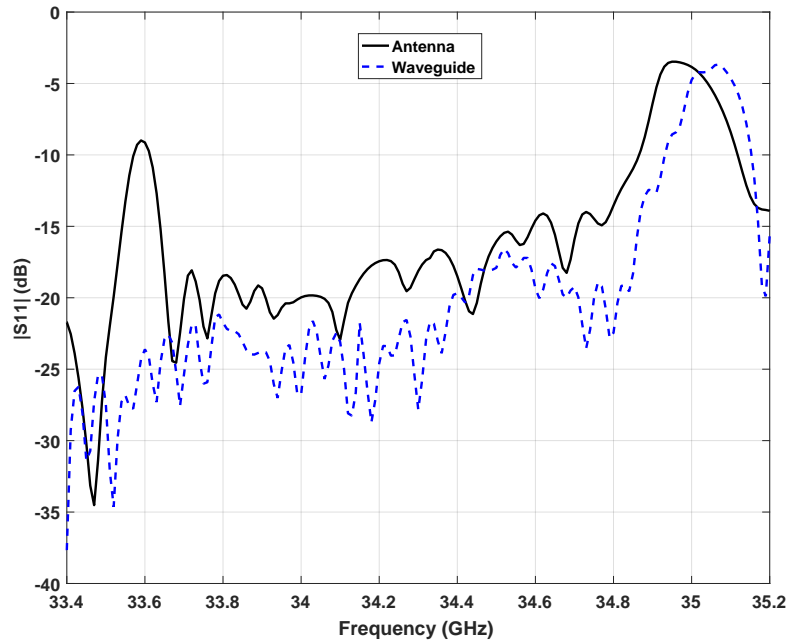


Figure 6.12: Modified Simulated Model Reflection Coefficient.

The results of this section highlight the importance of proper mating of the antenna's components. In particular, sufficient electrical contact between the interior walls of the waveguide is critical to an efficient design that can radiate toward broadside. From the discussion in Chapter 3, the waveguide should be manufactured using alternative methods if efficient operation is critical and costs permit. Moreover, by not using countersunk screws, these methods would also allow the components to be aligned more accurately, reducing the side lobes at  $\theta_0 \pm 45^\circ$ . Nevertheless, the summarized results of Section 6.2.3 show the performance of the measured antenna should enable a frequency-scanned radar to detect and locate targets in both angle and range.

## Chapter 7

# Radar Demonstration

The previous two chapters described the design and implementation of a waveguide-fed slot array for frequency-scanned radar applications. The antenna's performance was analyzed and determined to be suitable for use in a radar system. In this chapter, a simplified radar front-end is assembled for use with the fabricated antenna to further demonstrate its capabilities.

As a proof-of-concept demonstration, the radar front-end was assembled from laboratory equipment and commercial components. This simplified radar system was used to determine the location of a set of corner reflectors in a hallway. Targets were able to be resolved in both angle and range. Furthermore, a flexibility in range and angular resolutions when using a frequency scanning approach was shown. The measurement results demonstrated the successful application of the antenna in a frequency-scanned radar system.

### 7.1 Demonstration Overview

A block diagram depicting the overall configuration of the demonstration for a single target is shown in Figure 7.1. For the reasons discussed in Chapter 4, as well as its simple implementation, the quasi-monostatic antenna configuration is used. The bandwidth and centre frequency of the transmitted signals were set according to the values determined in Section 6.2.2 for beam steering in discrete two-degree increments and are summarized in Figure 7.2. In this implementation, an oscilloscope performed the function of the radar processor, sampling the receiver's beat frequency signal and transforming it to the frequency domain using a Fast Fourier Transform (FFT). During measurements, the presence of a target at a given angle was determined based on the observation of a discernible peak in the displayed signal. The frequency for which this peak occurs indicated the range to the target. The beat frequency signals

for each transmitted centre frequency were stored and later combined to produce a two-dimensional radar image. This permitted post-processing threshold detection to simultaneously resolve a target's location in both range and direction.

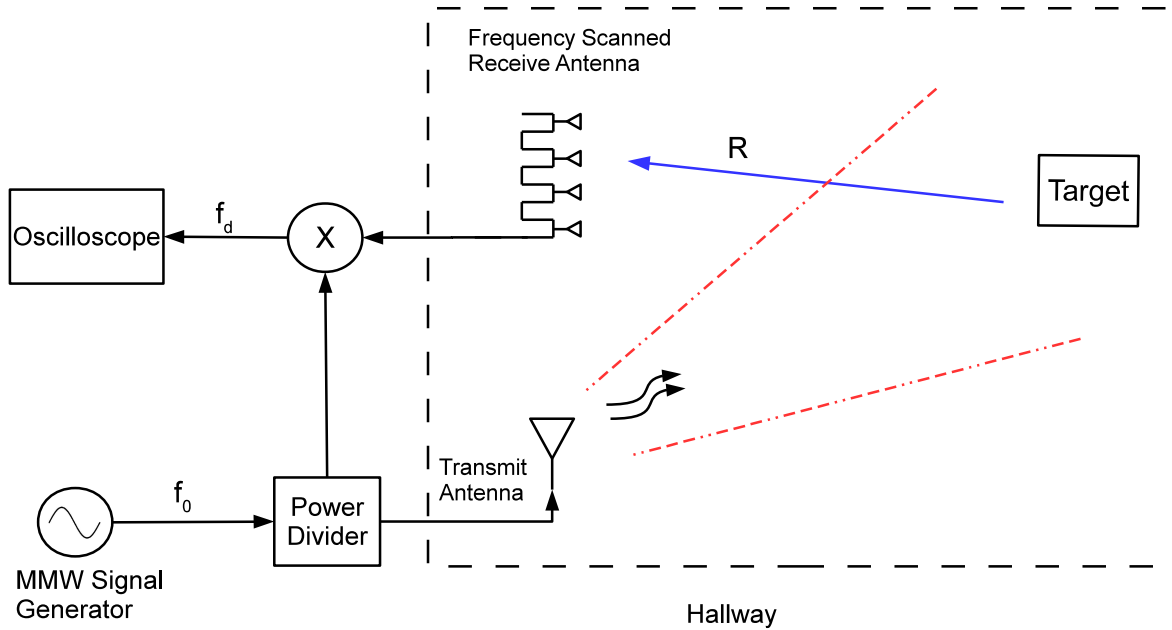


Figure 7.1: Block diagram of simplified radar front-end and demonstration configuration.

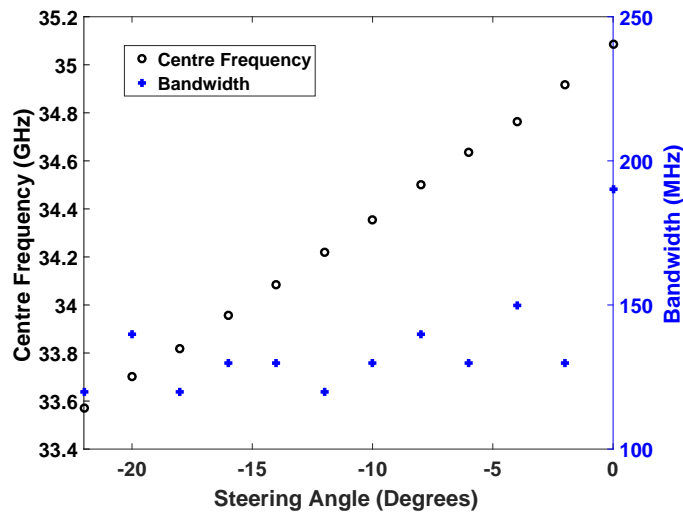


Figure 7.2: Radar transmitted frequency scanning scheme.

To verify the antenna's application, a set of corner reflectors were placed a distance away from the implemented radar system in a number of configurations. Initially, a single target measurement was

completed. This provided insight on the behaviour of the implemented radar in the demonstration environment. A second demonstration consisted of determining the location of a set of three targets displaced in both range and angular position. Finally, two targets were aligned in angle relative to the radar and closely spaced in range. The received signals for two different bandwidths were compared to illustrate the radar's versatility in resolution.

There were a number of factors that led to the decision to perform the demonstrations in a hallway rather than in a far-field chamber or outdoor environment. It was desired to perform the demonstration for relatively short ranges; this allowed the radar to operate with a low transmitted power, and without amplification in the receiver, simplifying its implementation. It was expected, and later verified, that the five metre range of the available far-field chamber would result in the received echo being masked by the transmitter leakage phenomenon described in Chapter 4. Compared to an outdoor location, the interior hallway provided a relatively controlled environment, with convenient access for repeatable results. The hallway was selected as it allowed for relatively short target distances, while still providing sufficient ranges to ensure echoes were not overpowered by transmitter leakage.

One significant disadvantage is apparent for radar measurements in an interior environment. The transmitted radar signals will also be reflected toward the receiver from walls, floors, and other large features. The stationary nature of these resulting clutter signals allows the clutter map technique described in Chapter 4 to be applied in post-processing and is further detailed in the results section of this chapter.

### 7.1.1 Radar Components

The use of laboratory equipment and commercial components simplified the implementation of a radar system. The MMW signal generator and oscilloscope blocks of Figure 7.1 represent the transmitter and processor components of the radar front-end. While the commercially available power divider and mixer perform the receiving functions. The fabricated antenna and a commercial standard gain horn complete the radar.

The general purpose laboratory equipment used for the transmitter and radar processor components of the front-end are pictured in Figure 7.3. These components allowed the radar demonstration to be quickly configured for beam steering and provided easy access to measured data. The MMW signal generator used was Keysight's E8257D. This source allowed the centre frequency and bandwidth of a linearly modulated signal to be specified according to Figure 7.2 but restricted the signal's duration to 10 ms. The Keysight 54846A oscilloscope measured the received beat frequency based on a trigger signal

produced by the generator. The signal was windowed to the length of the generated signal and an FFT applied to obtain its frequency domain representation.

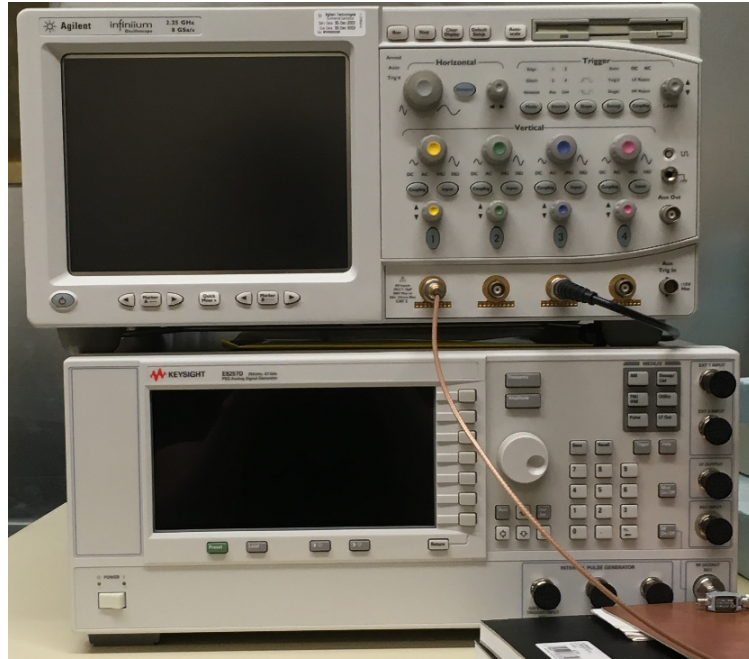


Figure 7.3: Laboratory equipment used in demonstration. The Keysight E8257D (bottom) acts as the radar transmitter while the Keysight 54846A (top) performs the functions of a radar processor and display.

The receiver was assembled from the commercially available components seen in Figure 7.4. The Taylor Microwave PD2S-12400 equally divides the MMW signal generator's power between the transmitting antenna and the local oscillator (LO) port of the Marki MM1-2567LS mixer. In effectively multiplying the received echo signal from the frequency-scanned antenna with the reference signal applied to its LO port, the mixer produces the beat frequency signal measured by the oscilloscope. For simplicity, an active low-pass filter was omitted, as the cut-off frequency of the mixer's IF port, as well as the sampling rate of the oscilloscope, act as a passive low-pass filter to reject higher frequencies that result from the mixing process.

Figure 7.5 depicts the quasi-monostatic configuration of the radar's antennas. The waveguide-fed slot array receiving antenna is seen on the right, while the transmitting antenna is on the left. The Quinstar QWH-KPRS pyramidal horn was used as the transmitting antenna. This antenna's gain is specified as 24 dB with a six degree beamwidth. Omitted from this image, is approximately 2.6 metres of coaxial cable used to connect the antennas to the radar front-end. The velocity factor of this cable is specified as 0.83, effectively increasing the apparent range of a target by approximately 3.1 metres.



Figure 7.4: Demonstration Receiver Components. Taylor Microwave PD2S-12400 power divider (left) and Marki MM1-2567LS mixer (right).

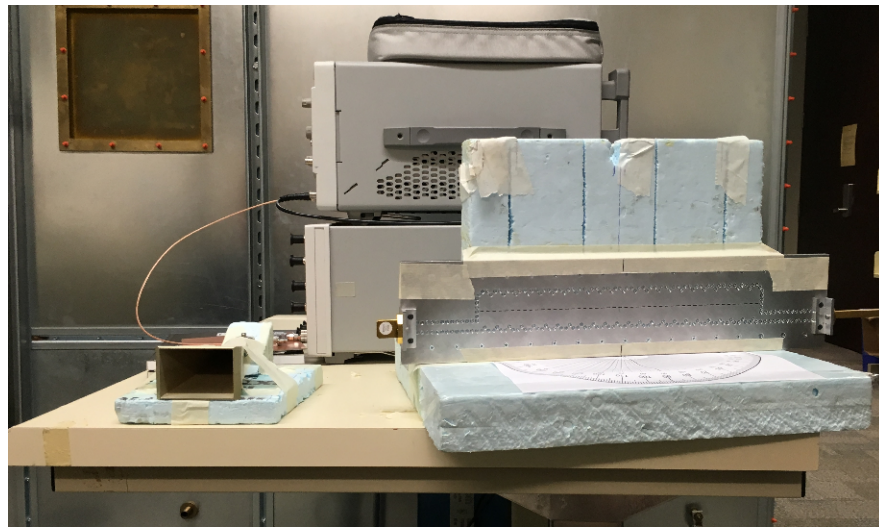


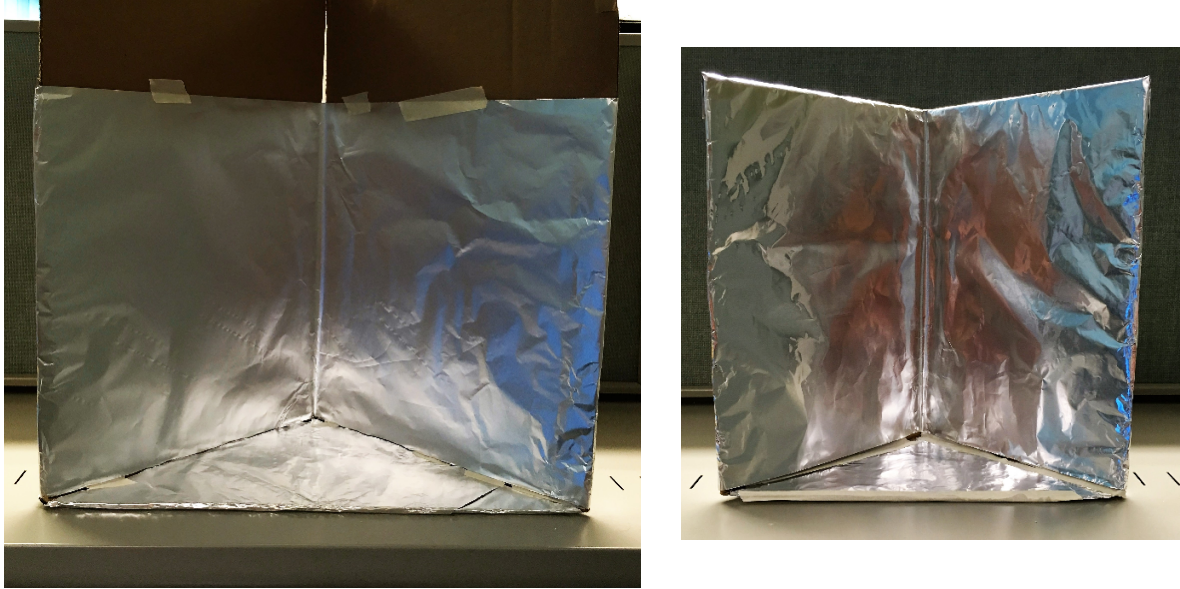
Figure 7.5: Demonstration Radar Antenna Configuration.

### 7.1.2 Targets

A set of rectangular corner reflectors were constructed to use as targets to locate. Corner reflectors were selected as they provide a relatively large radar cross section compared to their physical size that varies little with the viewing angle. Additionally, their simple geometry allows for easy construction. For near normal incident angles, the radar cross section is proportional to the projected area in the direction of the radar and is approximated by [10]

$$\sigma = \frac{4\pi A^2}{\lambda_0^2} \quad (7.1)$$

where  $A$  is the projected area. Figure 7.6 depicts the two sizes of corner reflectors constructed using aluminum foil. The larger reflector's projected area is  $0.12 \text{ m}^2$  while the smaller reflector's is  $0.078 \text{ m}^2$ , leading to calculated RCS values of +33.7 and +30 dB respectively. Based on the extreme sensitivities in geometry experienced in the design of the antenna and the relatively crude construction of the targets, the realized values are expected to be drastically reduced, and these values were largely ignored. Thus, the primary benefit of the corner reflectors was their broad angular response.



(a) Larger corner reflector with height of 30cm and projected width of 40cm.

(b) Smaller corner reflector with height and projected width both equal to 28 cm.

Figure 7.6: Corner reflectors constructed for demonstration.

### 7.1.3 Signal-to-Noise Ratio Estimate

As an initial prediction of successful radar measurements, an estimate of the received signal-to-noise ratio (SNR) was calculated prior to the radar's implementation. The estimate was determined from the radar equation as presented in (4.5) and (4.7) as well as the receiver noise and noise figure values described in Chapter 4. The calculation assumed nominal measurement parameters, listed in Table 7.1, that were selected based on the scanning characteristic of the antenna and the area available for measurements.

Parameter	Symbol	Value
Frequency	$f_0$	34.3 GHz
Receiver Bandwidth	$B$	100 kHz
Range	$R$	15 m
Temperature	$T_0$	290 K

Table 7.1: Nominal Measurement Parameters.

In addition to the nominal experimental parameters, the radar equation includes factors to account for individual component performance. Component power and gain values were obtained from measurements or manufacturer specifications and are found in Table 7.2. From the previous discussion regarding the relatively crude construction of the corner reflections, the calculated RCS values were disregarded and a nominal value of 0 dB was assumed and thought to represent the worst case.

To provide a more practical estimate of the received power and therefore SNR, component losses

Component	Symbol	Power/Gain
MMW Signal Generator	$P_t$	15 dBm
Transmitting Antenna	$G_t$	24 dB
Receiving Antenna	$G_r$	16 dB
Target RCS	$\sigma$	0 dBm <sup>2</sup>

Table 7.2: Power and Gain Values for Implemented Radar.

were included in the calculations. The total losses are summarized in Table 7.3. Individual component values were obtained from manufacturer specified insertion losses, while an additional loss factor was introduced to account for the large number of interconnections and other omitted effects.

Component	Symbol	Loss (dB)
Power Divider	$L_{divider}$	4
Cable Losses	$L_{cables}$	6
Mixer	$L_{mixer}$	9
System Loss	$L_{sys}$	3
Total Loss	$L$	22

Table 7.3: Total Losses.

The estimated received power as measured by the oscilloscope was calculated from Equation (4.5) expressed in dBm

$$P_r = P_t + G_t + G_r + \sigma + 10 \log_{10} \left( \frac{\lambda_0^2}{(4\pi)^3 R^4} \right) - L \quad (7.2)$$

with the calculated value found as  $P_r = -88.18$  dBm.

To calculate the SNR for this received power, the receiver's thermal noise power and system noise figure were required. The noise power was determined from the parameters listed in Table 7.1 and Equation (4.8) expressed in dBm:

$$N_0 = 10 \log_{10} (kT_0 B / 10) + 30 \quad [\text{dBm}] \quad (7.3)$$

The resulting value was  $N_0 = -124$  dBm. Figure 7.1 shows only the mixer in the path of signal received from the antenna before it is measured at the oscilloscope. Thus, the mixer's specified noise figure of 9 dB describes the total system noise figure,  $F_{sys}$ . The system's SNR was then obtained from

$$\frac{S}{N} = P_r - N_0 - F_{sys} \quad (7.4)$$

The resulting SNR estimate was 26.8 dB. This value was thought to be sufficient for successful measurements with the laboratory equipment used in the demonstration. Based on the discussion in Chapter 4, if the received signal proved too weak to resolve, a low noise amplifier may be inserted in the

receiver chain to significantly increase this ratio.

### 7.1.4 System Limitations

In designing the radar demonstration, simplicity and reduced costs were prioritized. Where possible, previously obtained components and laboratory equipment were used. Their use, as well as the measurement within the interior hallway environment resulted in a number of system limitations that were not accounted for in the practical considerations discussed in Chapter 4. In particular, a relatively narrow transmitting antenna beamwidth, limited signal processing, and alignment errors reduced the performance of the system.

As envisioned in Chapter 1, a frequency-scanned radar system may use a transmitting antenna with a broad beamwidth to direct radiation over the entire observation region and determine the direction of a target based on the angle of the received echo. The transmitting antenna available for this demonstration was specified for a six degree beamwidth. For the designed two degree scanning beamwidth, this corresponds to only three angular cells being effectively illuminated. As a result, the efficiency of the radar system decreases significantly over its entire scanning range. Fortunately, this impact was reduced as large angular coverage was not required for the narrow hallway environment.

The block diagram of Figure 7.1 shows an oscilloscope performing the function of the radar processor. In this demonstration, the oscilloscope simply measured the received signal, performed an FFT, and displayed the results to an operator. This implementation was limited to processing received echoes for fixed steering angles. To produce two-dimensional radar images, the received signals were required to be stored for each angle and later combined. An implicit assumption in this method was the observed region remained unchanged between measurements. For this reason, the demonstration was limited to stationary targets.

Performing radar measurements in the enclosed environment of the hallway, resulted in a significant amount of clutter echoes observed in the received signal. To reduce their detrimental effect on target detection, the clutter map technique from Chapter 4 was used. The method used here is described in detail later in this chapter. In short, it required a comparison between the measured signal with the presence of a target and the measured signal from the empty environment. This process introduced a source of error as it required both antennas' orientation to remain constant throughout all measurements. Efforts were made to minimize their movement; however, small errors in orientation are expected and will manifest as artifacts in the processed signals.

## 7.2 Results

The implemented radar system was used to detect and locate the set of corner reflectors for the configurations described in the previous section. The received signals, as measured by the oscilloscope for the single target case, were used to evaluate the radar's basic performance. From these results, a method to generate a two-dimensional radar image with reduced clutter was developed. This method was applied to the remaining multiple target configurations that were measured at a later date. The final results demonstrate the capabilities of the fabricated antenna when included in a radar system.

### 7.2.1 Single Target

For the first demonstration, a single, large corner reflector was placed 15 metres from the radar in an approximately 50 metre long hallway. Its placement is pictured in Figure 7.7. The transmitting horn antenna was directed toward the target, while the frequency-scanned receiving antenna was rotated such that the target was located  $-12^\circ$  from broadside.

To observe the received signal from a target direction of  $\theta_0 = -12^\circ$ , the MMW source was configured to transmit a linearly modulated signal centred at  $f_o = 34.22$  GHz with a bandwidth  $\Delta B_n = 120$  MHz and duration  $T_b = 10$  ms. The resulting beat signal is plotted in Figure 7.8. Clearly, the effect of the transmitter leakage is seen in the large magnitude for frequencies below 1 kHz. A peak with a magnitude -78 dBm is measured at  $f_d = 1.465$  kHz. Substituting the appropriate values into the FMCW equation for range, (4.3), indicates this peak is produced by a target at 18.31 m. The error in range is easily accounted for by the 3.1 metre equivalent additional length of the cable used in connecting the antennas. Reflections from the hallway's far wall are seen to produce an additional peak at  $f_d = 3.906$  kHz, or equivalently, at a range of 48.85 m. Smaller peaks are also observed in the signal and were considered clutter, attributed to reflections from the background environment.

To better verify the ability of the radar to resolve a target's range, the frequency axis of Figure 7.8 was first scaled to its equivalent distance. In doing so, a range correction factor of 3.1 metres was subtracted to account for the length of cables. To further improve the corrected signal, a minimum range of 10 metres was adopted such that effect of the leakage was not observed. The resulting corrected signal for the  $\theta_0 = -12^\circ$  case is shown in Figure 7.9. To confirm the source of the smaller peaks distributed throughout the received signal, the measurement was repeated without the target in place. This clutter signal is included in the figure for reference and indicates the observed peak at 15 metres is indeed due to the presence of the target.

To demonstrate the radar's, and therefore antenna's, ability to resolve a target's location in angle,



Figure 7.7: Single Target Demonstration.

a two-dimensional radar image was produced. The measured signals for each transmitting signal configuration described in Figure 7.2 were corrected using the above approach. The corrected signals for each steering angle were then resampled to a common differential range of 1.25 metres and combined to form a polar radar image. To approximate the behaviour of a practical radar system and improve target visibility, a threshold was applied to the measured signal. An initial threshold value of -90 dBm was set based on the signal of Figure 7.9 and the noise power level calculated in Section 7.1.3. The generated image is depicted in Figure 7.10(a).

The radar image of Figure 7.10(a) indicates the limited benefit of simple thresholding in a cluttered environment. The clutter signal magnitudes are comparable to the echo produced by the corner reflector, making it difficult to distinguish the target. To improve target visibility in the image, the clutter map in Figure 7.10(b) was generated by measuring the entire region without the target in place. An additional

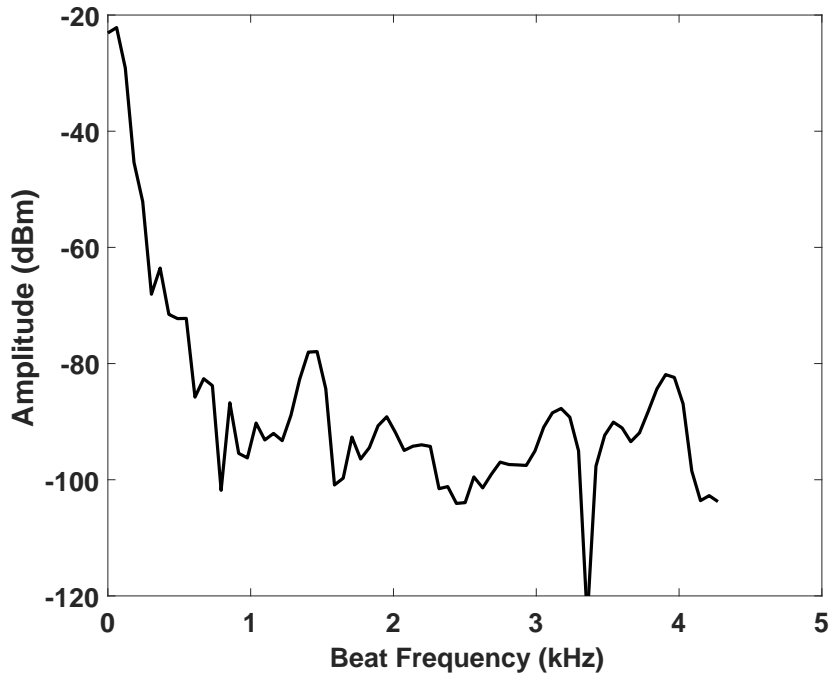


Figure 7.8: Measured Received Radar Signal for Single Target. Transmitting signal was configured with  $f_o = 34.22$  GHz and  $\Delta B_n = 120$  MHz corresponding to  $\theta_o = -12^\circ$ .

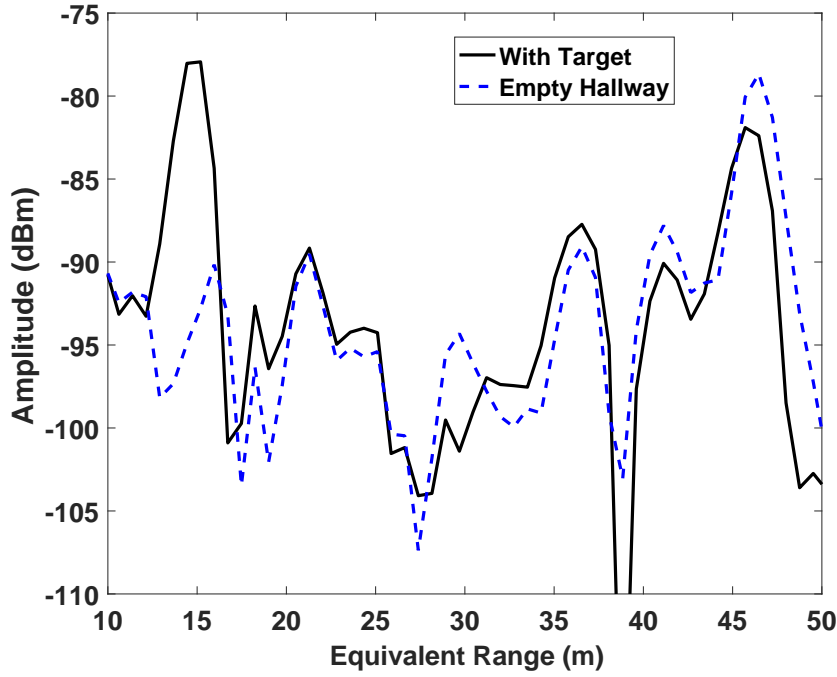
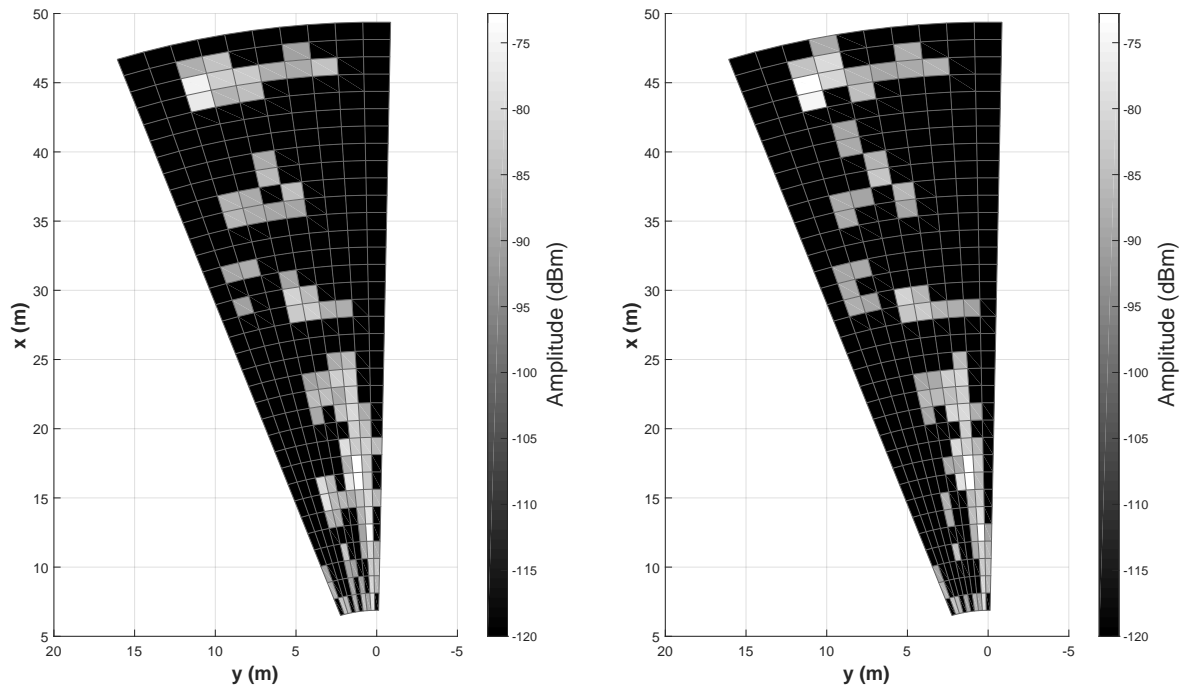


Figure 7.9: Single Target Corrected Range Measurement.



(a) Measured radar image with target located at  $R = 15$  m and  $\theta = -12^\circ$ .

(b) Measured radar image of empty hallway.

Figure 7.10: Measured Radar Images for Single Target.

threshold criterion was introduced, where only received signals 6 dB greater than the clutter map value for the same location are retained.

In addition to the clutter map implementation, the visible region included in the radar image was reduced to improve target visibility. Both images show a strong return for  $\theta = -4^\circ$ , due to reflections from the nearest sidewall of the hallway. After the clutter reduction, artifacts remained in the processed image for angles closer to broadside. These artifacts were attributed to orientation errors as described in Section 7.1.4 as well as secondary reflections. These measurements corresponded to non-physical locations and were rejected accordingly. Furthermore, a metal railing resulted in both images depicting a broad target at an approximate range of 30 metres. This value was adopted as a maximum range. The final processed radar image is plotted in Figure 7.11 and the target's location is clearly resolved.

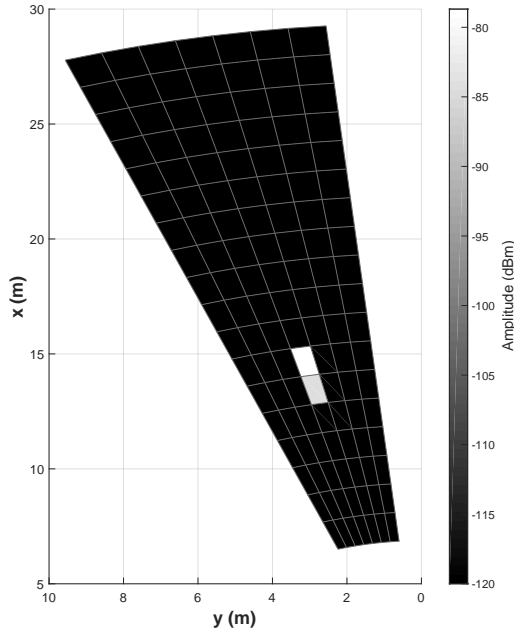


Figure 7.11: Processed Single Target Radar Image.

### 7.2.2 Multiple Targets

To further demonstrate the capabilities of a radar employing the frequency-scanned antenna, measurements were performed with multiple targets in the radar's field of view. The process developed for the single target configuration was applied to obtain a two-dimensional radar image. The resulting image successfully validated the radar's ability to resolve the locations of multiple targets simultaneously.

In this demonstration, three corner reflectors were placed in the radar's field of view as pictured in Figure 7.12. Two smaller corner reflectors were placed 12.5 metres from the radar and spaced 2 metres apart. A third, larger corner reflector was placed 18 metres from the radar, between the two smaller targets. The transmitting horn was directed toward the centre target, while the frequency scanned antenna was rotated such that the centre target was approximately  $-8^\circ$  from broadside.

A radar range measurement was completed for each discrete two-degree steering angle of the antenna. Following the process developed for the single-target demonstration, the range measurements were combined to form a two-dimensional image. Minimum and maximum ranges of 10 and 30 metres respectively were again used. The produced image, after applying the -90 dBm threshold, is featured in Figure 7.13(a). As these measurements were taken at a separate date than the single target demonstration, a new clutter map was generated and is shown in 7.13(b).

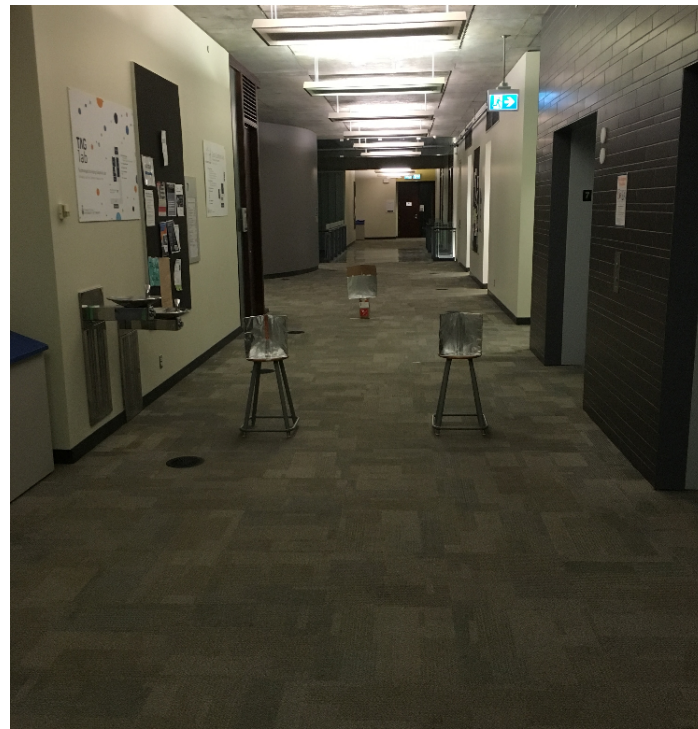
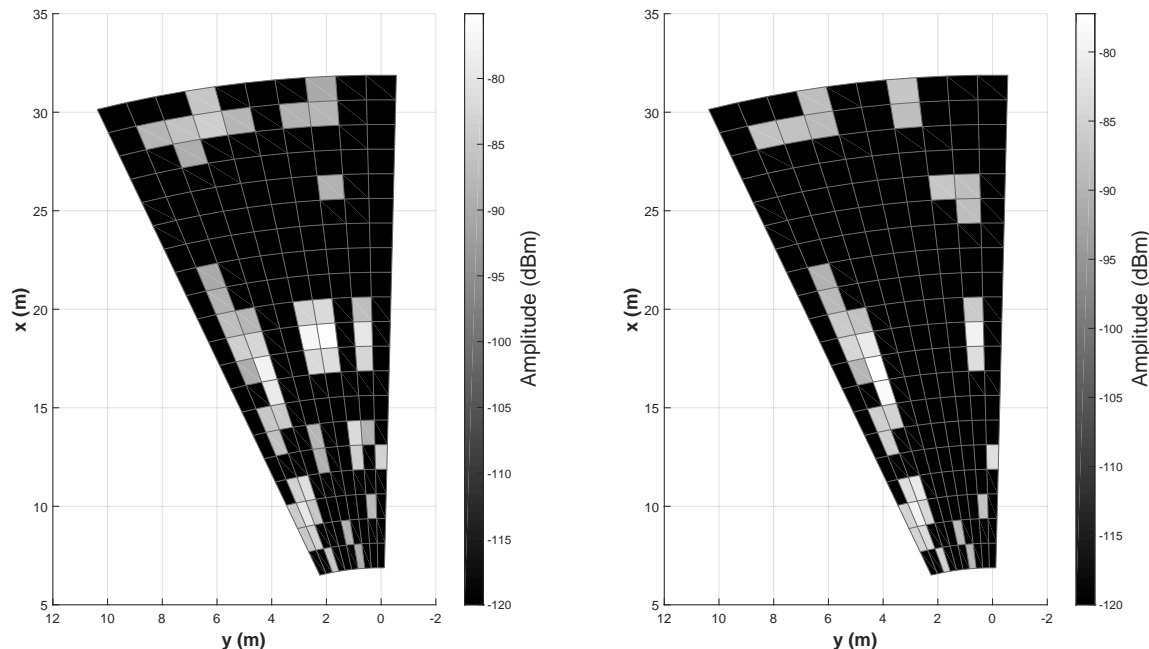


Figure 7.12: Multiple Target Demonstration.



(a) Measured radar image with multiple targets in view.

(b) Measured radar image of empty hallway.

Figure 7.13: Measured Radar Image for Multiple Targets.

Figure 7.14 depicts the processed radar image following the reduction of clutter. Similar to the single target measurement, the field of view was restricted. Here, the viewing range,  $-14^\circ \leq \theta \leq -2^\circ$ , was used corresponding to the area within the sidewalls of the hallway. All three targets are seen to be resolved; however, the effect of the limited beamwidth of the transmitting antenna is apparent. The return from the left, smaller reflector is reduced when compared to the right equal sized target. Additionally, the larger corner reflector appears across two angular cells. This image indicates the transmitting horn was focused at  $\theta = -6^\circ$ , with the left target at  $\theta = -10^\circ$  falling just outside the half power beamwidth of the transmitting antenna.

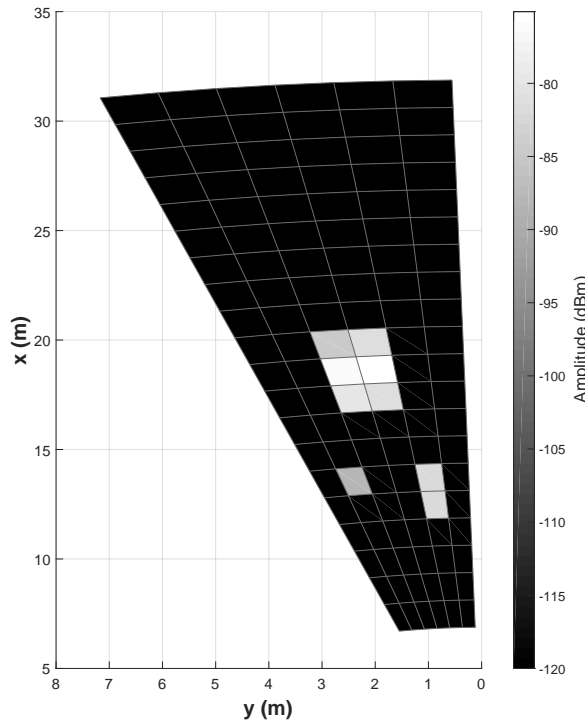


Figure 7.14: Processed Multiple Target Radar Image.

### 7.2.3 Range Resolution

The results of the previous two demonstrations illustrate a limitation in the practical range resolution of the implemented radar. The maximum dimension of either sized corner reflector is less than half the calculated range resolution at any steering angle, yet the results depict the targets are distributed over multiple range cells. The primary source of this error is the simple threshold detection used. For signal peaks sufficiently larger than the threshold level, the signal's value exceeds the threshold for a number of frequency points as it decays from the maximum. Consequently, the realized range resolution

depends on the threshold level and received signal strength, as well as the signal bandwidth. Additional practical effects, including the linearity of the transmitted signal's frequency-time characteristic, and an FFT window used by the oscilloscope tend to broaden the peaks of the received signals, further reducing the achieved range resolution.

The limitations of the simplified radar front-end prevented a practical evaluation of the upper limit of range resolution supported by the frequency scanned antenna. The values calculated from the measured scanning characteristic are left as an ideal value for a more sophisticated implementation, that was considered outside the scope of this work. Rather than attempt to measure these limits in detail, a demonstration of the resolution versatility of the implemented radar is presented here.

From previous discussions, it is clear that there is an implicit compromise between the radar's range and angular resolutions. The continuous scanning characteristic of the frequency-scanned antenna permits dynamic adjustments to this compromise. To demonstrate this versatility, measurements were performed for two targets closely spaced in range and approximately located in the  $\theta = -8^\circ$  direction. The transmitted signal's centre frequency was set according to Figure 7.2 for  $-12^\circ \leq \theta \leq -2^\circ$  and two radar images were produced. One using a fixed bandwidth of  $\Delta B = 100$  MHz, and a second with  $\Delta B = 150$  MHz. The expected result is that the increased bandwidth will improve range resolution at the expense of the associated increase in beam scanning and reduced angular resolution.

To establish an appropriate target spacing, the first corner reflector was placed approximately 15 metres from the radar, with the second placed some distance behind it. The received radar signal was observed on the oscilloscope for a transmitted bandwidth of 100 MHz. The target spacing was increased until two distinct peaks were visible on the oscilloscope's display. The resulting spacing was approximately 3.5 metres and the corresponding corrected range measurement for  $\theta = -8^\circ$  is seen in Figure 7.15(a). The signal's maxima were measured to occur at 14.28m and 18.86m, indicating a measured target spacing of 4.58 metres. The total 1.08m error in this measurement falls within the measurement range resolution of 1.5 metres for this bandwidth, and therefore satisfies an acceptable margin of error.

Figure 7.15(b) depicts the processed radar image for angles near the target and a fixed bandwidth of 100 MHz at each angle. The use of a fixed bandwidth removed the requirement to resample the range measurements in order to generate a radar image and permitted a valid comparison between the range resolutions of both bandwidths. The image shows that the simple thresholding detection is unable to resolve the separate targets in range. This should be expected from the range measurement seen in 7.15(a). While the peaks are clearly distinguishable, the local minimum between them does not fall below the threshold value of -90 dBm.

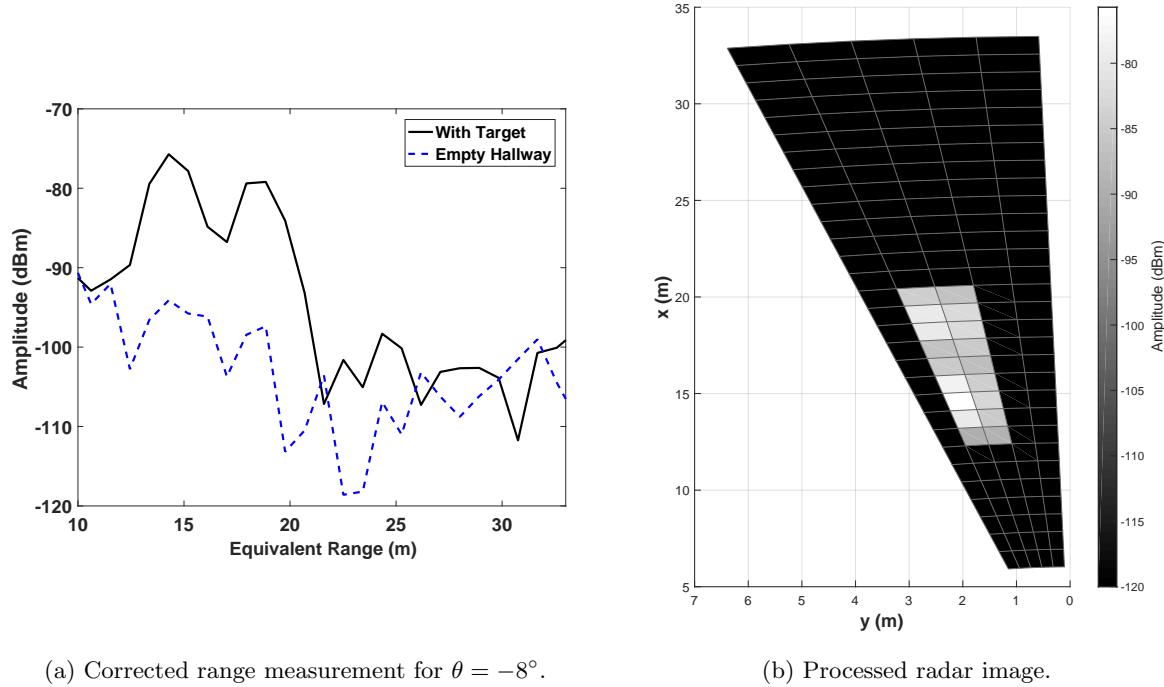


Figure 7.15: Range Resolution Demonstration with 100 MHz Bandwidth. Targets spacing of approximately 3.5m

The preceding measurements were repeated for the same target spacing but with the fixed bandwidth set to 150 MHz. The results are seen in Figure 7.16. The peaks in the corrected range measurement were observed at 14.58 and 18.24 metres, indicating a spacing of 3.66 metres. Compared to the 100 MHz case, this is much closer to the expected value of 3.5 metres. Moreover, the target's peaks are observed to be steeper, resulting in a local minimum between them that falls below the -90 dBm threshold. This is reflected in the two-dimensional radar image, as both targets are resolved in range. A slight trade-off in angular accuracy is seen, as the rear target is observed to extend into an additional angular cell.

The results of this demonstration suggest that a radar incorporating the frequency-scanned antenna in its design, may adaptively adjust its range and angular resolutions according to a target's size. The bandwidths of 100 and 150 MHz used in this demonstration were selected as they would ensure the antenna's beam was directed at the targets as it scanned slightly about a fixed angle. This technique may be applied using larger bandwidths provided the antenna's beam is directed at the target for all frequencies within the bandwidth. A detailed evaluation of this capability would require a more sophisticated radar controller and processing. This was considered outside the scope of this work and left for future development.

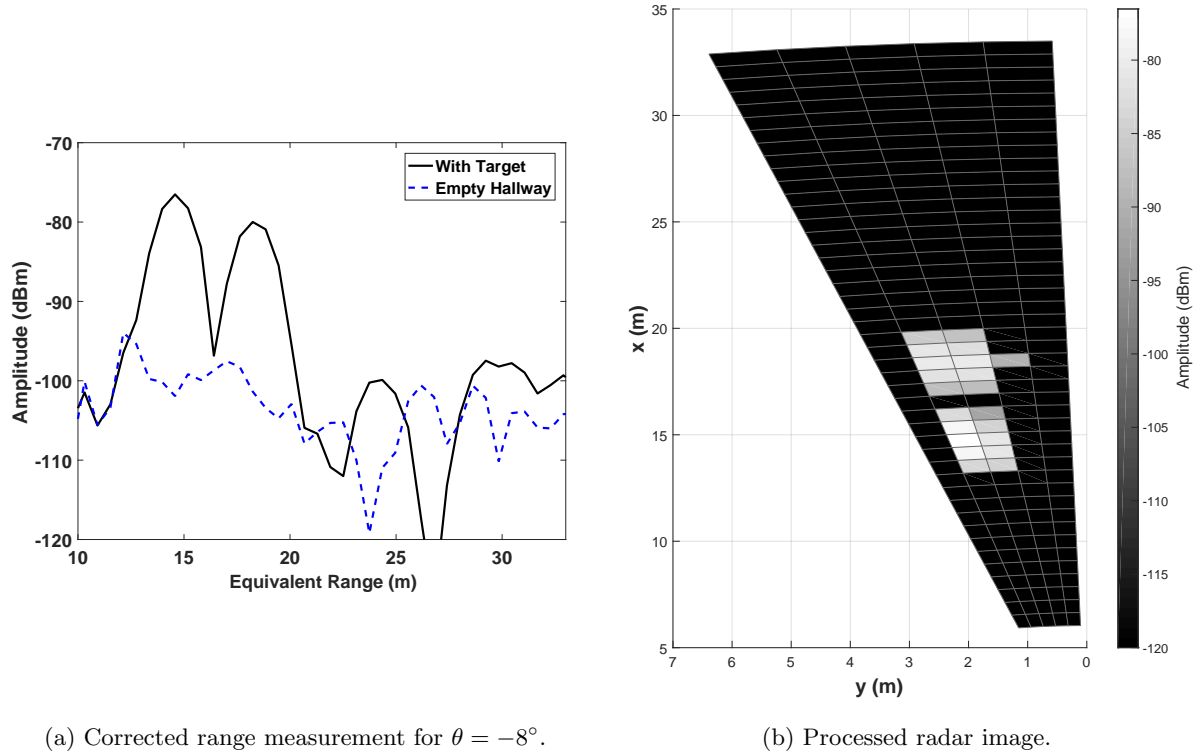


Figure 7.16: Range Resolution Demonstration with 150 MHz Bandwidth. Targets spacing of approximately 3.5m

### 7.3 Summary

In this chapter, a simplified frequency-scanned radar system was implemented for use with the fabricated waveguide-fed slot array. The radar served to demonstrate the basic application of the frequency-scanned antenna. From the measurement results of both the single and multiple target configurations, targets were successfully resolved in both angle and range. The radar's implementation prioritized simplicity and cost efficiency, requiring compromises in its performance. As the focus of this work was specifically the performance of the designed antenna, the measurement results of Chapter 6 should be referred to for achievable performance in more rigorously designed radar.

# Chapter 8

## Conclusion

The objective of this work was to design and implement a frequency-scanned waveguide-fed slot array suitable for MMW radar applications. To accomplish this, a set of desired features and specifications were identified that would ensure the antenna's feasible use and guide its design process. The designed antenna was fabricated, and its performance analyzed. The results indicated its compatibility with a frequency-scanned radar system despite limitations inherent to the manufacturing technologies used. A simplified radar demonstration verified its operation in resolving multiple targets' locations in both range and direction.

The antenna was designed for operation in a 1.8 GHz frequency band centered at 34.3 GHz. The design was based on a serpentine waveguide structure to produce the required frequency-dependent phase shift for beam scanning. Slots along the axis of the array act as discrete antennas, and adjusting their lengths permitted a specified radiation pattern to be synthesized. A set of circular pits in the bottom of the waveguide suppressed the reflections generated from the slots when excited in phase, allowing the antenna's beam to scan through broadside, albeit with a noticeable reduction in gain.

The MMW waveguide design produced a simple, robust, and relatively compact antenna structure. The fabricated antenna consists primarily of two aluminum components and requires no moving parts or additional electronics. This greatly limits potential points of failure when compared to mechanical or phased-array beam steering techniques. In particular, it should be noted that an equivalent length phased array would require an electronically-controlled feed module for each radiating element. Designing the antenna for MMW frequencies allowed its physical size to be relatively small, while maintaining the sufficiently large electrical length for a narrow beamwidth. The final structure measured 18 x 4 x 0.3125 inches; however, the length and width may be reduced to approximately 12 and 1.5 inches respectively,

based on the total interior dimensions of the serpentine geometry.

The antenna's performance was evaluated through simulation and far-field measurements. The measurement results indicated its scanning characteristic and beamwidth satisfied the identified requirements and agreed with simulations. The antenna produced a beamwidth less than  $1.8^\circ$  that scanned from  $-24.9^\circ$  to  $+1.4^\circ$  as the operating frequency increased over its 1.8 GHz bandwidth. The primary benefit of the MMW design is observed here, as the available bandwidth was sufficient to scan the beam and maintain a range resolution better than 1.25 metres. The beamwidth and scanning performance suggested the antenna was suitable for the basic radar function of determining a target's angle and range.

In observing the antenna's measured radiation patterns, it was determined that the realized gain and side lobe level performances were reduced compared to the designed and expected simulated values. The measured gain of 16 dB for steering angles away from broadside, represented a 4 dB decrease relative to the simulation results. Further performance degradation occurred near broadside, where the gain was measured to be 13 dB and the beamwidth increased to  $3.5^\circ$ . Side lobe levels were measured to be 16.5 to 18 dB below the beam maximum. These values represent an improvement when compared to a uniform array's 13.5 dB SLL, however, they did not meet the antenna's specifications. While these performance degradations did not restrict the basic functionality of a radar, they place limitations on the maximum range and the antenna's utility in applications where target RCS values are expected to vary significantly.

Further investigation through simulation indicated the primary source of the performance degradation was insufficient electrical contact between the waveguide's sidewalls and the top plate. Inserting a ten micron air gap between the antenna's components resulted in simulated gain values agreeing with the measured reduction away from broadside. The reduction in gain was attributed to conductor loss due to surface currents existing within the air gap. The simulation results also predicted the large, 4 dB return loss measured at the broadside frequency, as well as the corresponding reduction in gain and increased beamwidth. A secondary source of error was observed in the misalignment of the top plate and waveguide channel. An increase in SLLs, proportional to the displacement of the radiating slots was observed. When combined with the excitation amplitude error due to the air gap, a uniform offset of 200 microns in the direction of the width of the antenna produced SLLs similar to those measured.

Implementing a simplified radar front-end permitted further verification of the antenna's application. The front-end was assembled from laboratory equipment and commercial components, allowing the system to be reconfigured as required to demonstrate the capabilities of the antenna. Targets were able to be resolved in both range and angle in single- and multiple-target configurations using simple threshold detection.

The measured antenna performance and radar demonstration support the antenna's implementation in a MMW radar. The antenna's beamwidth, scanning characteristic, and resulting range resolution satisfy the proposed specifications for the accurate determination of a target's location. Due to the fabrication techniques used, the antenna's efficiency and directivity suffered. In applications where these parameters are critical and costs permit, more advanced techniques may be employed in assembling the antenna components. A radar demonstration illustrated the successful application of the antenna; however, the upper limits of its performance were not supported. A more sophisticated radar implementation, discussed in Section 8.1, may further exploit the characteristics of the designed antenna for more advanced features and increased performance.

## 8.1 Future Directions

In the completion of this work, two distinct directions were identified in which future work may be pursued toward the development of the envisioned radar system of Chapter 1. First, and most evident, the antenna's design and implementation may be refined to meet or exceed the performance specifications selected for this work. This may be achieved through employing more precise manufacturing technologies, or by extending the antenna's radiating aperture in a second dimension to focus its beam in an additional plane. The second direction would consist of the development of a radar front-end designed specifically to exploit the performance capabilities of the implemented antenna. Combining the outcomes of these future developments would result in a complete high-performance radar system suitable for many applications.

Increasing the electrical conductivity between the antenna's components will improve the antenna's efficiency, and therefore gain, to better match the simulated values. Furthermore, the elimination of the air gap is critical to maintaining antenna performance as the beam scans through broadside. From the discussion in Chapter 3, the antenna's components may be joined using a brazing or laser welding process without requiring modifications to its design. These processes use high temperatures to join the components and result in improved electrical contact, though complications can arise due to distortion of thin features, such as the waveguide's cover and interior side walls, when exposed to these temperatures. Thus, some trial and error may be required. As an alternative, one simple modification is a compromise proposed in [45], where the waveguide channel and slots are cut into the same conducting block. The circular pits may be milled in a separate thick base plate, and the increased rigidity when compared to the thin sheet is expected to increase the conductivity of the resulting electrical contact when bolted together. This design is compatible with the milling techniques used in this work, and represents a compromise, in both cost and performance, between the simple fabrications used in this work, and laser

welding or brazing.

The use of more accurate CNC milling equipment would permit a design incorporating a more precise mechanical feature resolution, allowing a more accurate implementation of a synthesized array factor. This in turn would eliminate the additional length added to compensate for errors in the approximated amplitude distribution and permit lower SLL distributions to be designed. As an example, a 10 micron resolution used in [27], permitted a design with a SLL of -35 dB for a similar length antenna in the same operating frequency range. This represents a mechanical resolution one tenth the value available for this work.

This work established that increasing the length of the array resulted in a reduced beamwidth as observed in the azimuthal scanning plane. The corresponding increase in directivity is limited, as the one-dimensional array produces an approximately uniform beamwidth in the antenna's elevation plane. It follows that extending the array's radiating aperture along its width, will reduce the elevation beamwidth, producing what is referred to as a pencil beam. In radar applications, the benefits of this reduced beamwidth are twofold. First, the more directive radiation pattern increases the antenna's gain and therefore the radar's maximum range. Second, the effect of ground reflections are reduced, whether the antenna is transmitting or receiving. This reduces the amount of noise and clutter measured by the radar and increases its sensitivity.

There are numerous techniques to increase the width of the radiating aperture, and therefore directivity, of the antenna. Previously used methods include implementing a two-dimensional array of slots, employing a cylindrical reflector, or coupling the radiating slots to patch arrays orientated along the width. A two-dimensional slot array may be constructed in combining a set of linear waveguide-fed slot arrays adjacent in their widths. The serpentine structure of the frequency scanned antenna does not allow this configuration; however, each slot may be coupled to a linear resonant waveguide-fed slot array as part of a two-dimensional array. The resulting radiation pattern features a pencil beam that scans along the axis of the serpentine waveguide. In this case, the total structure becomes large, costly to produce, and is no longer planar, potentially limiting its application. A cylindrical reflector was used in combination with a frequency scanned slot array in [27] to reduce the elevation plane beamwidth. The cylindrical reflector is fed by the frequency scanned antenna, and is shaped such that the reflected radiated waves are collimated, or aligned, in elevation and produce a more narrow, directive beam. Again, this method increases the size and cost of the total antenna. Finally, linear patch arrays, placed on top of each radiating slot and oriented along the antenna's width were successfully used in [22]. The patch arrays may be considered discrete elements of a linear frequency-scanned array with an element pattern that contains a narrow beamwidth in the elevation plane. From the principle of pattern multiplication,

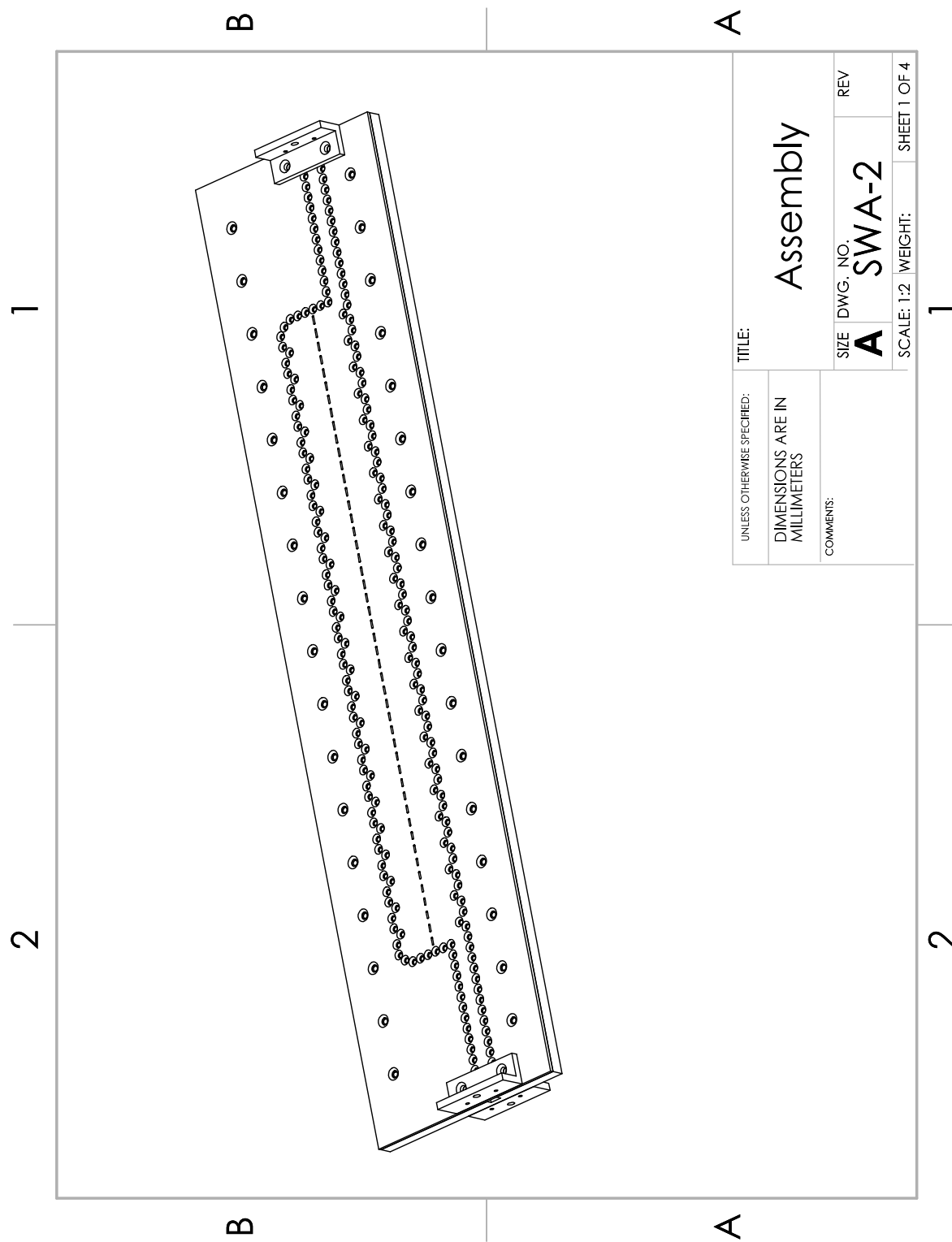
and the narrow azimuthal beamwidth of the linear array, a pencil beam is produced. This method produces a relatively planar structure, however the coupling between each patch and slot increases the complexity of the design process.

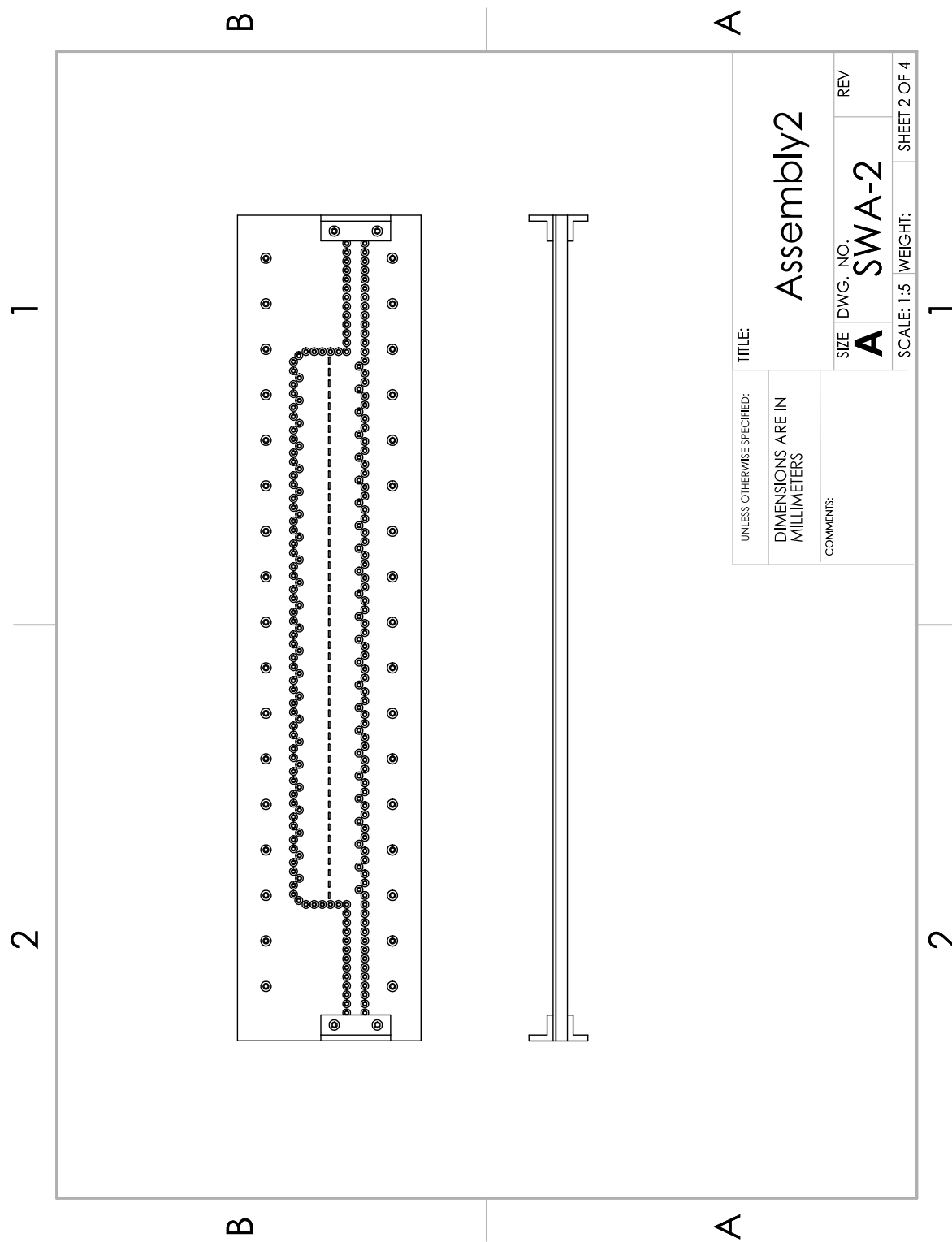
In addition to the previously used techniques described, research is currently being conducted at the University of Toronto to develop metasurface transmitarrays to reduce the elevation plane beamwidth. These thin surfaces are designed to act as planar lenses, focusing a fan beam. When combined with the antenna designed in this work, the resulting structure is virtually planar and produces a pencil beam that scans in the azimuthal plane.

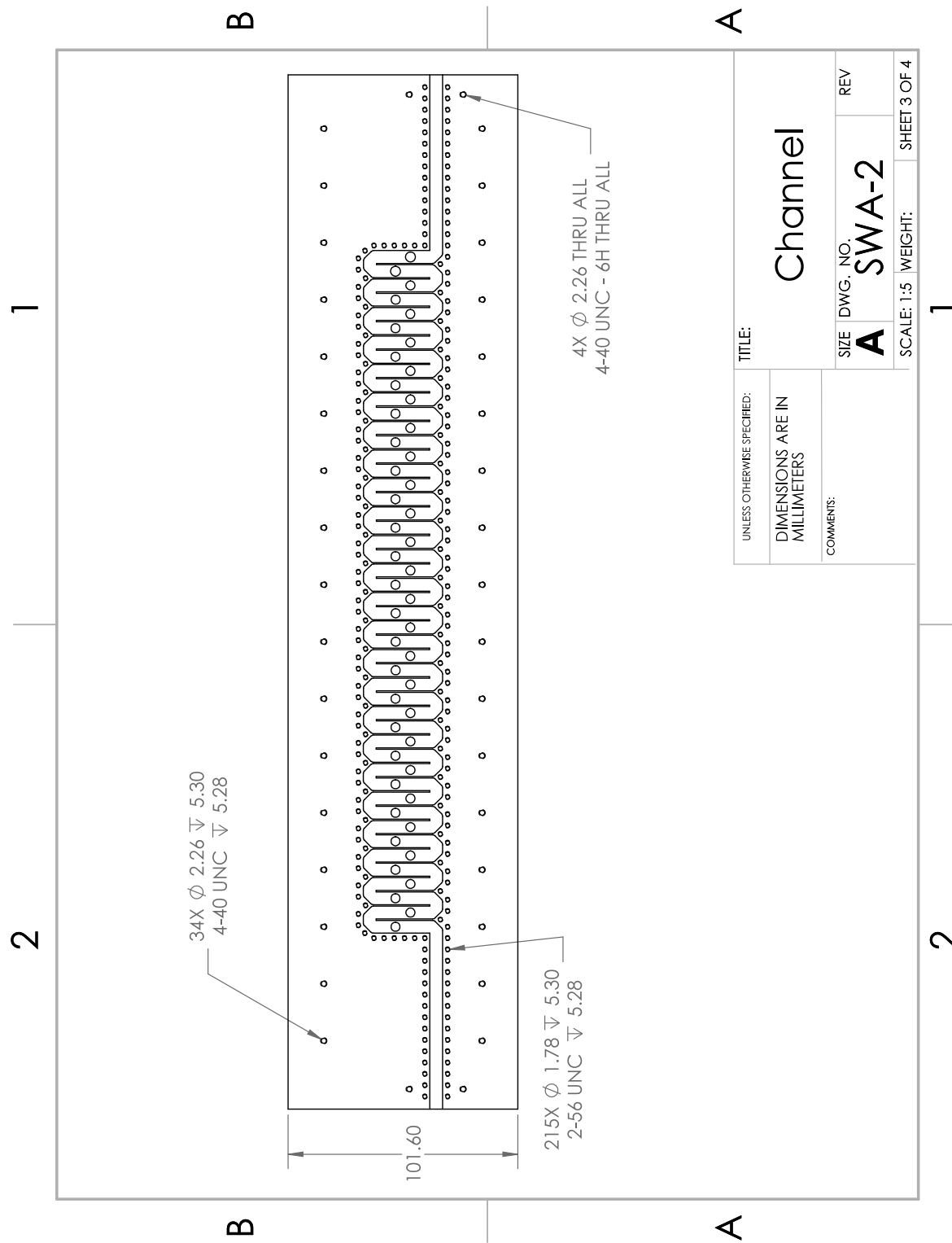
Finally, to implement a comprehensive radar system satisfying the desired performance outlined in Chapter 1, an integrated front-end may be developed. The basic front-end used in the radar demonstration of this work, was assembled from discrete, general-purpose components. This approach simplified its implementation while significantly sacrificing performance. An integrated, complete radar front-end may be designed and implemented on a printed circuit board, reducing its size and eliminating losses within cables and interconnections. The signal generator and oscilloscope may be replaced with a voltage controlled oscillator and microcontroller with digital signal processing (DSP) capabilities and data storage. Relative to the operator-controlled angular scanning used in the demonstration of this work, a microcontroller can instantaneously adjust a VCO's frequency to rapidly steer the radar's observed direction. Combined with the processing speed and data storage of the microcontroller, near real-time monitoring and radar processing is feasible, and should permit the detection and tracking of moving targets. Improved target detection algorithms, when compared to the simple thresholding used here, may also be employed to better resolve a target's location. Furthermore, the microcontroller may be programmed to dynamically adjust the compromise in range and angular resolutions to adapt to varying target sizes. The inclusion of an LNA in the receiver chain, would increase the radar's range to appreciable distances, allowing for practical surveillance applications. The result will be a versatile, robust, radar system suitable for many applications.

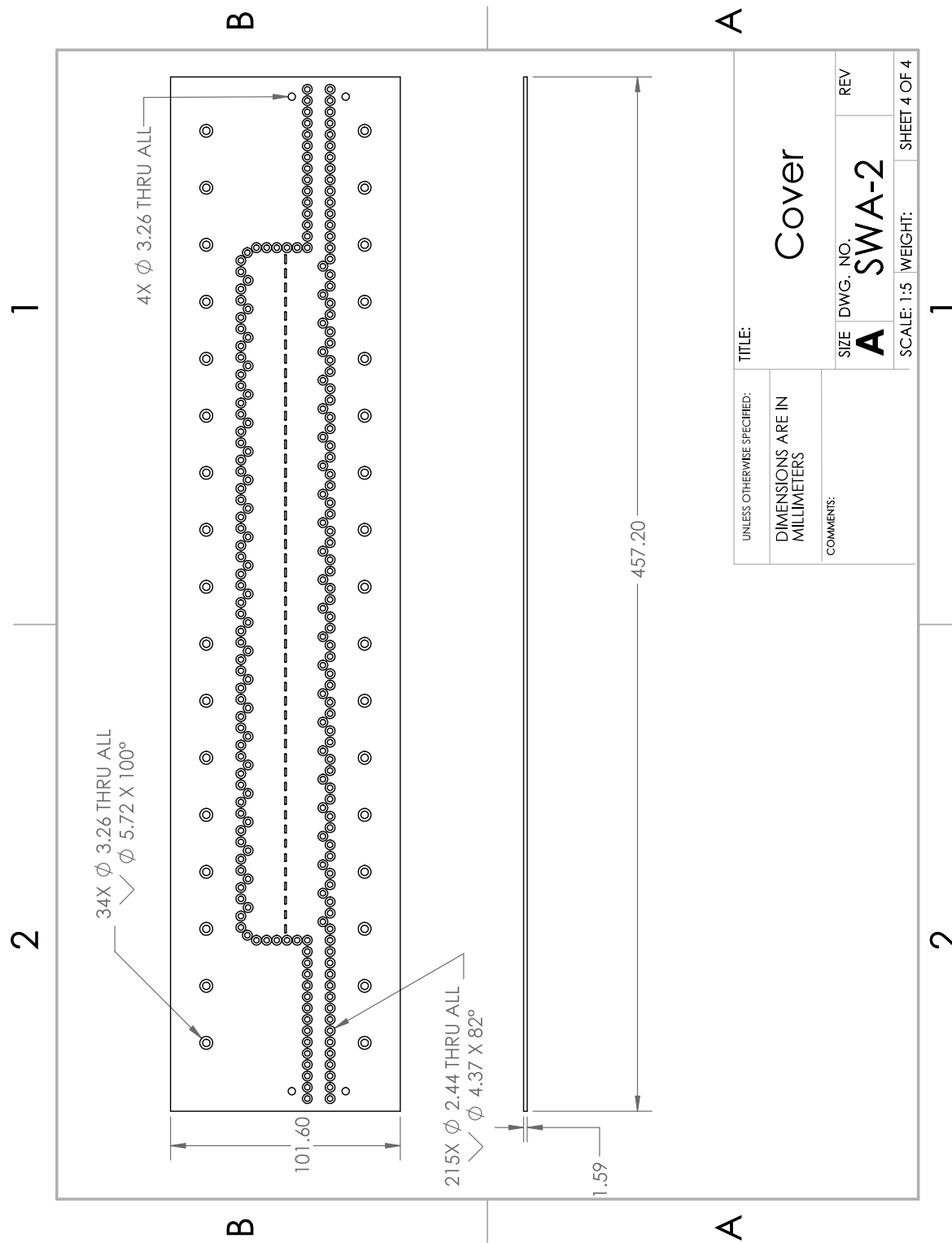
## **Appendix A**

### **Detailed Antenna Drawings**









# Bibliography

- [1] J. C. Wiltse, "History of millimeter and submillimeter waves," *IEEE Transactions on Microwave Theory and Techniques*, vol. 32, no. 9, pp. 1118–1127, Sep 1984.
- [2] Automotive radar millimeter-wave technology. NXP Semiconductors. [Online]. Available: <http://www.nxp.com/pages/automotive-radar-millimeter-wave-technology:AUTRMWT>
- [3] The stalker ii hand-held police radar. [Online]. Available: [http://www.stalkerradar.com/law\\_stalkerII.php](http://www.stalkerradar.com/law_stalkerII.php)
- [4] Introducing facebook's new terrestrial connectivity systems terragraph and project aries. Facebook Inc. [Online]. Available: <https://code.facebook.com/posts/1072680049445290/introducing-facebook-s-new->
- [5] *Attenuation by atmospheric gases*, International Telecommunication Union Std. Recommendation ITU-R P.676, 2013. [Online]. Available: <https://www.itu.int/rec/R-REC-P.676/en>
- [6] H. J. Liebe, T. Manabe, and G. A. Hufford, "Millimeter-wave attenuation and delay rates due to fog/cloud conditions," *IEEE Transactions on Antennas and Propagation*, vol. 37, no. 12, pp. 1617–1612, Dec 1989.
- [7] F.-J. Tospann, M. Pirkl, and W. Gruener, "Multifunction 35-ghz fmcw radar with frequency scanning antenna for synthetic vision applications," vol. 2463, 1995, pp. 28–37. [Online]. Available: <http://dx.doi.org/10.1117/12.212752>
- [8] Ranger r1 short-range ground surveillance radar. FLIR. [Online]. Available: <http://www.flir.com/surveillance/display/?id=64733>
- [9] A. Mukherjee, S. Stolpner, X. Liu, U. Vrenozaj, C. Fei, and A. Sinha, "Large animal detection and continuous traffic monitoring on highways," in *SENSORS, 2013 IEEE*, Nov 2013, pp. 1–3.

- [10] M. I. Skolnik, *Introduction to Radar Systems*, 3rd ed. McGraw-Hill College, 2001.
- [11] Averse. Phased\_array\_(2).png. CC BY-SA 2.0 DE. German language Wikipedia. [Online]. Available: [https://upload.wikimedia.org/wikipedia/commons/0/09/Phased\\_array\\_%282%29.png](https://upload.wikimedia.org/wikipedia/commons/0/09/Phased_array_%282%29.png)
- [12] I. P. Theron and J. H. Cloete, “On slotted waveguide antenna design at ka-band,” in *Communications and Signal Processing, 1998. COMSIG '98. Proceedings of the 1998 South African Symposium on*, Sep 1998, pp. 425–426.
- [13] M. Ando, “Planar waveguide arrays for millimeter wave systems,” *IEICE transactions on communications*, vol. 93, no. 10, pp. 2504–2513, 2010.
- [14] Y. Wang, M. Ke, M. J. Lancaster, and J. Chen, “Micromachined 300-ghz su-8-based slotted waveguide antenna,” *IEEE Antennas and Wireless Propagation Letters*, vol. 10, pp. 573–576, 2011.
- [15] A. Stevenson, “Theory of slots in rectangular wave-guides,” *Journal of Applied Physics*, vol. 19, no. 1, pp. 24–38, 1948.
- [16] R. Elliott and L. Kurtz, “The design of small slot arrays,” *IEEE Transactions on Antennas and Propagation*, vol. 26, no. 2, pp. 214–219, Mar 1978.
- [17] R. Elliott, “On the design of traveling-wave-fed longitudinal shunt slot arrays,” in *Antennas and Propagation Society International Symposium, 1979*, vol. 17, Jun 1979, pp. 22–25.
- [18] K. W. Brown, “Design of waveguide slotted arrays using commercially available finite element analysis software,” in *Antennas and Propagation Society International Symposium, 1996. AP-S. Digest*, vol. 2, July 1996, pp. 1000–1003 vol.2.
- [19] R. K. Enjiu and M. Perotoni, “Slotted waveguide antenna design using 3d em simulation,” *Microwave Journal, International ed.*, vol. 56, p. 72, Jul 2013.
- [20] G. Pfister, “The series 320 radar: Three-dimensional air surveillance for the 1980s,” *IEEE Transactions on Aerospace and Electronic Systems*, vol. AES-16, no. 5, pp. 626–638, Sept 1980.
- [21] C. M. Lain and E. J. Gersten, “AN/TPS-59 overview,” in *International Radar Conference, 1975*, pp. 527–532.
- [22] M. Vahidpour, M. Moallem, J. East, and K. Sarabandi, “Micromachined low-mass rf front-end for beam steering radar,” vol. 8373, 2012, pp. 83731N–83731N–13. [Online]. Available: <http://dx.doi.org/10.1117/12.920797>

- [23] K. Sakakibara and J. Hirokawa, "A linearly-polarized slotted waveguide array using reflection-cancelling slot pairs," *IEICE transactions on communications*, vol. 77, no. 4, pp. 511–518, 1994.
- [24] J. Sato, J. Hirokawa, and M. Ando, "Reflection-canceling of slotted waveguide antenna by using a circular pit," in *Antennas and Propagation Society International Symposium, 1998. IEEE*, vol. 3. IEEE, 1998, pp. 1706–1709.
- [25] S. Park, J. Hirokawa, and M. Ando, "Analysis of a waveguide slot with a reflection-canceling post," IEIC Technical Report 102.232, Tech. Rep., 2002.
- [26] ——, "Analysis and design of a waveguide slot and a reflection-canceling inductive wall," in *Wireless Communication Technology, 2003. IEEE Topical Conference on.* IEEE, 2003, pp. 362–363.
- [27] K. Solbach, "Below-resonant-length slot radiators for traveling-wave-array antennas," *IEEE Antennas and Propagation Magazine*, vol. 38, no. 1, pp. 7–14, Feb 1996.
- [28] H. Gruenberg, "Second-order beams of slotted wave guide arrays," *Canadian Journal of Physics*, vol. 31, no. 1, pp. 55–69, 1953. [Online]. Available: <http://dx.doi.org/10.1139/p53-006>
- [29] K. Sakakibara, J. Hirokawa, M. Ando, and N. Goto, "Design of a slotted waveguide array using reflection-canceling slot pairs," in *PROCEEDINGS OF THE INTERNATIONAL SYMPOSIUM ON ANTENNAS AND PROPAGATION JAPAN*, vol. 1. INSTITUTE OF ELECTRONICS, INFORMATION & COMMUNICATION ENGINEERS, 1992, pp. 121–121.
- [30] C. A. Balanis, *Antenna Theory: Analysis and Design, 3rd Edition*, 3rd ed. Wiley-Interscience, 4 2005.
- [31] C. Dolph, "A current distribution for broadside arrays which optimizes the relationship between beam width and side-lobe level," *Proceedings of the IRE*, vol. 34, no. 6, pp. 335–348, jun 1946. [Online]. Available: <http://dx.doi.org/10.1109/JRPROC.1946.225956>
- [32] T. T. Taylor, "Design of line-source antennas for narrow beamwidth and low side lobes," *Transactions of the IRE Professional Group on Antennas and Propagation*, vol. 3, no. 1, pp. 16–28, Jan 1955.
- [33] A. Villeneuve, "Taylor patterns for discrete arrays," *IEEE Transactions on Antennas and Propagation*, vol. 32, no. 10, pp. 1089–1093, Oct 1984.
- [34] R. S. Elliott, *Antenna Theory & Design*. Wiley-IEEE Press, 2003.

- [35] H. G. Booker *et al.*, "Slot aerials and their relation to complementary wire aerials (babinets principle)," *J. IEE*, vol. 93, no. pt III, pp. 620–626, 1946.
- [36] J. Volakis, *Antenna Engineering Handbook, Fourth Edition*. McGraw-Hill Education, 2007.
- [37] M. Ando, M. Zhang, J. Lee, and J. Hirokawa, "Design and fabrication of millimeter wave slotted waveguide arrays," in *Proceedings of the Fourth European Conference on Antennas and Propagation*, April 2010, pp. 1–6.
- [38] J. W. Digby, C. E. McIntosh, G. M. Parkhurst, B. M. Towlson, S. Hadjiloucas, J. W. Bowen, J. M. Chamberlain, R. D. Pollard, R. E. Miles, D. P. Steenson, L. S. Karatzas, N. J. Cronin, and S. R. Davies, "Fabrication and characterization of micromachined rectangular waveguide components for use at millimeter-wave and terahertz frequencies," *IEEE Transactions on Microwave Theory and Techniques*, vol. 48, no. 8, pp. 1293–1302, Aug 2000.
- [39] K. Sakakibara and J. Hirokawa, "Single-layer slotted waveguide arrays for millimeter wave applications," *IEICE transactions on communications*, vol. 79, no. 12, pp. 1765–1772, 1996.
- [40] K.-L. Chan and S. R. Judah, "A beam scanning frequency modulated continuous wave radar," *IEEE Transactions on Instrumentation and Measurement*, vol. 47, no. 5, pp. 1223–1227, 1998.
- [41] G. M. Brooker, "Understanding millimetre wave fmcw radars," in *1st International Conference on Sensing Technology*, 2005, pp. 152–157.
- [42] Wr-28 standard gain horn antenna operating from 26.5 ghz to 40 ghz with a nominal 20 db gain 2.92mm female input connector. [Online]. Available: <https://www.pasternack.com/standard-gain-horn-waveguide-size-wr28-20-db-gain-292mm-female-pe98502f-20-p.aspx>
- [43] M. Pirkl and F.-J. Tospann, "Hivision millimeter-wave radar for enhanced vision systems in civil and military transport aircraft," in *AeroSense'97*. International Society for Optics and Photonics, 1997, pp. 8–18.
- [44] M. I. Skolnik, *Radar Handbook*. McGraw-Hill Professional, 1990.
- [45] J.-H. Hwang and Y. Oh, "A single-layer waveguide slot array antenna using diaphragms for easy manufacture and high performance," in *Antennas and Propagation Society International Symposium, 2003. IEEE*, vol. 3. IEEE, 2003, pp. 1038–1041.